Middle-atmospheric wind measurements by the ground-based passive radiometer WIRA-C

Inaugural dissertation
of the Faculty of Science,
University of Bern

presented by

Jonas Hagen

from Hüttwilen, TG

Supervisor of the doctoral thesis: Prof. Dr. Niklaus Kämpfer
Institute of Applied Physics

Middle-atmospheric wind measurements by the ground-based passive radiometer WIRA-C

Inaugural dissertation
of the Faculty of Science,
University of Bern

presented by

Jonas Hagen

from Hüttwilen, TG

Supervisor of the doctoral thesis: Prof. Dr. Niklaus Kämpfer
Institute of Applied Physics

Accepted by the Faculty of Science.

The Dean:

Bern, 6. Juli 2020 Prof. Dr. Zoltan Balogh

Summary

This thesis is dedicated to the measurement of wind in the middle-atmosphere, more precisely, zonal and meridional wind in the stratosphere and lower mesosphere from 30 to 70 km altitude. Dynamics in the middle atmosphere have an impact on life on Earth, by coupling to ozone chemistry and tropospheric weather systems. Nevertheless, measurements of middle-atmospheric wind speeds are surprisingly rare and continuous observations are difficult to achieve. Doppler microwave wind radiometry is capable to deliver such measurements by measuring the tiny Doppler shift introduced to thermal emission lines of atmospheric molecules due to the movement of air as wind.

This thesis is specifically concerned with the Wind Radiometer for Campaigns, WIRA-C, a replication and improvement of the prototype Wind Radiometer WIRA. It is a highly sensitive spectrometer that is capable to measure the weak thermal emission of middle-atmospheric molecules. It is ground-based and passive, meaning that it is easy to deploy and to operate remotely, especially also over extended periods of time.

Chapter 1 gives a short introduction to the middle-atmosphere and its dynamics. Of special interest are waves on various scales which are relevant to this thesis, from global scale waves to short scale disturbances. The goal is to give an overview over the state of middle-atmospheric research and its most important topics. Further this chapter includes a summary of the available measurement Methods which are capable to measure wind in the atmosphere. Again, the focus lies on the region of interest from 30 to 70 km altitude.

Chapter 2 contains an introduction and some historical context on microwave wind radiometry, which is a rather novel technique. This is followed by a quick introduction to the WIRA-C wind radiometer and some details about its calibration and retrieval algorithm.

The aim and impact of this thesis are summarized in chapter 3. This puts this thesis in the context of the European Commission's Horizon 2020 ARISE2 project, which also provided funding for this research project.

Chapter 4 gives the overview plots of the different campaigns that WIRA-C and WIRA have been in the last years. It will highlight the effects visible on large timescales and discuss them in a global context.

The following chapters 5, 6 and 7 present the scientific outcome of this thesis, represented by publications in peer-reviewed journals.

The publication in chapter 5 presents the in-depth description of the WIRA-C wind radiometer together with coincident lidar observations from the Maido campaign on La Réunion island.

Chapter 6 consists of a publication about the measurements of the atmospheric diurnal tide by passive microwave radiometry. These results are novel and represent an advancement in Doppler microwave radiometry. Using a composite analysis we reach very short timescales in the order of hours which provides a unique insight to the long-time behaviour of atmospheric tides and their variability.

The third publication in chapter 6 represents an improvement of passive microwave radiometry on the technical side, by taking advantage of modern software-defined radio techniques and evaluating its performance in the context of atmospheric research.

Finally, Chapter 8 provides some conclusive remarks and an outlook into possible future projects.

Contents

1 The middle atmosphere

The atmosphere enables life on Earth's surface by providing protection against the hostile space environment and sustaining the water vapour cycle. Air pressure drops exponentially with altitude while the temperature profile is more complicated and features multiple maxima and minima, which are generally used to define different layers of the atmosphere as shown in figure 1.1(a).

The troposphere is the lowermost layer and extends from the ground up to approximately 6 km at the poles and 17 km altitude in equatorial regions. It contains approximately 80% of the total air-mass of the atmosphere. The troposphere is dominated by weather phenomena like convection and clouds, storms and complex high and low pressure systems.

Above the troposphere begins the stratosphere. The local maximum in the temperature profile defines its upper extent to approximately 50 to 65 km. Above the stratosphere comes the mesosphere and temperature decreases again with altitude up to the mesopause at approximately 80 to 110 km where the thermosphere starts.

The altitude region between 20 km and 80 km, containing the stratosphere and mesosphere, is generally referred to as the middle atmosphere. Dynamics in the middle atmosphere have an impact on weather, extreme weather and climate change on Earth's surface. Yet, the dynamics of this altitude region in current weather models are poorly constrained due to the lack of available observations.

The following sections give a short introduction to the dynamics in the middle atmosphere and an overview over measurement techniques which are sensitive to middle atmospheric wind.

1.1 Structure and dynamics

In the stratosphere, the temperature rises with altitude. This increase in temperature is mainly caused by the absorption of solar UV-radiation by ozone chemistry, which is active in the whole middle atmosphere. Ozone chemistry is most effective in the lower stratosphere forming a region with high ozone concentration at 15 to 40 km altitude, the so called ozone layer.

This positive temperature gradient (positive lapse rate) results in a high vertical stability of the stratosphere. On the other hand, deposition of momentum and energy by atmospheric waves excite the stratosphere. While this forcing is not enough to drive the stratosphere away from its thermal equilibrium, it accounts for the large observed variability in the temperature and wind field. This forcing gains importance over radiative effects with

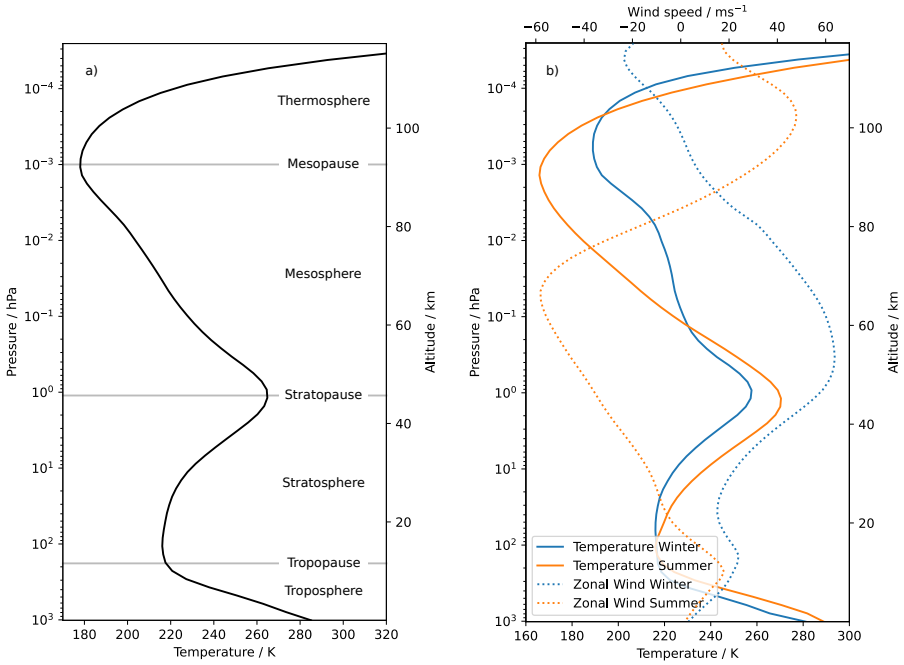

Figure 1.1 Structure of the atmosphere (a) and seasonal zonal wind speeds and temperature (b) according to the COSPAR International Reference Atmosphere (CIRA-86) on northern mid-latitudes on pressure and altitude scales.

altitude, ultimately inverting the sign of the temperature gradient at the stratopause resulting in a negative lapse rate for the mesosphere.

In the stratosphere and lower mesosphere, the temperature gradient, while influenced by dynamical effects, is still in thermal equilibrium and dominated by radiative heating and cooling. Thus the mean background wind speeds on a global scale can be understood in a context with thermal equilibrium. In this picture, radiative heating in the equatorial regions leads to a latitudinal temperature gradient. This gradient results in quasi-geostrophic winds which are westward directed in the summer hemisphere and eastward directed in the winter hemisphere. These background winds reverse twice a year around equinox, following the seasonal cycle of solar irradiation. A climatology of these seasonal patterns is shown in figure 1.1(b) for mid-latitudes clearly showing the difference in zonal wind direction between summer and winter.

A concrete but typical global circulation pattern at the stratopause level for northern hemisphere summer is shown in figure 1.2. Westwards jet on the summer hemisphere (north) and strong eastwards jets on winter hemisphere (south) are clearly visible.

1.2 Coupling to lower and upper atmosphere

The variability in the stratosphere and mesosphere is to a large extent driven by waves that propagate upwards from the troposphere. But in the last decades it became evident that the coupling between the middle atmosphere and the troposphere is a two-way process. Middle atmospheric dynamics have an influence on tropospheric dynamics and thus on weather patterns (Baldwin et al., 2003; Charlton et al., 2004). Especially for enhancing seasonal forecasts outside of the tropical regions, the middle atmosphere plays

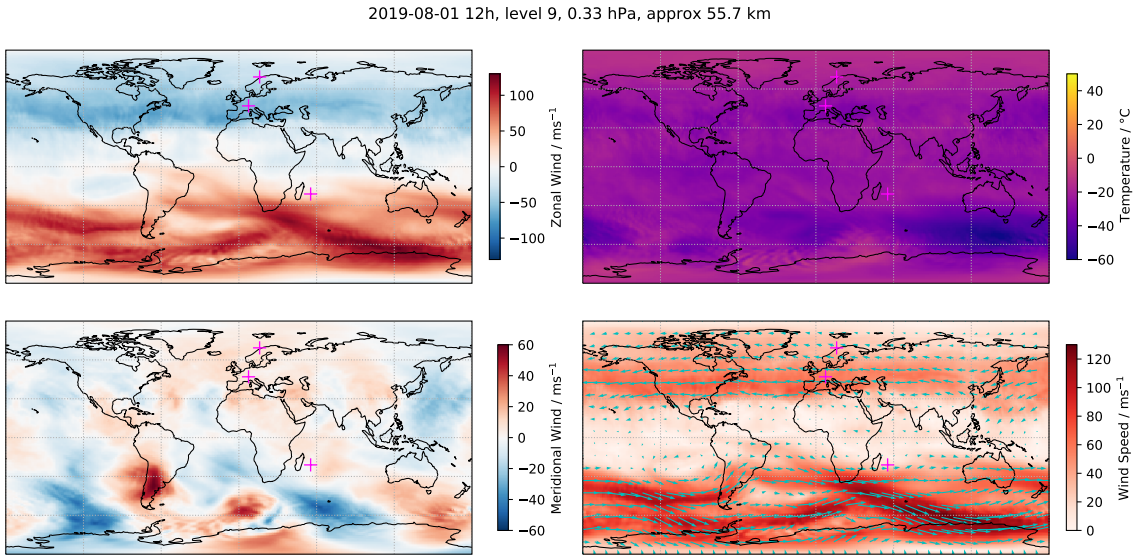

Figure 1.2 Zonal wind speed (top left), meridional wind speed (bottom left), temperature field (top right), wind magnitude and direction (bottom right): Data for August 1st, 2019 from the ECMWF operational model. Campaign locations Andøya, Bern and La Réunion are marked.

a central role (Sigmond et al., 2013). For this reason, more and more analysis models expand their model-top to higher altitudes and often include model layers up to the lower mesosphere.

Accompanied to this model developments there is a growing need for observations at these altitudes for data assimilation into the models. Without enough measurements to assimilate in these altitudes, the models are left with often difficult to adjust parametrizations and numerical tricks like sponge-layers and artificial damping to reproduce the required behaviour (Alexander et al., 2010; Kim, Eckermann, and Chun, 2003).

The middle atmosphere also is essential for the forcing from below for the thermosphere and ionosphere. Planetary, tidal and gravity waves propagate from the middle atmosphere upwards and excite variability in the thermosphere (Forbes and Salah, 1991). The coupling between the mesosphere and the thermosphere is supposed to be based largely on nonlinear wave interactions like gravity and tidal wave coupling (Palo et al., 2007).

The exact influence of these vertical coupling mechanisms between the lower-, middle- and upper atmosphere, especially in the context of extreme events, is a vital area of research. More measurements to better constrain middle-atmospheric dynamics are needed to further improve forecasts of weather models.

1.3 Waves and oscillations

From bottom to the top, the atmosphere is a medium for the propagation of waves and oscillations on different temporal and spatial scales. These waves transport energy and momentum from their source region to their deposition region. There, the deposition of momentum and energy by breaking atmospheric waves forces the atmosphere away from its thermal equilibrium. The following gives a short introduction to the most relevant waves present in the middle atmosphere: Planetary waves, solar tides and gravity waves.

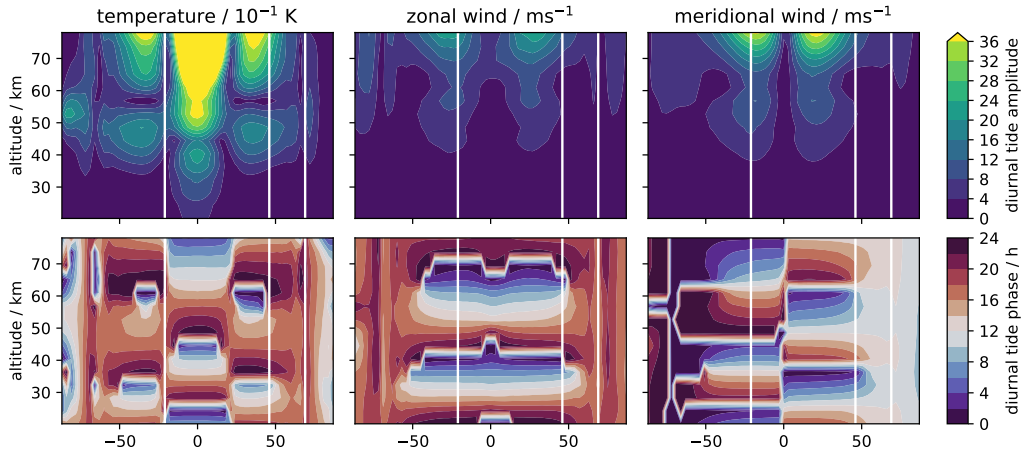

Figure 1.3 Amplitude and phase of the sun synchronous diurnal tide (altitude vs. latitude) in the temperature (note factor 10^{-1} in scale) and zonal and meridional wind field as modeled by the Global Scale Wave Model version 2000 (GSWM00). Marked with white lines are the campaign locations Andøya at 69 °N, Bern at 46 °N and La Réunion at 21 °S.

Planetary waves

So called Planetary or Rossby waves have a period of about 10 to 15 days and have a global extend. The restoring force is the Coriolis force. They are excited close to the ground due to the interaction of the mean flow with topography and the distribution of the continents. Planetary waves can only vertically propagate into the stratosphere during winter as they require westward (or weak eastwards) flow to propagate. Rossby waves at lower altitudes exist also in summer and have an effect on extreme weather conditions during northern-hemisphere summer (Coumou et al., 2014).

Planetary waves are the main driver of the dynamical variability in the stratosphere and mesosphere in northern hemispheric winter. Dunkerton, Hsu, and McIntyre, 1981; Matsuno, 1971 suggested, that the interaction between Planetary-waves and the mean flow is responsible for the sudden stratospheric warmings which occur regularly in the northern hemisphere. These events are dramatic warmings of the winter stratosphere which often include a temporary reversal of stratospheric wind speeds. Major sudden stratospheric warmings are assumed to not occur in the southern hemisphere, except for two single reported cases (Lewis, 2019; Varotsos, 2002), minor warmings have also been observed in austral winter 2019.

Under normal conditions in the northern hemisphere, planetary waves are apparent on mid- to high latitudes and form a meandering pattern of the polar vortex. On the southern hemisphere, where the ocean land distribution is different, these waves propagate and break at much lower latitudes. The region where the planetary waves break in the southern hemisphere is called the stratospheric surf zone and reaches even equatorial latitudes (McIntyre and Palmer, 1983; Shepherd, 2000). In figure 1.2, planetary waves appear on the southern hemisphere, visible as a meandering wave-structure of the global eastward jet.

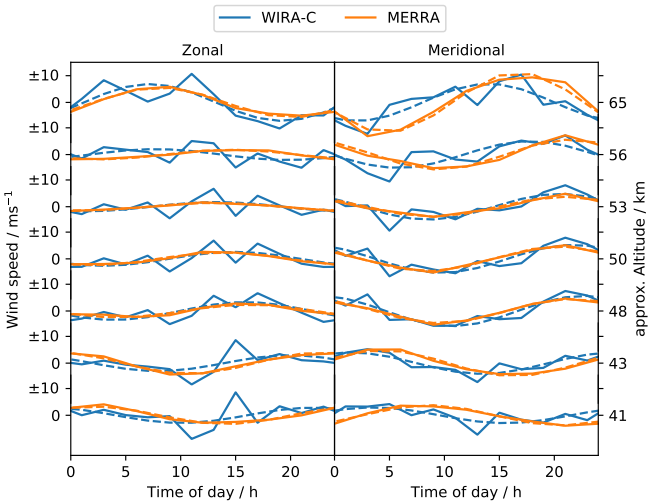

Figure 1.4 Diurnal tide in the zonal and meridional wind field on different altitude levels measured by WIRA-C on La Réunion (21 °S) for April to June 2017 and the corresponding data from the MERRA2 reanalysis model.

Solar tides

Solar tides are global scale waves with periods that are integer fractions of the solar day. They are excited by the diurnal cycle of insolation and propagate in the temperature and wind field on a global scale. Typically they are excited at or above the stratopause by solar heating and propagate upwards with increasing amplitude as air density drops. Eventually they break, creating secondary waves or dissipate, thus depositing energy and momentum. By doing so, they exchange energy between source and deposition region and thus provide a mechanism for the vertical coupling in the atmosphere. They are the dominant driver for dynamics in the upper mesosphere and lower thermosphere system (Forbes et al., 2008). While the period is forced by the solar day, the amplitude and phase are more complex to predict, as the tidal waves interfere with other waves (also with tides) while propagating on a global scale. The sun-synchronous tide is also referred to as migrating tide, as it migrates with the apparent westwards movement of the sun. Tides which are not sun-synchronous, are referred to as non-migrating tides. A global picture of the diurnal, migrating solar tide, which is the main component of the atmospheric tides spectrum, is shown in figure 1.3 on an altitude versus latitude plot. The data for this figure is from the Global Scale Wave Model version 2000 (GSWM00) by Hagan et al., 1999. It models the propagation and interference of the diurnal tide on a global scale, showing nodes of high and low amplitude over different latitudes. Generally, the amplitude is increasing with altitude, due to decreasing density and energy / momentum conservation. The phase is also variable with altitude, due to the vertical propagation of the tides. Additionally the phase has a clear latitudinal structure, which varies slightly over the course of the year.

Atmospheric tides are essential to understand the atmosphere as a whole. Their observation and modelling is therefor essential to monitor and predict atmospheric change (Lindzen, 1971; Lindzen and Chapman, 1969; Volland, 2012). The exact behaviour of tides on a sub-seasonal and local scale are topic of active research. Especially the variability of amplitude and phase within days and the exact phase relation between tides in

the temperature and wind field are topics of current atmospheric research. Baumgarten and Stober, 2019 observed the diurnal and semi-diurnal tide in the temperature field using lidar measurements and compared their phase to the tide in the wind field from reanalysis data. Continuous observation of tides in the middle atmosphere are rare, especially in the wind field. The first measurement of the diurnal tide in the wind field by ground based radiometry is shown in figure 1.4. In this figure, the increasing amplitude and phase shift with altitude due to upwards propagation of the diurnal tide can be seen. Details about the measurements can be found in Hagen et al., 2020a (chapter 6).

Gravity waves

On shorter timescales, with periods of hours down to minutes, gravity waves propagate in the atmosphere. Their restoring force is gravity. These waves are excited by disturbances in the troposphere like airflow over mountains and thunderstorms. Other sources include jet stream shear and adjustment processes in the atmosphere. Gravity waves propagate horizontally and vertically with wavelengths of a few to several hundred kilometers and transport energy and momentum from their source region.

Upwards propagating gravity waves grow in amplitude and eventually become unstable and break. The modes of propagation of gravity waves are filtered by the mean flow speed and direction. This wave filtering mechanism forces an asymmetry of gravity wave propagation between the summer and winter hemisphere which is responsible for the upwards flow and subsequent adiabatic cooling of the summer mesosphere, causing a corresponding downwards flow on the winter pole, forming an effective meridional transport, the so called residual circulation (Plumb, 2002).

1.4 Measurement of wind in the middle atmosphere

The following section gives an overview over wind measurements in the middle atmosphere. The presented techniques can roughly be divided into three categories: in-situ, remote active and remote passive. The most important measurement techniques are visually summarized with their respective altitude range in figure 1.5.

In-situ measurements in the middle atmosphere, are delivered by sounding balloons and rocket sounding campaigns. Balloon soundings are only available at the lowest part of the middle atmosphere, as they only reach altitudes up to 35 km. Additionally, radio soundings provide accurate temperature, pressure and sometimes ozone measurements. Weather balloons are launched once or twice a day from many stations around the earth and their data is assimilated in most weather models and reanalyses, for example by the Modern-Era Retrospective analysis for Research and Applications – Version 2 (MERRA2). Newman et al., 2016 used radiosonde wind measurements to study the 2015-2016 anomaly in the quasi-biennial oscillation (QBO).

In-situ observations at higher altitudes are only achievable by sounding rocket campaigns. For example, tides in the middle atmosphere have been measured by repeated rocket soundings (Lindzen and Chapman, 1969) and general properties of horizontal winds have been observed in the Mesosphere and Lower Thermosphere (MLT) region (Müllemann and Lübken, 2005). Since sounding rockets provide high-resolution data during their upwards and downwards flight they are also capable of capturing small-scale effects like turbulence in the Mesosphere and Lower Thermosphere (MLT) region (Strelnikov et al., 2017).

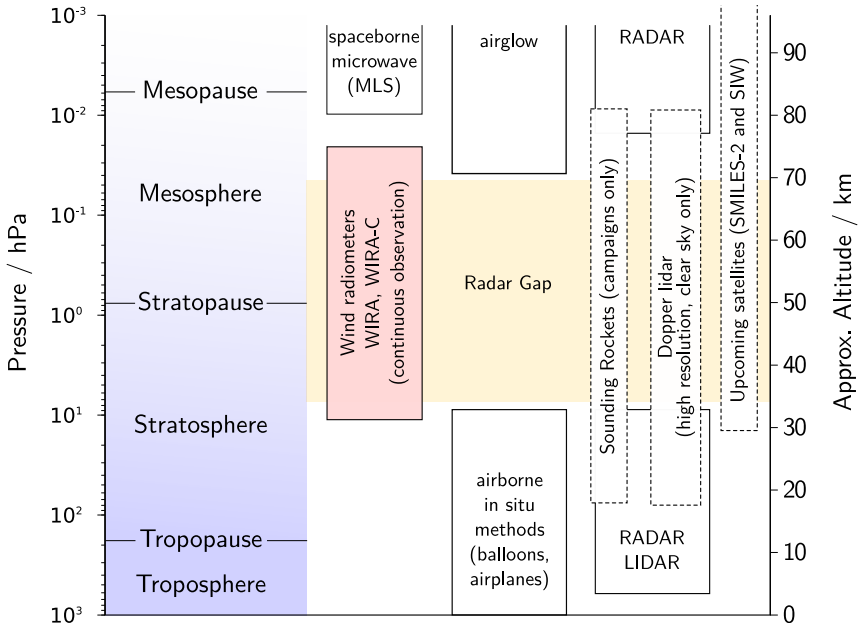

Figure 1.5 Overview over different measurement methods for wind in the atmosphere (blue). The region covered by WIRA and WIRA-C (red) overlaps with the so called radar gap (yellow), where no other continuous observations are currently available.

Remote exploration of dynamics in the middle-atmosphere is particularly difficult. Active techniques like radar and lidar rely on the presence of an atmospheric back-scatterer. In case of radar, this can be density differences or particles in the troposphere, meteor trails in the mesosphere or fluctuations in electron density in the ionosphere. Such scatterers are very sparse between 30 and 70 km altitude which is why this altitude range is often referred to as the *radar-gap*.

Rayleigh/Mie/Raman (RMR)-lidars can measure wind speeds (and temperature) in this region using high power lasers and large telescopes to measure the Doppler shift of back-scattered light (Baumgarten, 2010; Souprayen et al., 1999; Yan et al., 2017). Lidars deliver point in time measurements of wind profiles with a high resolution. The Arctic Lidar Observatory for Middle Atmosphere Research (ALOMAR) lidar is daylight-capable and delivers wind profiles up to 80 km altitude with an altitude resolution of a few 100 m (Baumgarten, 2010). Due to the decreasing density of molecular backscatterers and the inverse-square law of light, the uncertainties of the lidar measurements increase with altitude. Because lidars need clear-sky conditions to operate, long period observations (longer than 10 days) are rare. Other lidar systems like the Maïdo lidar on La Réunion are only night-time capable and deliver wind profiles up to 60 km (Khaykin et al., 2016). The advantage of lidar systems clearly is their high spatial and temporal resolution, which is enough to resolve fine-scale structures like gravity waves. The disadvantage however is, that they rely on clear-sky conditions and in practice often only provide a snapshot of the atmospheric state rather than continuous observations.

Meteor radars are active sounders which measure the back-scattered signal from meteor trails. Such meteor trails come from the plasma formed around a meteoroid entering the Earth's atmosphere when the particles have a sufficient high kinetic energy to reach the vaporization temperature. In the upper mesosphere, such meteor trails are ubiqui-

tous since the Earth is constantly bombarded by meteorites and the atmosphere is dense enough to ablate them by frictional heating. Metor radars are sensitive to wind down to approximately 80 km altitude. The Doppler shift induced to the meteor trail echoes give information about the wind speed. Meteor radars take advantage of timing information and synthetic aperture antennas and can thus exactly locate the origin of the echo. Thus they can actually produce two-dimensional maps of wind fields in the upper mesosphere down to approximately 80 km (Stober et al., 2018; Wilhelm, Stober, and Brown, 2019). A network of meteor radars, distributed around the earth can be used to retrieve exact planetary wave propagation parameters (Stober et al., 2017). By measuring the ambipolar diffusion coefficient they can also retrieve the temperature field in these altitudes (Stober et al., 2008).

The Microwave Limb Sounder (MLS) instrument on the NASA EOS/Aura satellite was capable to measure wind in the mesosphere and lower thermosphere region by using the Doppler-shifted oxygen line at 118 GHz (Wu et al., 2008). Further, geostrophic wind can be derived from MLS geopotential height measurements (Matthias and Ern, 2018). This requires the assumption of an exact balance between Coriolis force and pressure gradient force, which does not hold exactly in the atmosphere. Nevertheless, outside of the tropics, geostrophic winds are a good approximation of the actual wind field and provide a valuable source for comparison data (Rüfenacht et al., 2018). The ADM/Aeolus mission launched a space-borne lidar to measure tropospheric and lower stratospheric wind speeds up to 25 km altitude in 2018 (Reitebuch, 2012). Notably no operational satellite instruments to date provide direct wind measurements in the radar-gap between 30 and 75 km altitude. New satellites are being proposed to fill this gap, namely the microwave instruments SIW (Chalmers, 2018) and SMILES2 (Baron et al., 2019).

1.5 Atmospheric models

Atmospheric models, especially those focused on weather prediction and climate research are mainly concerned with the troposphere and the lower stratosphere. In the last decade, a general trend to elevated model-tops has been observed with models providing data also for the middle atmosphere, that is up to 80 km. How well the modelled quantities agree with measurements in these altitudes is subject of current research (Blanc et al., 2019; Pichon et al., 2015; Rüfenacht et al., 2018).

The European Centre for Medium-Range Weather Forecasts (ECMWF) provides an operational analysis of the atmospheric state modelled on 137 layers up to 80 km altitude. The main focus lies on delivering data on the atmospheric layers below 35 km for weather forecasts. Especially above 68 km the data quality is supposed to decrease because the uppermost layers, so called sponge layers, are artificially forced to achieve model stability. ECMWF assimilates radiosonde data and other measurements, whereby the concrete assimilation scheme is not available to the public. The model includes different schemes of gravity-wave parameterization to accurately model the middle-atmospheric mean-zonal flow and up- and down-welling (Orr et al., 2010). Also the exact behaviour and implementation of the so called sponge layers is not published.

The Modern-Era Retrospective analysis for Research and Applications – Version 2 (MERRA2) is the reanalysis produced by NASA's Global Modeling and Assimilation Office (GMAO). It is focused on the modern satellite era, and assimilates many different satellite observations (Gelaro et al., 2017). Among them is the MLS instrument on the EOS/Aura satellite

which provides temperature and ozone data also in the middle atmosphere. Apart from this satellite, there is no data assimilated in the middle atmosphere. Airplane temperature data, radiosonde data and surface measurements are assimilated in the troposphere.

In general, the performance of current operational models in the middle atmosphere is not well known. On one hand, it is clear that the models focus on weather and climate, and comparing their output to surface data thus has priority. On the other hand, there is evidence that a better understanding of middle atmospheric dynamics and better constraints by measurements in this region can improve the overall model performance, especially in the context of extreme events (Baldwin et al., 2003; Coumou et al., 2014).

Performing observations in the middle atmosphere to benchmark and improve global circulation models thus brings immediate social and economic benefits.

1.6 The ARISE2 project

In the previous sections it has been outlined, that dynamic processes in the middle atmosphere have a direct impact on weather and extreme weather situations. However, limited observations of the middle-atmosphere restrict the ability to constrain these processes in numerical weather models. The goal of the ARISE2 (Atmospheric dynamics Research InfraStructure in Europe 2) project is to combine existing observational networks with complementary technologies to provide advanced data products covering the middle atmosphere, which can be used to improve and benchmark weather models. The ARISE2 project[1] was funded with 3.2×10^6 € under the European Commissions Horizon 2020 framework program, taking place between September 2015 and August 2018. It was an international collaboration, with partners from 24 institutes from 17 countries, which built upon the grounds of the fist ARISE project.

Specifically, the goal of the ARISE2 project was to integrate complementary observational networks and technologies to provide a comprehensive and consistent set of middle atmospheric observational data. To cover the entirety of relevant spatial and temporal scales of dynamics in the middle atmosphere as illustrated in figure 1.6, it is essential to combine a variety of instruments (and models), each of which having specific strengths and limitations. These technologies and networks include

- the infrasound International Monitoring System (IMS) developed for the Comprehensive Nuclear-Test-Ban Treaty (CTBT) verification,
- the lidar Network for the Detection of Atmospheric Composition Changes (NDACC),
- multi-instrument reference stations equipped with lidar systems (ALOMAR in northern Europe, OHP at middle latitude, Maïdo in the tropics)
- radiometers,
- complementary infrasound networks,
- radars and
- satellite observations.

[1] http://arise-project.eu, last visited 2020-05-11

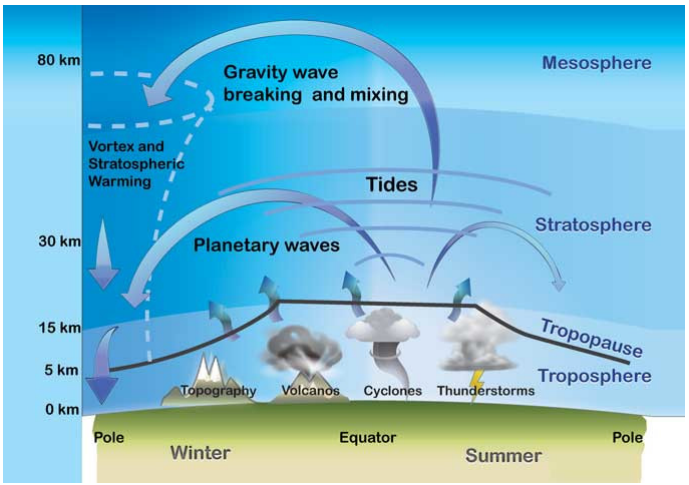

Figure 1.6 Waves on different temporal and spatial scales play an important role in atmospheric dynamics. Figure adapted from Blanc et al., 2018, (CC-BY).

With this multi-technology approach, it is possible to effectively fill the gap of measurements in the middle atmosphere as no single technology is able to provide a full picture of dynamics in this domain by its own. With this integrative approach, it is possible to better describe dramatic events like stratospheric warmings and their impact to extreme weather in the northern hemisphere, tides, weather related disturbances (tropical convection, mountain waves), gravity waves and their impact on vertical coupling as well as to improve predictability and modeling of natural hazards such as volcanos, severe weather or meteoroids, as all these are directly or indirectly coupled to the middle atmosphere. Blanc et al., 2018 describes the main ARISE2 results.

2 Microwave wind radiometry

Microwave radiometry observes rotational transition lines of atmospheric molecules in the microwave spectrum. It is one of the very few measurement techniques that is sensitive to the middle atmosphere from 30 to 70 km altitude and is also able to provide altitude resolved profiles in this altitude region. Since a long time it has been used to remotely measure the mixing ratio of atmospheric constituents like ozone or water vapour (e.g. Lobsiger, 1987; Nedoluha et al., 1995).

Using the Doppler shift of transition lines to observe wind speeds has already been proposed by Clancy and Muhleman, 1993 and they specifically proposed measurements of the 230 GHz mesospheric CO emission at high latitudes to measure mesospheric wind speeds. Later, Burrows, Martin, and Roberts, 2007 used this technique to measure mesospheric wind speeds using an Antarctic CO radiometer. Flury et al., 2008 used air-borne measurements of the 183 GHz water vapour emission lines and a narrow band fast Fourier transform spectrometer (FFTS) to prove the feasibility of wind measurements in the stratosphere. Shah, Muhleman, and Berge, 1991 used a millimeter wave instruments to observe the wind on Venus, where the Doppler shift is larger due to higher wind speeds than on Earth.

With the WIRA ground-based Doppler microwave wind radiometer, Rüfenacht, Kämpfer, and Murk, 2012 (also Rüfenacht et al., 2014) proved the feasibility of wind measurements in the middle atmosphere, especially also for long term continuous observations. Given the lack of observation methods covering this altitude region, continuous measurements and monitoring of middle atmospheric wind speeds provide a new opportunity for atmospheric research.

Baron et al., 2013 published Dopper microwave wind measurements performed by the Superconducting Submillimeter-Wave Limb-Emission Sounder (SMILES) onboard the Internatioal Space Station (ISS). Unfortunately this instrument stopped operation in 2014 and no more wind measurements are available. The concept of microwave Doppler wind measurements is also applied to space exploration, for example with the ESA Jupiter Icy Moon Explorer (JUICE) mission with the Submillimeter Wave Instrument that is planned to launch in 2022 (Suess, 2014).

Observations of wind speeds in the middle-atmosphere have been used to characterize oscillations in the wind field with periods from weeks down to approx. 5 days (Rüfenacht, Hocke, and Kämpfer, 2016). Further, observations with Doppler microwave instruments and co-located Doppler lidar measurements are invaluable to compare and validate middle atmospheric wind speeds between measurements and models (Rüfenacht et al., 2018). And, in the frame of the ARISE2 project, various sounding techniques including Doppler

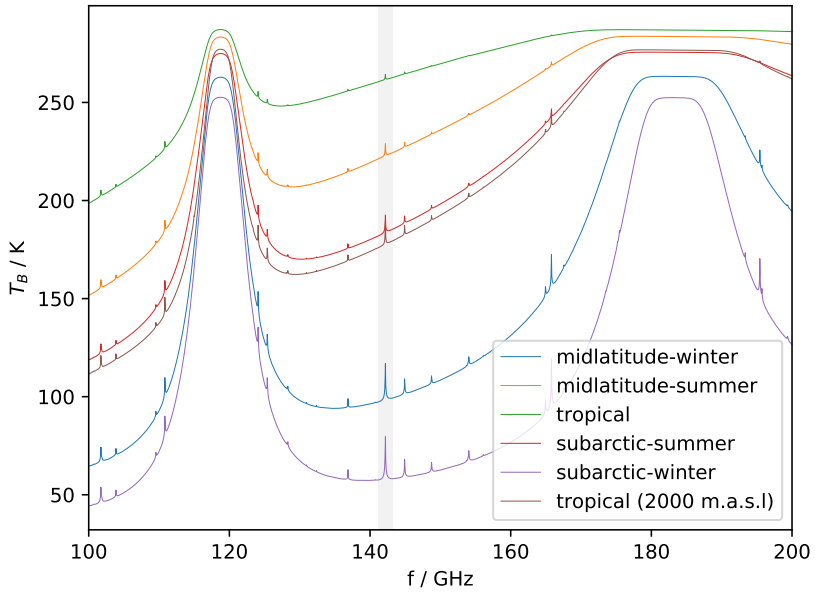

Figure 2.1 Microwave emission of water vapor, oxygen (O_2) and ozone (O_3) simulated for different climatologies and an instrument at 500 m.a.s.l looking at an elevation angle of 22°. The 142 GHz emission line of ozone is located between the oxygen line (118 GHz) and water vapour line (183 GHz).

microwave radiometry and infrasound have been used to characterize uncertainties of atmospheric models in the middle atmosphere (Blanc et al., 2019).

The existing ground-based instruments WIRA and WIRA-C can deliver middle atmospheric wind profiles in an altitude range of approx. 30 to 75 km with an altitude resolution of approx. 12 km and a temporal resolution of 12 to 24 hours. Thus, wind radiometers have been primarily used for the monitoring of background wind speeds since they are unable to resolve oscillations shorter than a few days. Rogers et al., 2016 employed multi-year composite retrievals of different ozone radiometers to measure the diurnal cycle of mesospheric winds. Hagen et al., 2020a used 7 to 13 day composites to retrieve diurnal tide amplitude and phases in the middle atmosphere. This demonstrates the feasibility of continuous observation of atmospheric tides using ground-based microwave radiometry.

Co-located ground-based microwave measurements of ozone, water-vapour and wind have been used to get a comprehensive picture of middle atmospheric chemistry, dynamics and short-term variability in polar latitudes (Schranz et al., 2019a,c). These studies showed that the observation of multiple species in the middle atmosphere helps to understand the highly variable atmosphere in polar regions.

2.1 Measurement principle

2.1.1 Microwave radiation in the atmosphere

Matter with a temperature greater than absolute zero emits thermal radiation. For a perfect blackbody in thermal equilibrium, the emitted energy is distributed over all fre-

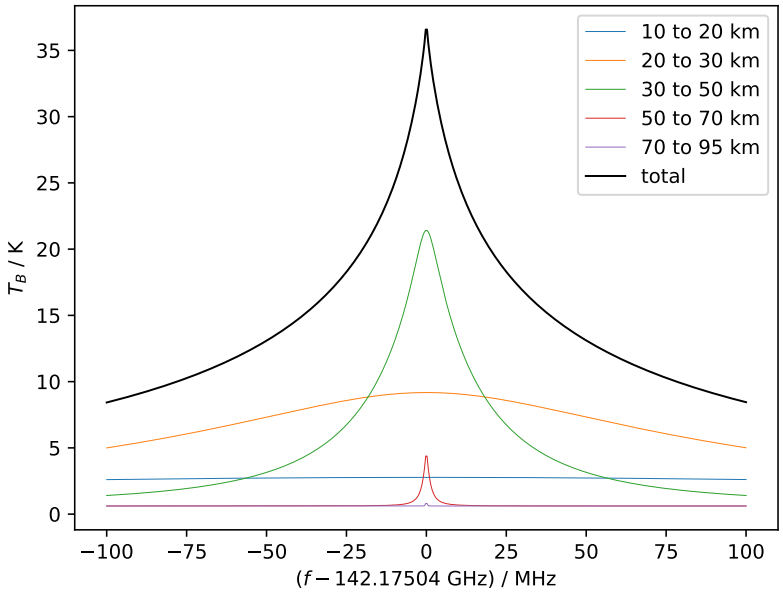

Figure 2.2 Emission line of ozone at 142.17504 GHz as seen at 10 km altitude (total) and the contributions from different altitude levels. Emission lines from lower altitudes are pressure broadened. Contributions from upper altitudes are more narrow and also weaker due to lower density of ozone molecules.

quencies according to Plank's law. For example, a blackbody at 300 K would emit its radiation primarily at wavelengths of a few micrometers (infrared) but also radiates at other wavelengths. If the emitter is not a blackbody, the emitted spectral radiance is equal to the radiance of a blackbody multiplied with the frequency dependent emissivity. For an object emitting and absorbing in thermal equilibrium, its emissivity is equal to its absorptivity according to Kirchhoff's law.

Molecules with a rotational asymmetry have different rotational energy states and transitions between these states enable the molecule to absorb and emit radiation at certain frequencies that are proportional to the energy difference of the transition states. As a result, each species has a typical thermal emission and absorption spectrum that features certain lines where the absorptivity and emissivity are high.

In passive microwave radiometry, this rotational emission of the molecules is measured at wavelengths between roughly 1 m (300 MHz) and 1 mm (300 GHz). Figure 2.1 shows the simulated emission spectrum of ozone (O_3), water vapour and oxygen between 100 and 200 GHz as it would be seen from ground under an elevation angle of 22 deg. The emission line of ozone at 142.17504 GHz is the strongest emission line of ozone in this range. It is in the local minimum of the continuum, between the water vapour line at 118 GHz an the oxygen line at 183 GHz. The contribution from the continuum is dominated by tropospheric water vapour. Making observations during winter, in arctic latitudes or at higher elevation above sea-level is beneficial because of an increased signal-to-noise ratio due to increased line amplitude as can be seen from the same figure.

In theory, these emission lines are infinitely narrow. Natural broadening due to the quantum mechanical uncertainty principle and the uncertainty in the lifetime of the states can be neglected for remote sensing applications. Doppler broadening (not the same as Doppler shift) occurs because molecules in a gas are in constant motion and the air speed is randomly distributed according to the Maxwell-Boltzmann distribution.

The most important broadening effect is the pressure broadening effect (sometimes also called collisional broadening). Collisions between molecules affect the lifetime of their energy states and thus broaden the emission line. Because this broadening is pressure dependent, it allows the retrieval of altitude resolved profiles. Figure 2.2 shows simulated lines from different altitudes. The total of these lines is the superposition that an instrument would see from the ground. The core idea behind the retrieval of profiles by ground-based radiometry is to decompose the measured spectrum into the different contributions from different altitudes using the pressure broadening effect.

Up to an altitude of approximately 75 km, the pressure broadening effect is dominating all other broadening effect. At higher altitudes, Doppler broadening becomes the dominant effect and the retrieval of altitude resolved profiles is no longer possible.

At altitudes below 30 km the emission lines become so broad, that the signal-to-noise ration drops rapidly and the ability to retrieve information is constrained by instrumental limitations. For example the finite bandwidth of the spectrometer limits the ability to cover very broad lines. Reflections on optical elements (e.g. the calibration target) cause non-linear base-line effects which cannot be separated from a very broad line with low amplitude. At higher altitudes, the Doppler broadening effect dominates over the pressure broadening and restricts the ability to resolve altitude information. Thus, radiometric applications which resolve altitude by pressure broadening are best suited for measurements in the middle atmosphere.

To model microwave radiation in the atmosphere, we use the Atmospheric Radiative Transfer Simulator (ARTS) (Buehler et al., 2018). This is a community radiative transfer model that has been developed to accurately model emission spectra of molecules and their propagation through an atmosphere as well as modeling different radiometers and spectrometers.

2.1.2 Wind radiometry

Passive ground-based wind radiometry is based on the Doppler shift imposed on emission lines due to the relative speed between air-molecules and observing radiometer. Due to the pressure broadening effect, the retrieval of altitude resolved wind-profiles is possible. This requires the capability to measure the emission line with a high spectral resolution.

The Doppler shift

$$\Delta\nu = \frac{v_{\text{los}}}{c}\nu_0 \tag{2.1}$$

describes the linear relation of observed frequency shift $\Delta\nu$ to the speed of the emitter along the line of sight v_{los}, relative to the observer. The Doppler shift is proportional to the observation frequency ν_0. We are interested in the horizontal wind speeds $v_{u,v}$ which depend on the elevation angle of the line-of-sight η as

$$v_{\text{los}} = v_{u,v}\cos\eta + v_z\sin\eta \approx v_{u,v}\cos\eta \tag{2.2}$$

The approximation in equation (2.2) is possible because in the middle atmosphere, vertical wind speeds v_z are typically 2 to 3 orders of magnitude lower than horizontal wind speeds.

Because of this projection relation, it is advantageous to observe at low elevation angles for wind measurements. Nevertheless, the observation angle has to be chosen so that it is still above the horizon and the troposhoeric signal is not dominating the middle-atmospheric contribution. An elevation of 22° has been proven to be a good compromise in practice and has thus been used for all wind radiometers.

At an observation frequency of 142 GHz and a typical middle-atmospheric horizontal wind speed of 100 ms^{-1}, at an elevation angle of 22°, the observed Doppler shift is 43 kHz. A difference in wind speed of 10 ms^{-1}corresponds to a difference in Doppler shift of 4.3 kHz. Because the observed frequency shift is so small, a stable frequency reference is important for wind radiometry. To compensate for drifts and offsets that do not come from wind signals, it is advantageous to observe opposing directions (North, South, East and West). This makes it possible to discriminate between instrumental shifts (same in both directions) and Doppler shifts (opposite in both directions).

The ozone emission line at 142.17504 GHz is especially suited for Doppler wind radiometry for the following reasons: Firstly, the emission line is at a relatively high frequency, which proportionally increases the observed Doppler shift. At the same time, the frequency is low enough that low-noise amplifiers are commercially available to build a highly sensitive radiometer front end. Secondly, the 142 GHz emission line is located at a local minimum of atmospheric emission between the 118 GHz water vapor line and the 183 GHz oxygen line as can be seen in figure 2.1. And finally, ozone is present in the whole atmosphere, with a maximum in volume mixing raio between 20 and 60 km. With only very little ozone being present in the lower atmosphere, the troposphere is nearly transparent to this frequencies. This makes it an ideal tracer for ground-based observations of middle atmospheric wind.

2.2 The WIRA-C instrument

The Wind Radiometer for Campaigns (WIRA-C) instrument has been built at the Institute of Applied Physics, University of Bern in 2015. Figure 2.3 shows the instrument as it has been deployed at the Maïdo observatory on La Réunion.

The instruments dimensions are $0.6 \times 0.75 \times 0.5$ m and all the components are placed inside a single housing, that is mounted on a tripod. It is very compact and portable, only requiring power and ethernet to operate at any place. Once setup, it measures autonomously over months and provides the possibility for remote control and maintenance. This makes WIRA-C ideal for campaigns as well as long-term continuous observations.

Technically, it is a highly sensitive single side-band microwave radiometer which measures the 142 GHz ozone emission line with a high spectral resolution of 12 kHz over a bandwidth of 160 MHz. The receiver electronics are uncooled but actively temperature stabilized. The instrument contains an internal calibration target at ambient temperature and a GNSS-disciplined reference clock for long term stability of the frequency reference.

Some distinguished technical highlights of WIRA-C include:

- All in one compact housing, only requiring power and internet

Figure 2.3 The WIRA-C instrument as deployed at the Maïdo observatory on La Réunion. All the components are integrated in one compact housing.

- Low-noise pre-amplified single-sideband receiver
- Low receiver noise temperature of instrument (512 K)
- Microwave components are actively temperature stabilized
- Path-length modulator mitigates standing waves
- Wedge load as internal low reflectivity calibration target
- Ultra-low side-lobe corrugated feed horn
- All-sky capability
- Automatic rain protection (with power backup)
- Automatic drying / cleaning of exposed mirror
- Tilt sensor for leveling
- Real-time preview of calibrated spectra
- Heated airflow for humidity control (corrosion protection)

2.2.1 Receiver optics

A view on the mechanical setup of WIRA-C is given in figure 2.4 with labels for the respective parts. Radiation from the atmosphere enters through the scan-drum and is deflected by the flat mirror M3. The scan drum is used to select the elevation angle of the

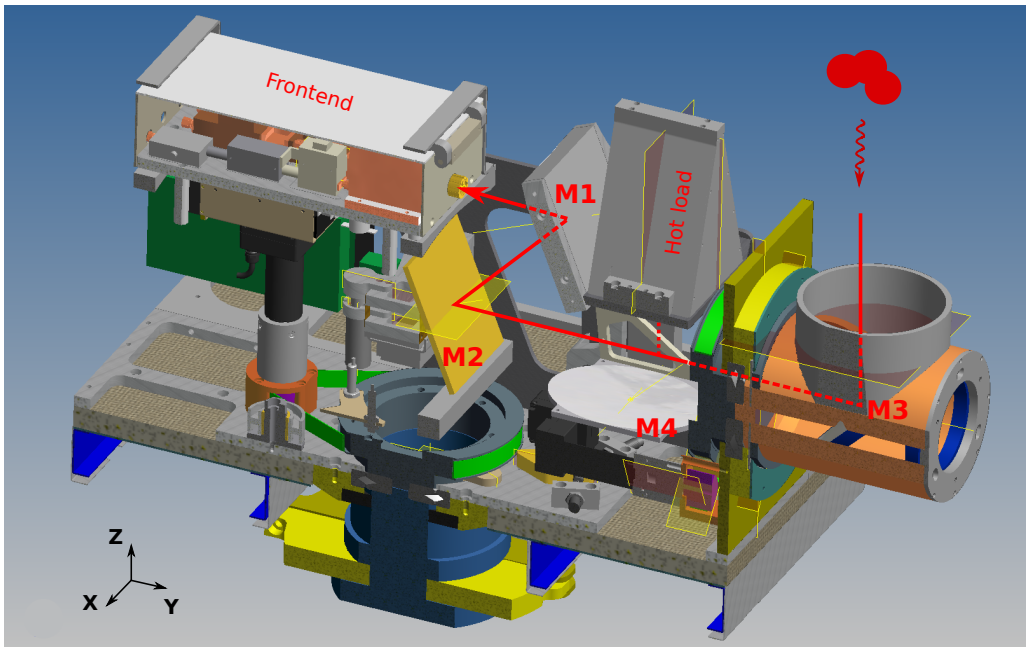

Figure 2.4 Overview of the mechanics in WIA-C. The optical system includes the scan-drum with mirror M3, the path-length modulator M2, the slewable elliptic mirror M4 and the elliptic reflector M1 that couples the instrument beam to the antenna inside the frontend. The whole instrument is mounted on an azimuthal drive.

observation and together with the azimuthal drive below the instrument, it is effectively possible to observe the whole sky. The flat mirror M2 is placed on a linear stage and can be moved in order to make a $\lambda/4$ difference in optical path length between two measurements. This mechanism is usually referred to as wobbling when done in a continuous motion or path-length modulation when done in discrete steps like for WIRA-C. The path-length modulation is used to mitigate standing waves by destructive interference of resonance patterns in the spectrum.

The elliptic mirror M1 couples the beam into the antenna of the frontend. It defines the Half Power Beam Width (HPBW) of the instrument that is 2.3° which is effectively a pencil-beam. A narrow beam allows to exclusively observe a certain part of the atmosphere and limits the contribution from higher and lower layers especially at low elevation angles.

For calibration, the slewable elliptic mirror M4 can be engaged and couples the antenna to the ambient temperature (hot) load (see section 2.2.3).

2.2.2 Receiver electronics

A schematic of the WIRA-C receiver electronics is shown in figure 2.5. The electronics are split in a front- and a backend part. The frontend is a pre-amplified single-side band heterodyne receiver that mixes down the radio frequency (RF) of around 142 GHz down to an intermediate frequency (IF) band that is centered around 3.65 GHz. The first amplifier in the chain is a low noise amplifier (LNA) that amplifies the incoming signal and noise by 20 dB (factor 100). Its noise figure is critical for the noise of the whole system, as it is the first active component. This LNA has been built by the Fraunhofer IAF based on

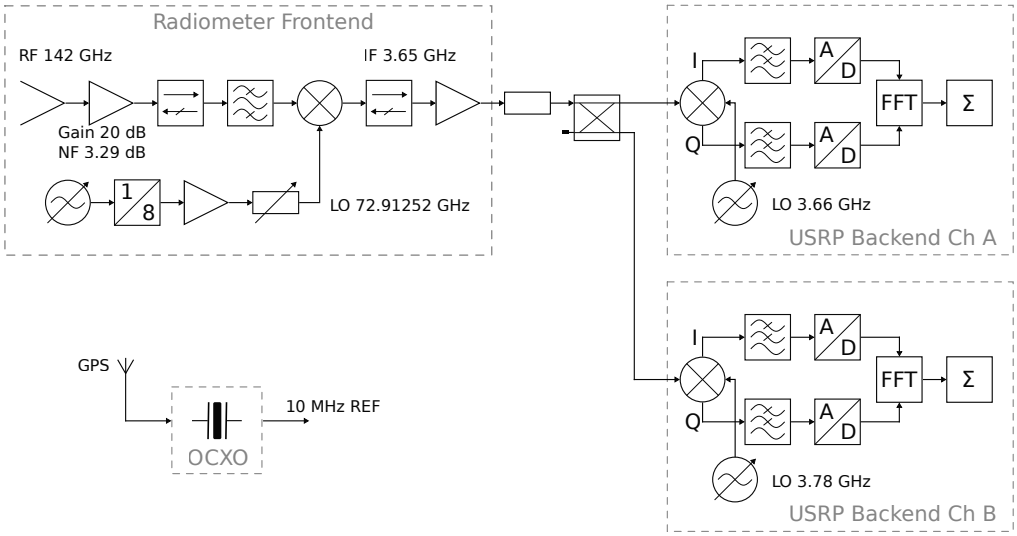

Figure 2.5 Schematic of the WIRA-C frontend and backend.

the 50 nm M-HEMT technology described by Leuther et al., 2012. The very piece built into WIRA-C has the minimum of its noise figure of 3.29 dB at 140 GHz (at 293 K) which which coincides with our observation frequency of 142 GHz.

The subharmonic mixer down-converts the amplified signal to an intermediate (IF) frequency band centered around 3.65 MHz. This IF signal is then fed to the backend.

As a backend, WIRA-C uses a software defined radio from Ettus Research Inc., the USRP X310 with two CBX-120 daughter boards. This backend has two independent channels which can be configured individually. Each channel uses an IQ-mixer for base band conversion and an analog to digital converter (ADC) with a sampling rate of 200 MHz. Because of the filter characteristics in the base band converter, only approximately 160 MHz of the total bandwidth are usable for radiometric observations. The USRP has a Xilinx FPGA embedded, which is programmed to do the Fast Fourier Transform and accumulation using Labview Real-Time.

Because the IF input matching of the USRP CBX-120 daughter boards is not perfect and causes reflections, we implemented an attenuation of 10 dB between the frontend and the backed to mitigate standing waves between the IF amplifier and the input stage of the USRP. Without this attenuation, we observed a strong baseline, caused by non-linear effects caused by these reflections and their interaction with the input stage of the CBX-120.

2.2.3 Calibration

Compactness and low maintenance requirements were major design goals of WIRA-C. This is why we opted for an ambient temperature load complemented with the tipping curve method for the radiometric calibration. Essentially, this method has been explained by Han and Westwater, 2000 and uses the sky as cold load. We determine the opacity of the sky τ_{trop} by measuring at two elevation angles , which in our case are $\eta_1 = 22°$ and $\eta_2 = 90°$ (zenith). It is crucial here to average two opposite directions, in order to include

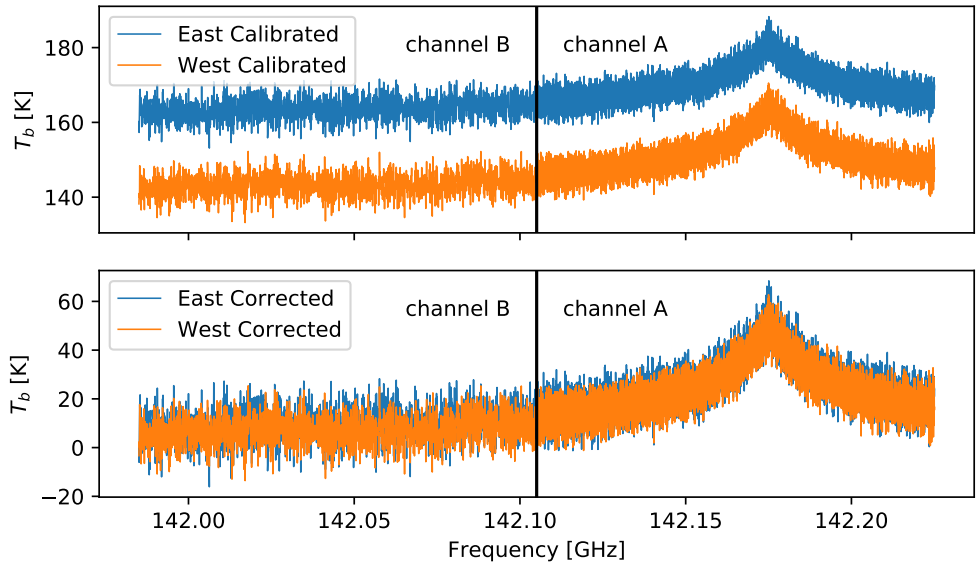

Figure 2.6 Measured spectrum of the ozone line. Top panel shows the eastward and westward measurement after calibration, bottom panel shows the same measurement but with tropospheric correction ap- plied. Channel A of the USRP has 12.2 kHz resolution and is cen- tred around the line centre while channel B has 97.7 kHz resolution and, in this case, observes the line wing. Figure from Hagen et al., 2018.

as little wind information in the calibration process as possible. Preferably, we average north and south observations as the meridional wind is weaker than the zonal wind.

The following calibration is applied for each frequency bin separately. It is thus applicable to a single channel or in a vectorized form for a full spectrum.

The brightness temperature T_b is related to the measured power U by the radiometer equation

$$T_b = \frac{1}{G_{\text{rec}}} U - T_{\text{rec}} = aU - b. \tag{2.3}$$

On the other hand, the brightness temperature of the atmosphere can be approximated by the zenith opacity τ and a tropospheric mean temperature $T_{m,i}$, depending on elevation angle η_i as

$$T_b = T_b^{\text{bg}} \exp\left(\frac{-\tau}{\sin \eta_i}\right) + T_{m,i}\left(1 - \exp\left(\frac{-\tau}{\sin \eta_i}\right)\right) \tag{2.4}$$

As suggested by Ingold, Peter, and Kämpfer, 1998, we derive the tropospheric mean temperature from the surface temperature T_{s} as $T_{m,1} = T_{\text{s}} - 9.8$ K and $T_{m,2} = T_{\text{s}} - 10$ K at 142 GHz (choosing $T_{m,1} = T_{m,2} = T_{\text{s}} - 10$ K would be a valid approximation). The cosmic background temperature is included with $T_b^{\text{bg}} = 2.7$ K. The contribution from the upper atmospheric layers is included in the opacity τ, which will have a frequency dependence. Because these layers are optically thin compared to the troposphere and wind retrievals are rather insensitive to absolute calibration, the approximation with a

tropospheric mean temperature is appropriate and can be considered in the uncertainty budget (Hagen et al., 2018, Table 2).

By combining equation (2.3) and equation (2.4) for the hot load measurement and the atmospheric observations with i being the the index of different elevation angles $\eta_1 = 22°$ and $\eta_2 = 90°$, we get

$$T^{\text{hot}} = aU^{\text{hot}} - b \tag{2.5}$$

$$T_{b,i} = aU_i - b = T_b^{\text{bg}} \exp\left(\frac{-\tau}{\sin\eta_i}\right) + T_{m,i}\left(1 - \exp\left(\frac{-\tau}{\sin\eta_i}\right)\right). \tag{2.6}$$

By substitution, we get rid of b:

$$b = aU^{\text{hot}} - T^{\text{hot}} \tag{2.7}$$

$$T_{b,i} = a\left(U_i - U^{\text{hot}}\right) + T^{\text{hot}} \tag{2.8}$$

We solve equation (2.8) for a, which leaves us with two equations (one for $i = 1$ and one for $i = 2$):

$$a = \frac{1}{U_1 - U^{\text{hot}}}\left[T_b^{\text{bg}} \exp\left(\frac{-\tau}{\sin\eta_i}\right) + T_{m,1}\left(1 - \exp\left(\frac{-\tau}{\sin\eta_i}\right)\right) - T^{\text{hot}}\right] \tag{2.9}$$

Both observations should yield the same receiver coefficient a and we use equation (2.9) for $i = 1$ and $i = 2$, to get an equation with τ as the only unknown:

$$\begin{aligned}\frac{1}{U_1 - U^{\text{hot}}}\left[T_b^{\text{bg}} \exp\left(\frac{-\tau}{\sin\eta_1}\right) + T_{m,1}\left(1 - \exp\left(\frac{-\tau}{\sin\eta_1}\right)\right) - T^{\text{hot}}\right] = \\ \frac{1}{U_2 - U^{\text{hot}}} T_b^{\text{bg}} \exp\left(\frac{-\tau}{\sin\eta_2}\right) + T_{m,2}\left(1 - \exp\left(\frac{-\tau}{\sin\eta_2}\right)\right) - T^{\text{hot}}\end{aligned} \tag{2.10}$$

Factoring out the exponential terms gives us the final equation:

$$0 = c_0 + c_1 \exp\left(\frac{-\tau}{\sin\eta_1}\right) - c_2 \exp\left(\frac{-\tau}{\sin\eta_2}\right) \tag{2.11}$$

where

$$c_0 = \frac{T^{\text{hot}} - T_{m,1}}{U^{\text{hot}} - U_1} - \frac{T^{\text{hot}} - T_{m,2}}{U^{\text{hot}} - U_2} \tag{2.12}$$

$$c_1 = \frac{T_{m,1} - T_b^{\text{bg}}}{U^{\text{hot}} - U_1} \tag{2.13}$$

$$c_2 = \frac{T_{m,2} - T_b^{\text{bg}}}{U^{\text{hot}} - U_2} \tag{2.14}$$

The equation (2.11) has no analytical solution but is typically convex for the opacities of interest and can thus be solved numerically by applying a simple Newton iteration. The solution τ^* is the zenith opacity which describes best our measurements. By substituting back, we also get the radiometer gain G_{rec} and radiometer noise temperature T_{rec} and the radiometer is calibrated.

Figure 2.7 The WIRA instrument at the ALOMAR observatory, Andenes, Norway. Photography by Rolf Rüfenacht.

After calibration, the spectra are in units of brightness temperature. Before one can retrieve wind speeds from a measurement, it has to be processed further, namely applying a tropospheric correction and integrating over an appropriate timespan. The details of the data processing are given by Hagen et al., 2018. Figure 2.6 shows an example of a measured spectrum for one calibration cycle (about 5 minutes) for opposing directions (east and west) with and without tropospheric correction applied.

2.3 The WIRA instrument

The WIRA (Wind Radiometer) instrument has been built at the Institute of Applied Physics, University of Bern in 2010 (shown in figure 2.7). It has been designed as a prototype and proved the ground based microwave wind radiometry to be possible. Rüfenacht, 2015 discussed it extensively in his thesis and we will only highlight the most important differences to WIRA-C here.

The WIRA instrument has originally been built as a double sideband receiver system and has later been upgraded to a pre-amplified single sideband receiver. Now, the receiver chain, including frontend and backend are similar to those of WIRA-C. It uses the same low noise amplifier (LNA) in the frontend and the same USRP in the backend. By chance, the LNA has a slightly higher noise-figure than the one in WIRA-C, which increases the noise temperature by approx. 200 K compared to WIRA-C.

The optical parts of WIRA, including mirrors, pyramidal-plate calibration load and feed horn are exposed to weather. Especially the calibration target needs some time to dry off after rainfall.

The microwave components are protected against weather by a plastic cap over the upwards pointing feed horn. In late December 2018, a crow picked the cap and water entered the receiver chain during the next rainfall. This caused a longer downtime of the instrument, with the need to replace amplifier and mixer in the receiver chain to recover the instrument.

Compared to WIRA-C, WIRA does not have a path-length modulator and is more restricted in its possible viewing directions. Further, it has a long IF cable running from the instrument to the backend-rack in the laboratory. This is not necessarily a disadvantage, as the baseline issues caused by reflections on the USRP input stage are not observed on WIRA.

2.4 Modelling and Optimal estimation

The radiative transfer model describes the relation between the atmospheric state vector x and the measurement vector y as $x = F(y)$. The inversion thereof is typically ill-posed because many (unphysical) configurations of the atmosphere lead to the same measured brightness temperature. The optimal estimation method uses a priori values with associated uncertainties to regularize the inverse problem (Rodgers, 2000).

WIRA and WIRA-C measure the brightness temperature in four different cardinal directions and an ideal retrieval combines all observations to fit one atmospheric state.

Different retrieval setups have been used in the course of this thesis:

v1 Retrieve every direction separately. Calculate difference of final atmospheric states.

v2 Retrieve zonal and meridional wind separately (Hagen et al., 2018).

v3 Retrieve one atmospheric state that fits all observations.

While all of the retrieval versions provide high-quality wind profiles, the improvement form v1 to v2 is manly an advantage for averaging kernels and quality control parameters. By combining all (or at least two opposing) observations in one inversion, we can effectively maximize the a posteriori likelihood of the wind profile given our four measurements in all cardinal directions. This is especially important in the presence of frequency shifts or drifts that are not related to wind. Such shifts are of systematic or random nature and can originate from instrumental instabilities or offsets or even uncertainties in the molecular resonance frequency.

The improvement from v2 to v3 is rather technical. Instead of iterating 2 times (for zonal and then for meridional) we can iterate only once and retrieve the full atmospheric state in one go. This improves performance and simplifies the retrieval process.

In the following, the retrieval v3 is described. The text is adapted from Hagen et al., 2018, with changes for the v3 retrieval where necessary.

In case of WIRA-C retrieval v3, the state vector $\vec{x}$ and the measurement vector $\vec{y}$ have the following form for the wind retrieval:

$$\vec{x} = \begin{bmatrix} \vec{u} & \vec{v} & \vec{x}_{\mathrm{O_3}} & \Delta f & \vec{b} \end{bmatrix}^\intercal \tag{2.15}$$

$$\vec{y} = \begin{bmatrix} \vec{T}_{b,\mathrm{east}} & \vec{T}_{b,\mathrm{west}} & \vec{T}_{b,\mathrm{north}} & \vec{T}_{b,\mathrm{south}} \end{bmatrix}^\intercal \tag{2.16}$$

where the elements of $\vec{x}$ are itself vectors. For example the zonal wind speed profile is given by $\vec{u} = \begin{bmatrix} u(p_1) & u(p_2) & \dots & u(p_N) \end{bmatrix}$ for N pressure levels. Besides the zonal and meridional wind profile $\vec{u}$ and $\vec{v}$, the $\vec{x}$ vector also contains the profile of volume mixing ratio of ozone $\vec{x_{\mathrm{O_3}}}$ as well as the frequency shift parameter Δf and one or more baseline parameters $\vec{b}$. Finally, the brightness temperatures $\vec{T_{b,\dots}}$ are the calibrated and corrected brightness temperatures observed in the respective directions.

The retrieval of ozone profiles is a by-product of the wind retrievals, because the bandwidth of the high resolution spectrometer used for wind measurements is not large enough to allow the retrieval of high-quality ozone profiles. Nevertheless, by applying a frequency-agile spectrometer technique, the bandwidth can be expanded for ozone retrievals. This technique is described in detail in Hagen et al., 2020b (see chapter 7).

The optimal estimation method then minimizes the cost function

$$\chi^2 = (\vec{\hat{x}} - \vec{x_a})^\intercal \mathbf{S}_a{}^{-1} (\vec{\hat{x}} - \vec{x_a}) + (\vec{y} - F(\vec{\hat{x}}))^\intercal \mathbf{S}_\epsilon{}^{-1} (\vec{y} - F(\vec{\hat{x}})) \tag{2.17}$$

for finding the most probable atmospheric state $\vec{\hat{x}}$ given the a priori profile $\vec{x_a}$ and the measurement $\vec{y}$. The a priori profile $\vec{x_a}$ is constructed analogously to the atmospheric state $\vec{x}$ using climatology or model data. The inversion uses the assigned statistics in form of the covariance matrices $\mathbf{S}_a$ and $\mathbf{S}_\epsilon$ for the a priori data and the measurement respectively.

They are constructed as block diagonal matrices, analogous to the $\vec{x}$ and $\vec{y}$ vectors in equation (2.15) and equation (2.16):

$$\mathbf{S}_a = \begin{bmatrix} \mathbf{S}_{a,u} & & & & & \\ & \mathbf{S}_{a,v} & & & & \\ & & \mathbf{S}_{a,X_{\mathrm{O_3}}} & & & \\ & & & \mathbf{S}_{a,\Delta f} & & \\ & & & & \mathbf{S}_{a,b} \end{bmatrix} \tag{2.18}$$

$$\mathbf{S}_\epsilon = \begin{bmatrix} \mathbf{S}_{T_{b,\mathrm{east}}} & & & \\ & \mathbf{S}_{T_{b,\mathrm{west}}} & & \\ & & \mathbf{S}_{T_{b,\mathrm{north}}} & \\ & & & \mathbf{S}_{T_{b,\mathrm{south}}} \end{bmatrix} = \sigma_y \, \mathbb{I} \tag{2.19}$$

The value σ_y on the diagonal of $\mathbf{S}_\epsilon$ is directly determined as the Allan-deviation of the measurement vector $\vec{y}$ by $\sigma_y^2 = \frac{1}{2}\langle(\vec{y}_{n+1} - \vec{y}_n)^2\rangle$.

Following Rodgers, 2000 and using a linearised form of the forward model with Jacobian $\mathbf{K}$, the solution that minimizes equation (2.17) in a linear case is

$$\vec{\hat{x}} = \vec{x}_a + \mathbf{G}(\vec{y} - \mathbf{K}\vec{x}_a) \tag{2.20}$$

where $\mathbf{G}$ is the gain-matrix and describes the sensitivity of the retrieved profile to changes in the spectra:

$$\mathbf{G} = \frac{\partial \vec{\hat{x}}}{\partial \vec{y}} = \left(\mathbf{K}^T {\mathbf{S}_\epsilon}^{-1} \mathbf{K} + {\mathbf{S}_a}^{-1}\right)^{-1} \mathbf{K}^T {\mathbf{S}_\epsilon}^{-1}. \tag{2.21}$$

Since the frequency shift introduced by wind has a non-linear impact on the brightness temperature, the final solution $\vec{\hat{x}}$ is found by a Levenberg–Marquardt algorithm and equation (2.20) is applied iteratively while updating the point of linearisation for $\mathbf{K}$ but leaving $\vec{x}_a$ fixed.

Assuming that $\mathbf{S}_\epsilon$ characterizes the radiometric noise on the spectra, the uncertainty of the retrieved profiles due to thermal noise, the so called observational error σ_o, is defined as

$$\sigma_\mathrm{o}^2 = \mathrm{diag}\left(\mathbf{G}\mathbf{S}_\epsilon\mathbf{G}^T\right). \tag{2.22}$$

We assume that the major contribution to the uncertainty on the retrieved profiles is due to radiometric noise and thus use the observational error σ_o as a measure for the uncertainty. It is important to note, that the observational error is influenced by the a priori statistics via equation (2.21) and the observational error grows with increasing a priori covariance because then the measurement and its noise have a bigger impact on the retrieved quantity. We accept this as an inherent property of the optimal estimation method: For a given thermal noise on the spectrum, the uncertainty of the retrieved value is smaller if there is less ambiguity in the a priori state.

Another measure for quality of our retrieved state $\vec{\hat{x}}$ is the averaging kernel matrix given by

$$\mathbf{A} = \frac{\partial \vec{\hat{x}}}{\partial \vec{x}} = \mathbf{G}\mathbf{K}. \tag{2.23}$$

Each row of the matrix A is called an averaging kernel and describes the smoothing of information.

The forward model and OEM implementation is provided by ARTS (version 2.3) (Buehler et al., 2018). A big advantage of the OEM over other regularisation methods is the availability of quality control parameters from $\mathbf{A}$ in (2.23). A representative set of such parameters is shown in figure 2.8. The effective limitations in altitude range, altitude resolution and altitude accuracy can readily be derived from these parameters. For WIRA-C, with an integration time of 12 hours, the altitude resolution is around 10 km (according to the Full Width at Half Maximum) and the offset in altitude information is lower than 5 km. A detailed uncertainty budget, including the estimation of possible random and systematic sources of uncertainty is included in Hagen et al., 2018 (see chapter 5).

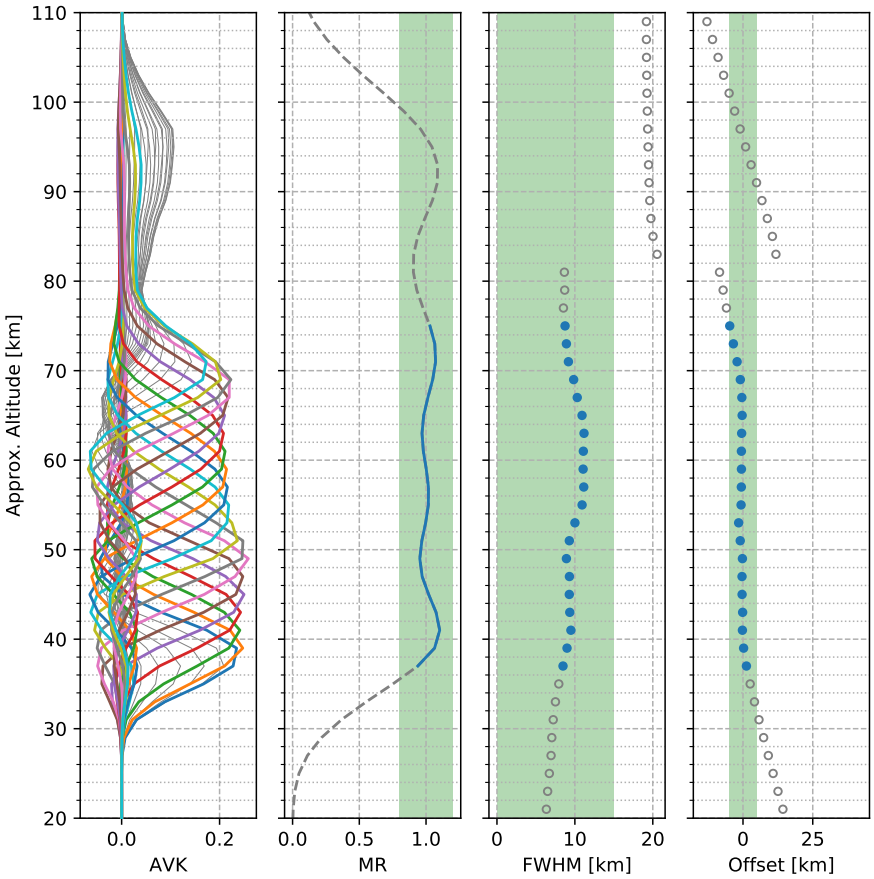

Figure 2.8 Visualisation of the averaging kernel matrix (AVKM) for WIRA-C. The individual aver aging kernels (rows of the AVKM) for each altitude are characterized by the measurement response (MR), their full width at half maximum (FWHM) and the difference of their maximum to the nominal height (Offset). The valid ranges for all parameters are marked by the green areas. Valid components that fulfill all criteria are shown in colours and others in gray (or dashed lines and hollow markers, respectively). Figure and description from Hagen et al., 2018.

3 Aim and impact of this thesis

As outlined in chapter 1, dynamics in the middle atmosphere have a direct impact on weather and extreme weather on Earth's surface (Baldwin et al., 2003; Shaw and Shepherd, 2008). Better constraints on stratospheric initial conditions would improve the forecasting capabilities of numerical weather prediction models (Charlton et al., 2004). Further, long term stratospheric trends have an impact on climate change on the surface (Manzini et al., 2014). Thus there is a need for a more comprehensive image of middle-atmospheric dynamics.

Creating the community to provide the required products to gain further insight to middle-atmospheric dynamics is the goal of the European Comission's Horizon 2020 projects ARISE and ARISE2 and the candidate project ARISE-IA [1]. The core idea of this project is, that complementary measurements can deliver the required insight to middle-atmospheric dynamics if organized in a collaborative network. This collaboration and diversity of instruments and methods is required, as no method alone is able to provide observations on all relevant scales by itself (Blanc et al., 2018).

Passive microwave Doppler wind radiometry provides long-term continuous measurements of horizontal wind speeds between 30 and 70 km where no other continuous wind measurements are available to date.

In the long run, such measurements could be assimilated by models directly, or provide auxiliary data for other measurements. For satellites with a sun-synchronous orbit, this would be measurements of the diurnal tides which are aliased due to the orbit. For infrasound, this includes long-term background wind speed measurements which are needed to model infrasound propagation.

The goals of this thesis can thus be summarized as follows:

- Characterize WIRA-C performance for middle-atmospheric wind measurements
- Reproduce and improve upon the WIRA prototype
- Acquire time-series of middle-atmospheric wind speeds at different latitudes
- Compare wind profile measurements to lidar measurements
- Compare WIRA-C measurements to models and reanalyses data sets
- Further develop passive microwave wind radiometry

[1] http://arise-project.eu, see also section 1.6

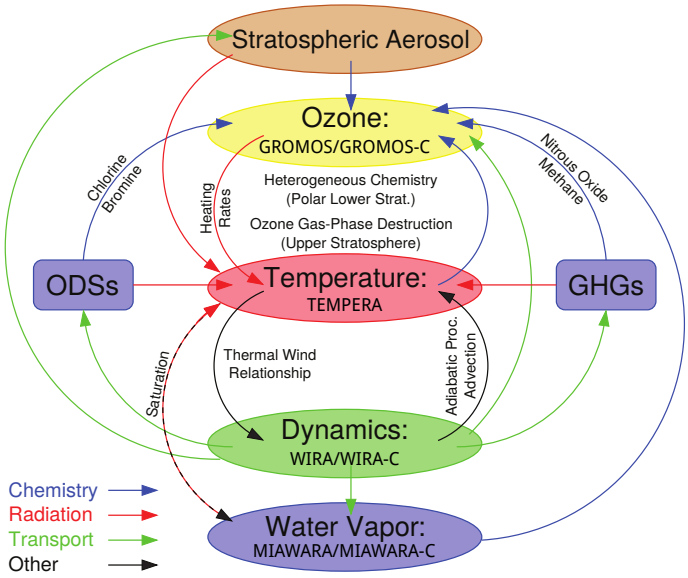

Figure 3.1 Links between atmospheric constituents and dynamics. Wind has a direct impact on the other constituents by transport. Names of microwave instruments from the Institute of Applied Physics are annotated below the respective quantities they are able to measure. Figure from N. Kämpfer, modified by F. Schranz.

The Institute of Applied Physics in Bern has a long history in passive radiometer development for various applications, in particular also for ground-based atmospheric observations. In the past 30 years, many instruments for passive ground-based atmospheric observations have been developed at the institute. Figure 3.1 illustrates interactions between different players in the atmosphere. Wind acts on all other chemical species like ozone, water vapor, ozone depleting substances (ODSs) and green-house gases (GHGs) by transport. Many of the atmospheric constituents shown in this figure can be measured by microwave radiometry and specifically by instruments built at the Institute of Applied Physics in Bern. Namely these are GROMOS and GROMOS-C for ozone monitoring, TEMPERA for temperature measurements, MIAWARA and MIAWARA-C for measuring middle-atmospheric water vapour and WIRA and WIRA-C for wind measurements. Ozone and water vapor radiometers have a long history at the institute of Applied Physics in Bern, while wind radiometers are very recent developments.

The advantage of radiometry (be it wind, temperature, ozone, water vapour) is its capability to operate autonomously and mostly independent of weather conditions over decades with stable quality. Thus microwave radiometry can even provide data for trend studies (Bernet et al., 2019). Low vertical and temporal resolution are the main weaknesses of passive microwave wind radiometry when compared to other technologies like lidar. In combination with highly accurate, but point-in-time snapshot measurements like balloon and rocket soundings and lidar measurements as well as other techniques such as infrasound and radar systems, a comprehensive middle-atmospheric research infrastructure can be envisioned.

4 Campaigns

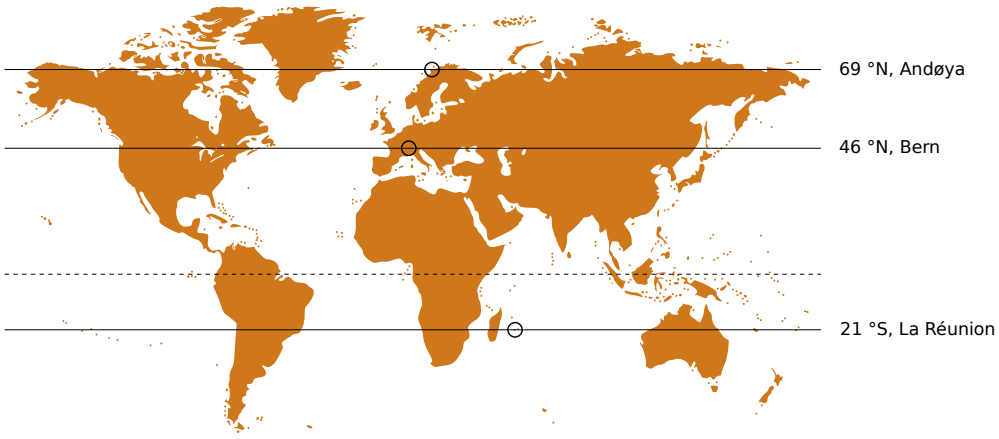

Figure 4.1 World map with the three campaign locations: ALOMAR on Andøya at 69 °N, Bern at 46 °N and Maïdo on La Réunion at 21 °S.

This chapter presents and summarizes the three campaigns of the wind radiometers WIRA-C and WIRA which took place in the last years. The campaign locations are spread across different latitudes: La Réunion (indian ocean) in the tropics, Bern (Switzerland) at mid-latitudes and Andøya (Norway) within the arctic circle as mapped in figure 4.1.

The distribution of campaigns over different latitudes enables the observation of different middle atmospheric effects which are typical for the respective latitude. For tropical latitudes this would be the stratospheric surf zone with planetary wave braking and for polar latitudes this would for example be sudden stratospheric warmings. The following chapters present wind measurements in the context of such dynamics.

Each campaign location has a specific climatic environment that has an influence on radiometric measurements. In figure 2.1, the emission lines of ozone as simulated by ARTS is shown for different latitudes. This figure shows, that the amplitude (difference of tip to wing brightness temperature) of the ozone line is larger at polar and mid-latitudes than in the tropics, but comparable to a station in the tropics at over 2000 m above sea level.

Figure 4.2 shows the zenith opacity for the three different campaign locations aggregated by month and hour of day. It is the result of the calibration routine described in section 2.2.3 (denoted as τ) at 142.125 GHz (50 MHz off the ozone line center). The mid-latitude and arctic sites (Bern and ALOMAR) show a clear annual cycle with high opacities in the summer months. At the Maïdo observatory, which is located at 2200 m.a.s.l, the

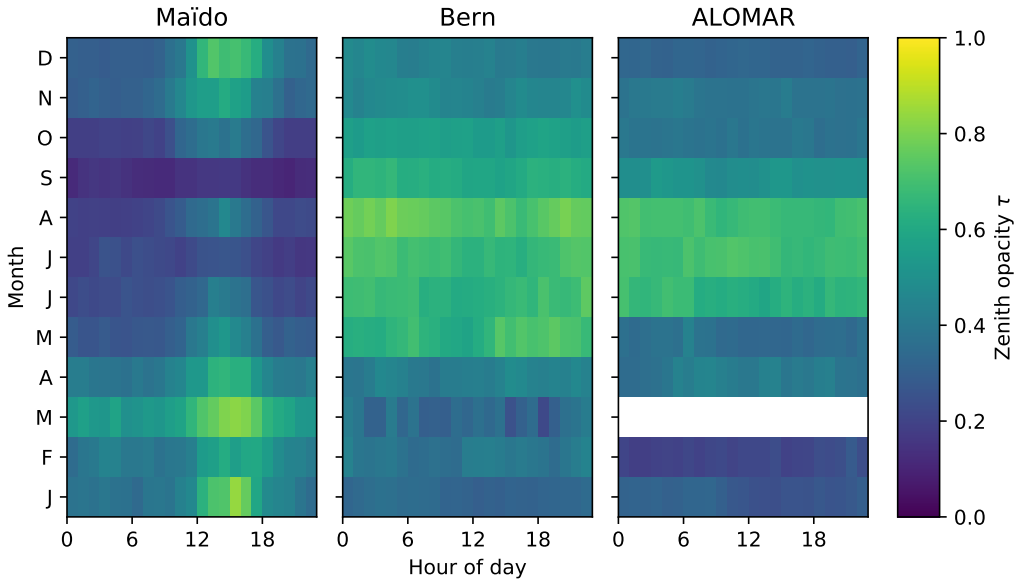

Figure 4.2 Zenith opacity at line wing, obtained from the tipping curve calibration from WIRA-C and WIRA for the three campaign locations aggregated by month and mean local solar time.

diurnal cycle due to tropical (and micro-climatic) weather patterns is readily visible. It is most pronounced during austral summer (December to March) with the maximum in opacity visible in the afternoon, when mist and thick clouds enwrap the vcolcanic summits of La Réunion island. At mid and polar latitudes, while a diurnal cycle of water vapour concentration exists (e.g. for Bern Hocke et al., 2019), its influence is apparently small at 142 GHz and averaged out when aggregating whole months. Ideal conditions for radiometric observations are found in (austral and boreal) winter. The rate of rainfall is another limiting factor to radiometric observations since observations are not possible when the optical components are covered by highly absorbing water. This cannot directly be seen from the opacity shown in figure 4.2, as the measurements are interrupted if rain is detected.

4.1 WIRA-C: La Réunion

The first long-term campaign of WIRA-C took place in the frame of the ARISE2 project at the Maïdo observatory on La Réunion (French overseas department) from 2016 to 2018. The exact dates and coordinates of the campaign are listed in table 4.1.

On La Réunion (21 °S), a tropical island in the indian ocean, the Maïdo observatory is located at the slope of an inactive volcano crater, at 2200 m.a.s.l. At these altitudes, the observatory is close to the free troposphere and provides optimal conditions for optical and quasi-optical atmospheric observations. The observatory is a multi instrument reference station to the ARISE2 project and hosts a variety of instruments, including a temperature and wind lidar and an infrasound array. Figure 4.3 shows the WIRA-C instrument on the roof of the Maïdo observatory.

As it was the first long-term campaign of WIRA-C, the Maïdo campaign was focused on testing the instrument as well as performing a first validation against models and lidar measurements. Specifically, the goals of this campaign are summarized as follows:

- Perform long-term continuous measurements over the course of at least a full year
- Retrieve a continuous time-series of horizontal wind in the middle-atmosphere
- Test the WIRA-C design (hardware / algorithms) in a tropical environment with high humidity and daily rainfall
- Observe seasonal cycle of middle atmospheric wind in the tropical region, including planetary wave activity
- Perform comparisons with the Doppler wind lidar at the Maïdo observatory
- Contribute data to the ARISE2 data-portal project for cross-comparison and validation

Figure 4.6 and figure 4.7 show the timeseries of zonal and meridional wind measured during the Maïdo campaign of WIRA-C with a time resolution of 12 hours. Over the course of the 17 months campaign, approximately 12 months have been measured continuously after a failure of the WIRA-C frontend has been fixed. The figures also contain analysis data from the European Centre for Medium-Range Weather Forecasts (ECMWF). On one panel, the ECMWF data is convolved with the averaging kernels and adjusted for the temporal resolution of WIRA-C to provide a qualitative reference. Further, also the raw ECMWF operational analysis is shown. These observations show the manifestation of some interesting atmospheric processes.

For example, one can see the atmospheric wind reversal around equinox in March 2017 from the westwards regime changing to the eastwards regime and back (November 2018). While

Location	Maïdo Observatory, La Réunion, Indian Ocean, France
Coordinates	21 °S, 55 °E
Altitude	2158 m.a.s.l
Period	2016-08-28 to 2018-07-27
Duration	17 months

Table 4.1 Coordinates and dates of the Maïdo Campaign of WIRA-C.

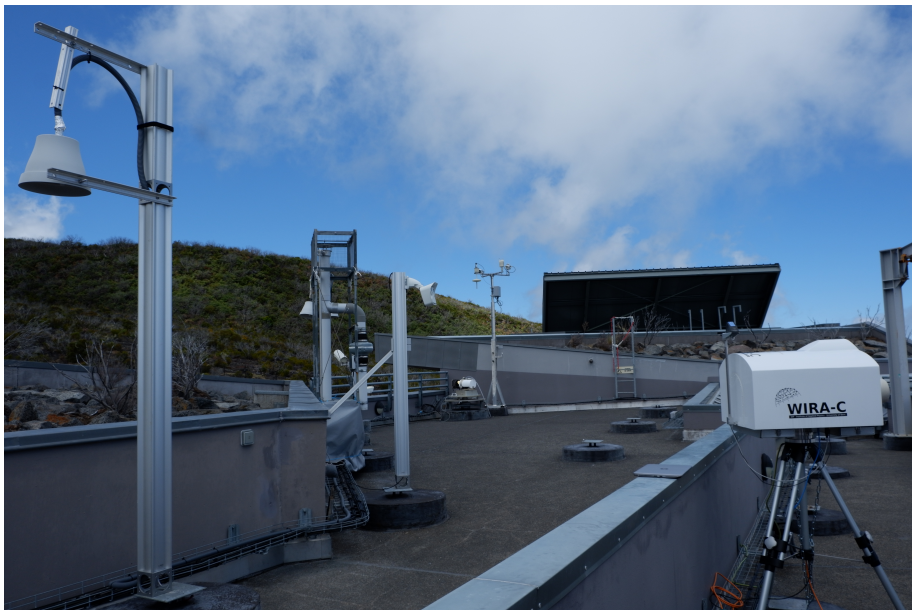

Figure 4.3 WIRA-C on the roof of the Maïdo observatory on La Réunion. In the background are various other instruments, mostly for air-quality and meteorological observations. Also in the background is the partially open hatch of the lidar system. Photography by Patrick Hupe.

the change in March occurs in a downward-propagation, the reversal in austral spring is more instantaneous and happens on the whole observed altitude range at the same time. This feature is also represented in the ECMWF model data. A more detailed comparison of measurements and models is contained in (Hagen et al., 2018), and shows that the ECMWF operational model and WIRA-C measurements agree well when comparing the 12 hourly averages. The differences between model and measurements are mostly within the estimated uncertainty of the measurements. Even in the context of strong planetary wave activity (as described below), the model is able to capture the dynamics and agrees with the measurements.

In July and August 2018, the zonal wind speed features a strong oscillation with a period of approximately 10 to 15 days where the eastward flow is interrupted by short periods of westward flow. Corresponding patterns of meridional wind enhancements are also evident during this period (figure 4.7). This is due to the planetary scale Rossby waves, which reverse the wind speed locally in the whirl of their breaking region. Due to the different distribution between ocean and land in the southern hemisphere, these waves reach much closer to the equator than in the northern hemisphere. Figure 4.4 shows this phenomenon in a global context with the wind and temperature field as modeled by ECMWF during these events. The waves are visible as patches in the meridional wind field or as wave-like structure in the zonal wind field in the global view.

Another highlight of the Maïdo campaign was the possibility to compare our measurements with the Rayleigh–Mie Doppler wind lidar (Khaykin et al., 2016) that is located at the Maïdo observatory. Figure 4.5 shows seven coincident measurements of the Doppler wind lidar and WIRA-C together with ECMWF operational model data and radio soundings. While the lidar measurements represent point-in-time measurements with observation times between 3 and 10 hours, WIRA-C measures continuously and the integration time for one profile has been set to 12 hours. Immediately apparent is the difference in

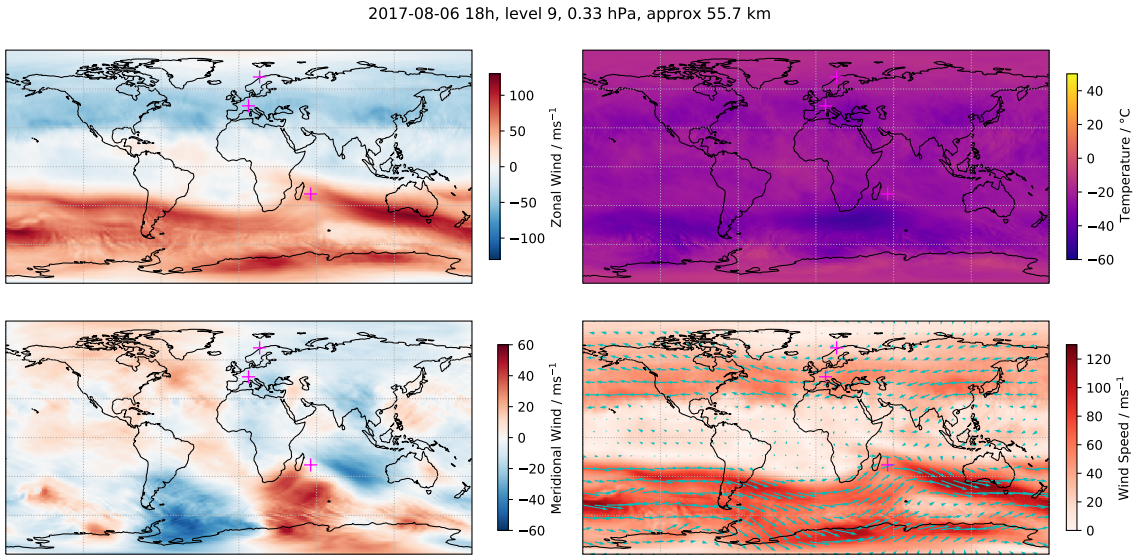

Figure 4.4 Rossby-waves reach tropical latitudes in the southern hemisphere: Zonal wind speed (top left), meridional wind speed (bottom left), temperature field (top right), wind magnitude and direction (bottom right) form ECMWF analysis data at level 9 (55 km altitude). All three campaign locations (La Réunion, Andøya, Bern) are marked for reference.

altitude resolution for the two instruments. While the lidar is able to capture small scale variations, which might come from gravity waves, WIRA-C presents a much smoother profiles. For longer integration times of the lidar (for example 9.7 hours on 2017-06-22), the profiles agree well within their respective uncertainties.

The data of this campaign has been contributed to the ARISE2 data portal[1], where the zonal and meridional wind speed product is available to the public.

The results of this campaign can be summarized in the following points:

- WIRA-C is capable to deliver continuous wind profile measurements with 12 hours temporal and 10 to 15 km vertical resolution in an altitude region from 30 to 75 km
- The stratospheric wind reversal around equinox can be observed
- Planetary wave activity in austral winter can be observed (Earth's largest breaking waves!)
- ECMWF model data and WIRA-C measurements agree well
- Comparison with coincident lidar wind profiles show that the two instruments agree well
- Lidar and WIRA-C measurements agree best for longest lidar integration times
- ECMWF model indicates diurnal variability in wind speeds of a few ms^{-1}(lidar is only capable to measure during night time)
- The measurement data has been contributed to the ARISE data portal

[1]The ARISE data portal is accessible online: arise-portal.eu

The variability of the middle atmosphere within a day as seen in models and also by previous lidar campaigns, gave rise to further questions. When comparing short lidar measurements to continuous WIRA-C measurements, the short term variability in the wind field has to be considered. Especially the variability of tidal waves in the wind field and their possible impact to measurements of any kind (lidar, sattelite, infrasound and microwave) was identified as a topic of interest to the community.

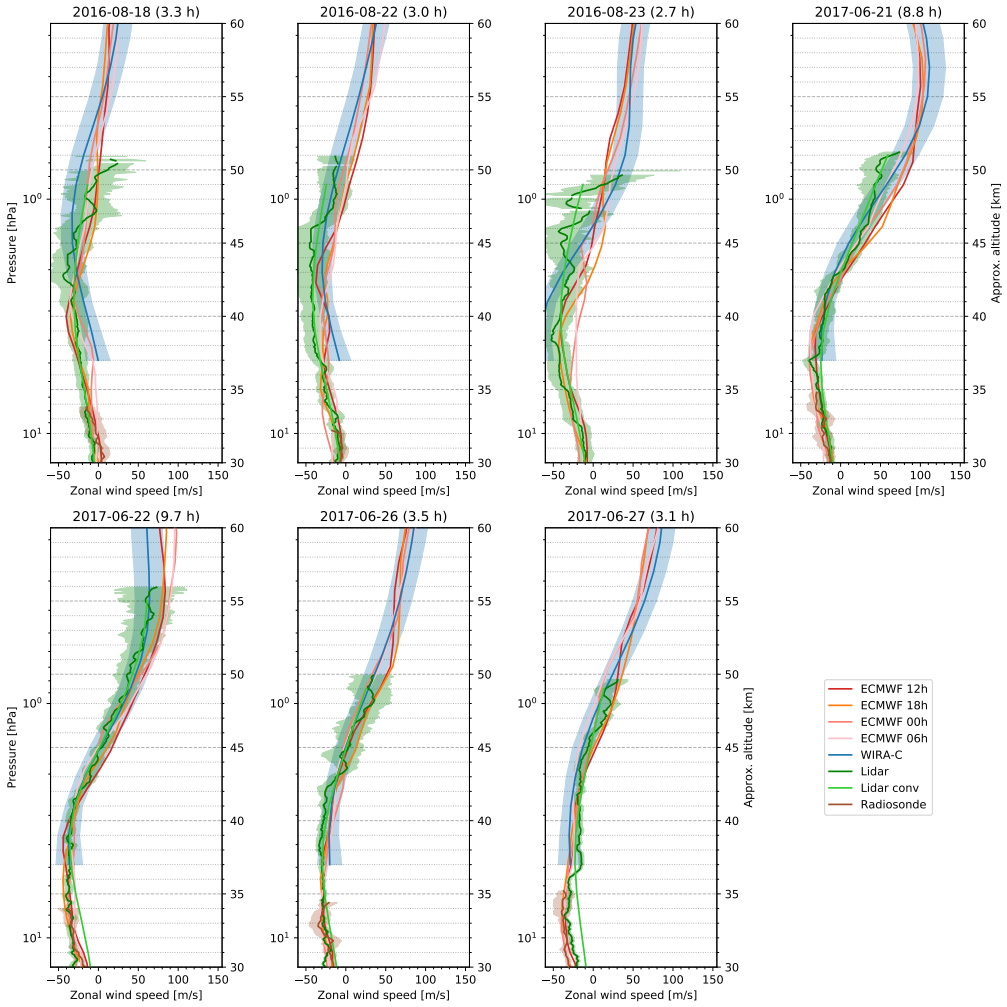

Figure 4.5 Seven coincident observations of zonal wind from WIRA-C and Doppler lidar from August 2016 and June 2017 together with radio soundings and ECMWF operational model data at different times, WIRA-C measurements start at 14:00 UT (18:00 LT) and lidar measurements typically between 17:00 and 20:00 UT (21:00 and 24:00 LT). The integration time for WIRA-C is 12 h for every profile while the measurement time for the lidar observation (given in parenthesis) is typically between 3 and 3.5 h, with the exception of 21 and 22 June 2017, where measurement took 8.8 and 9.7 h, respectively. Source of radiosonde data: Météo-France. Figure and description from Hagen et al., 2018.

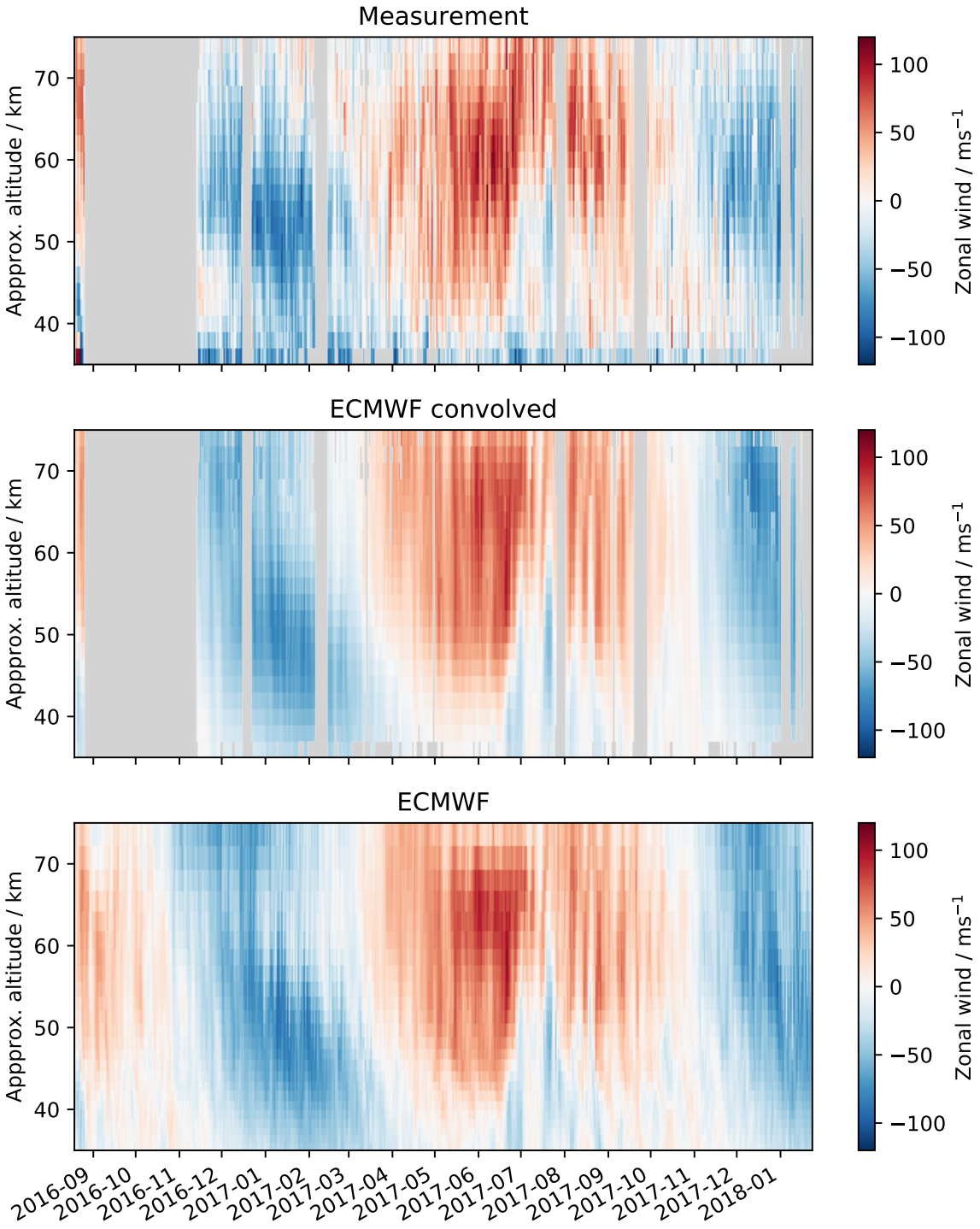

Figure 4.6 Zonal wind as measured by WIRA-C on Maido (top) with ECMWF operational analysis data, convolved with the averaging kernels (middle) and in its original form (bottom).

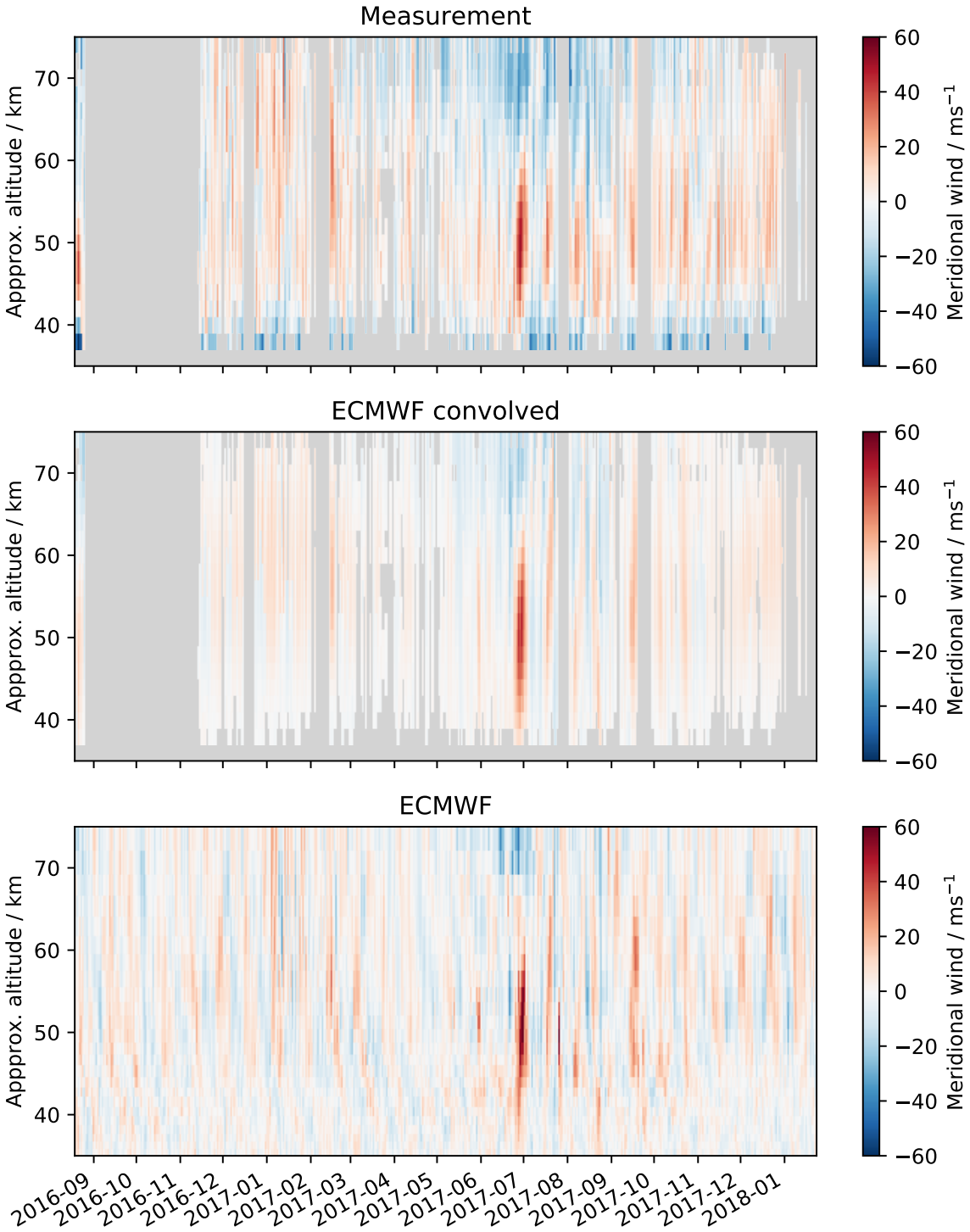

Figure 4.7 Meridional wind as measured by WIRA-C on Maido (top) with ECMWF operational analysis data, convolved with the averaging kernels (middle) and in its original form (bottom).

Figure 4.8 WIRA-C on the roof of the Arctic Lidar Observatory for Middle Atmosphere Research (ALOMAR) building on Andøya, Norway. On the left side, the hatch of the RMR lidar is visible.

4.2 WIRA-C: Andøya

In June 2018, WIRA-C was relocated to Andøya in Norway at 69 °N. The dates and coordinates for this campaign are given in table 4.2. The Arctic Lidar Observatory for Middle Atmosphere Research (ALOMAR) is a research station at the Andøya Space Center (ASC) with over a dozen different active and passive instruments to observe the Arctic atmosphere[2]. Most notably, ALOMAR hosts the RMR-Lidar (Baumgarten, 2010), a daylight capable lidar that measures temperature and wind up to approx. 80 km altitude under optimal conditions. Further, the VHF MAARSY radar and the rocket launch pad allow for distinguished multi-instrument campaigns for exploring the Arctic atmosphere (e.g. Strelnikov et al., 2017). The ALOMAR observatory is a multi-instrument reference station to the ARISE projects, with many different nations collaborating.

Located inside the polar circle, the ALOMAR observatory is an ideal place to observe the arctic middle-atmosphere. The goals of the WIRA-C campaign on Andøya can be summarized as follows:

- Acquire a time series of horizontal wind speeds in the arctic middle atmosphere
- Observe wind speeds in the context of sudden stratospheric warmings
- Compare WIRA-C measurements to the ALOMAR lidar
- Test WIRA-C performance (instrument / algorithms) in arctic maritime environment (rainfall, polar day and night)
- Provide a data set of horizontal wind speeds up to 75 km to complement continuous meteor radar observations in the mesosphere

The weather in Andøya is dominated by the marine climate and is variable only within days to weeks with long-lasting periods of light rainfall that peaks in September, right after the warmest months. Since passive radiometers can not measure during rainfall, we have periods with very few measurements and thus a low measurement response in the daily average. On the other hand, during periods of dry weather, the conditions for radiometric observations are nearly ideal. Polar day at Andenes lasts from 19. May to 24. July and polar night from 28. November 28 to 14. January.

Figure 4.11 and figure 4.15 show the whole WIRA-C time series measured at ALOMAR to date with a time resolution of 24 hours. Generally, it can be seen, that the measurement response during the summer months is lower than during the winter months due to many days with light rainfall. Due to the reduced measurement time during these periods and

[2] https://www.andoyaspace.no/alomar-observatory/

Location	ALOMAR Observatory, Andøya, Norway
Coordinates	69 °N, 16 °E
Altitude	370 m.a.s.l
Period	2018-06-11 (ongoing)
Duration	approx. 24 months

Table 4.2 Coordinates and dates of the Andøya Campaign of WIRA-C.

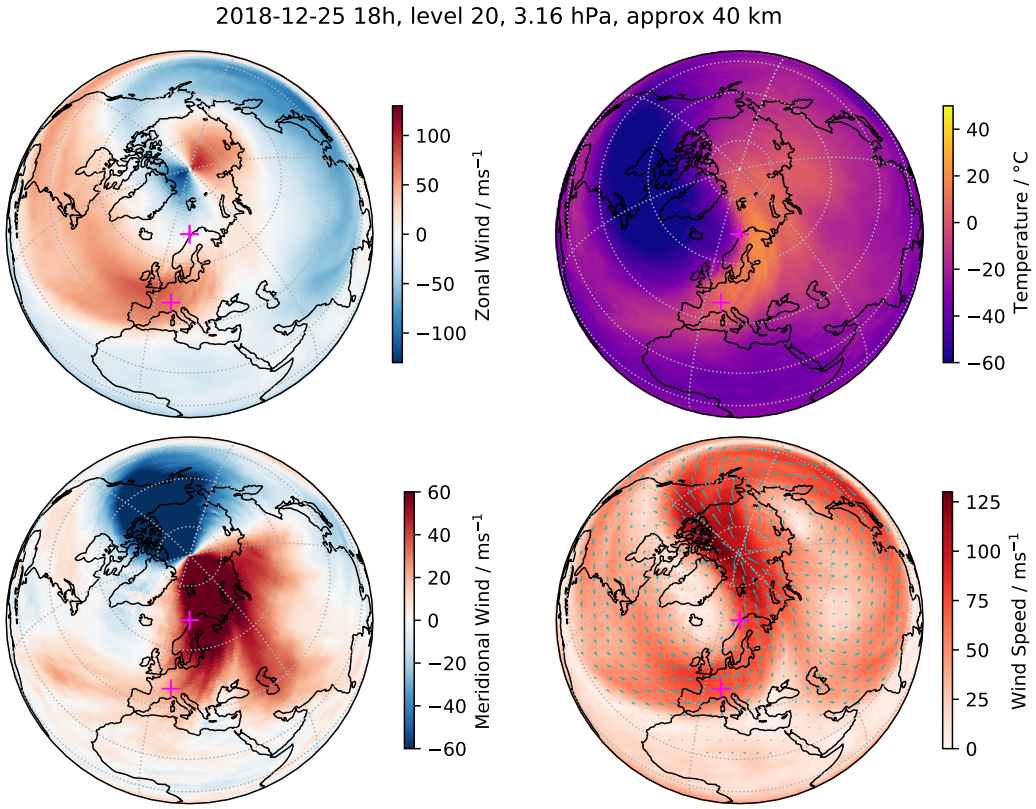

Figure 4.9 Zonal wind (top left), meridional wind (bottom left), temperature (top right) and wind speed and direction (bottom right) from ECMWF operational model output on 40 km altitude at 2018-12-25, right before the sudden stratospheric warming 2018/2019. The campaign locations Andøya and Bern are marked.

the reduced daily cycle during polar day and night, we use a time resolution of 24 hours for the overview plots.

This timeseries exposes many interesting features of the arctic middle atmosphere. Most prominently, the timeseries features the sudden stratospheric warming (SSW) in winter 2018/2019 with a short reversal of zonal wind followed by an eastward wind enhancement. The global context of this event is visualized in figure 4.9 and figure 4.10 using ECMWF operation model data before the SSW and at the central date (2019-01-06). In figure 4.9, it can be seen that the polar vortex shifts off from the pole, leading to high meridional wind speeds. These periods of enhanced meridional wind speeds are typical for the vortex splitting events. The corresponding pattern is clearly visible in the WIRA-C measurements of meridional wind speed in figure 4.12, which shows a clear disruption of the weak meridional background wind in the beginning of January 2019 with exceptionally strong meridional winds. The same pattern is also represented in the corresponding ECMWF data. A difference between the model and measurements appears in the zonal wind measurement during the SSW event. The zonal wind reversal on 40 km altitude persists longer in the WIRA-C measurements than in the ECMWF models. It would be interesting to further examine this feature, and check if similar differences are observable for other SSW events.

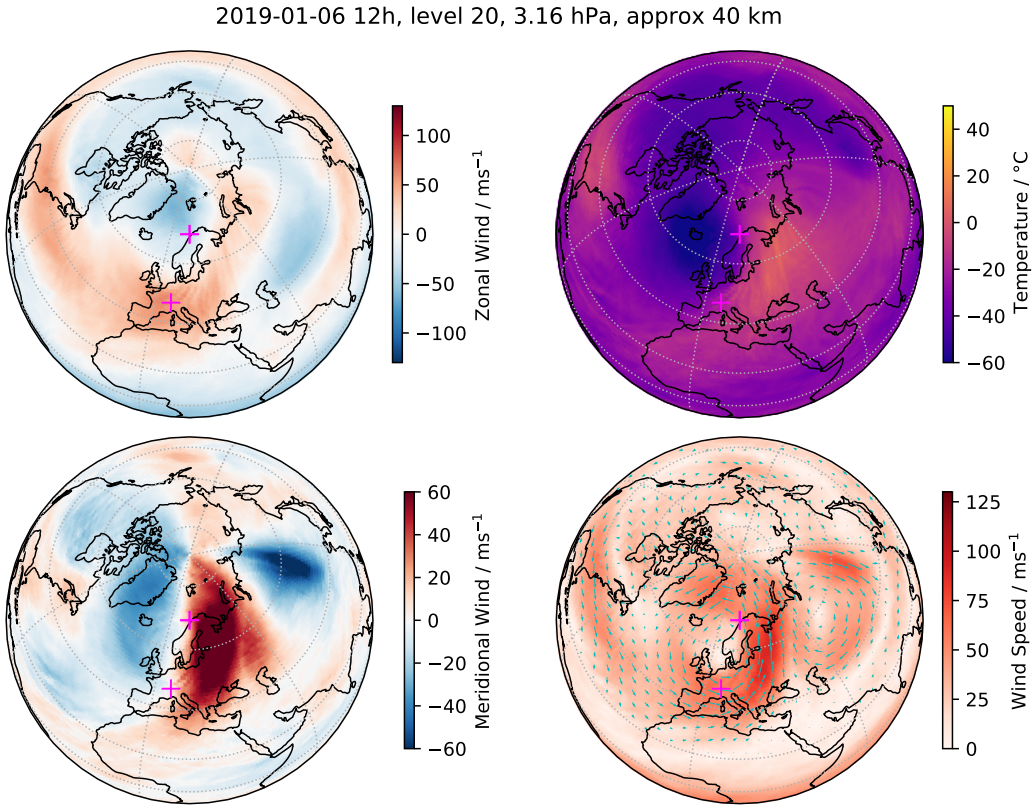

Figure 4.10 Zonal wind (top left), meridional wind (bottom left), temperature (top right) and wind speed and direction (bottom right) from ECMWF operational model output on 40 km altitude at 2019-01-06, at the central date of the sudden stratospheric warming 2018/2019. The campaign locations Andøya and Bern are marked.

The SSW 2018/2019 and its impact on the arctic middle atmosphere, as observed by the GROMOS-C microwave radiometer from Ny-Ålesund, is described in detail by Schranz et al., 2019b. Unfortunately, the WIRA-C elevation drive controller broke shortly after this event, prohibiting the observation of the atmosphere after the SSW until the controller has been replaced. A much less dramatic event of polar vortex offset is visible in winter 2019/2020 in the measurements of figure 4.12, where meridional winds enhance for a short period of time. A thorough comparison of measurements and models in the context of such events would certainly be an interesting topic for future studies.

Further, the stratospheric wind reversal in spring and autumn is well represented in measurements and models and happens on all observed altitudes simultaneously. Otherwise the observed wind background is rather stable over extended periods of time. The stable background allows the aggregation of measurements over longer periods, which has been exploited in the study about atmospheric tides (Hagen et al., 2020a).

In summary, the results from the WIRA-C campaign at the ALOMAR observatory can be summarized as follows:

- A continuous time series of horizontal wind speeds has been measured in arctic latitudes

- The signature of sudden stratospheric warmings in the wind field is well captured by our measurements
- Detailed comparisons of models and measurements in the context of such events is yet to be done, lidar measurements would be of high value for such comparisons
- The periods of stable eastward wind in the summer periods are beneficial for studying atmospheric tides in the middle atmospheric wind field

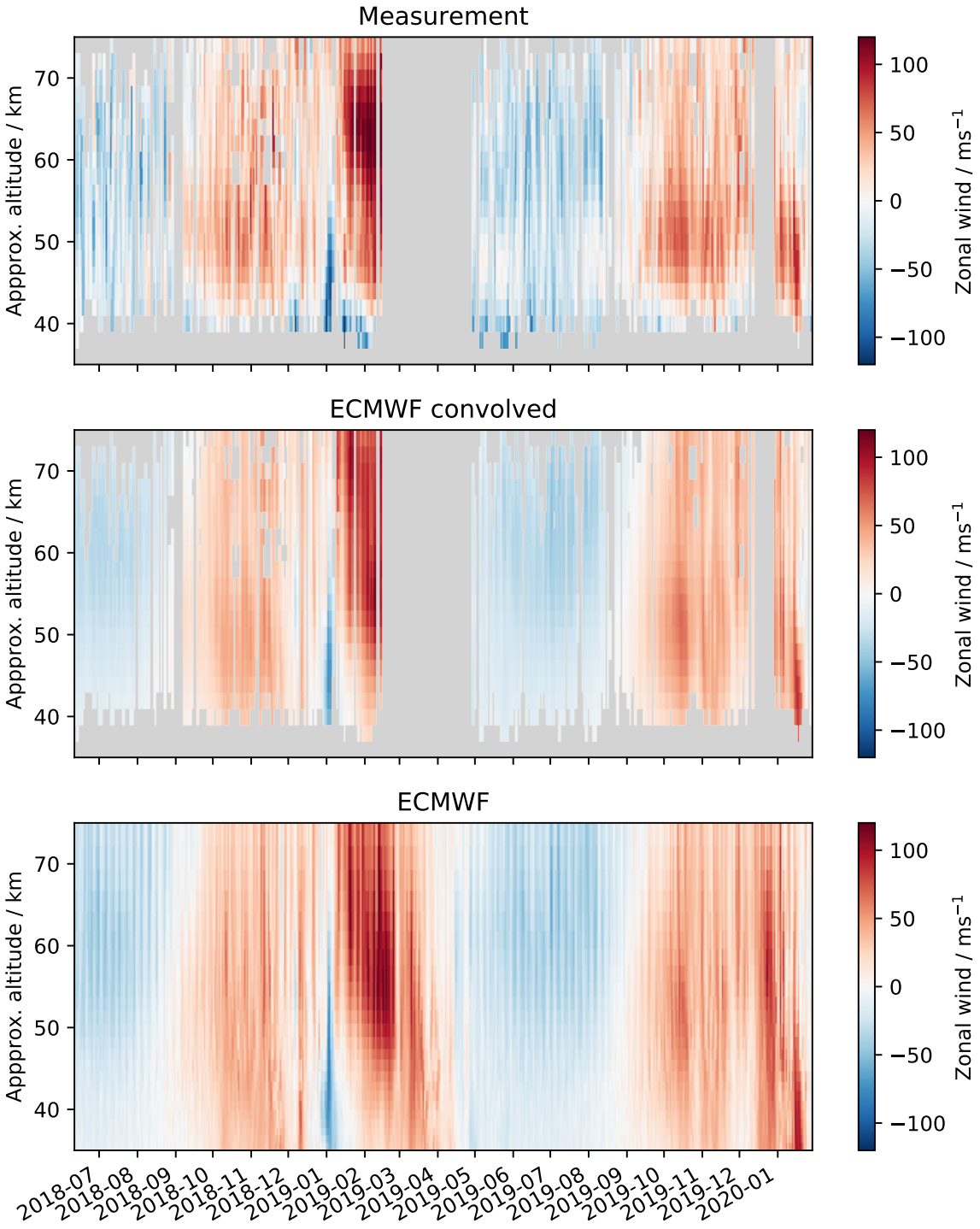

Figure 4.11 Zonal wind as measured by WIRA-C at ALOMAR (top) with ECMWF operational analysis data, convolved with the averaging kernels (middle) and in its original form (bottom).

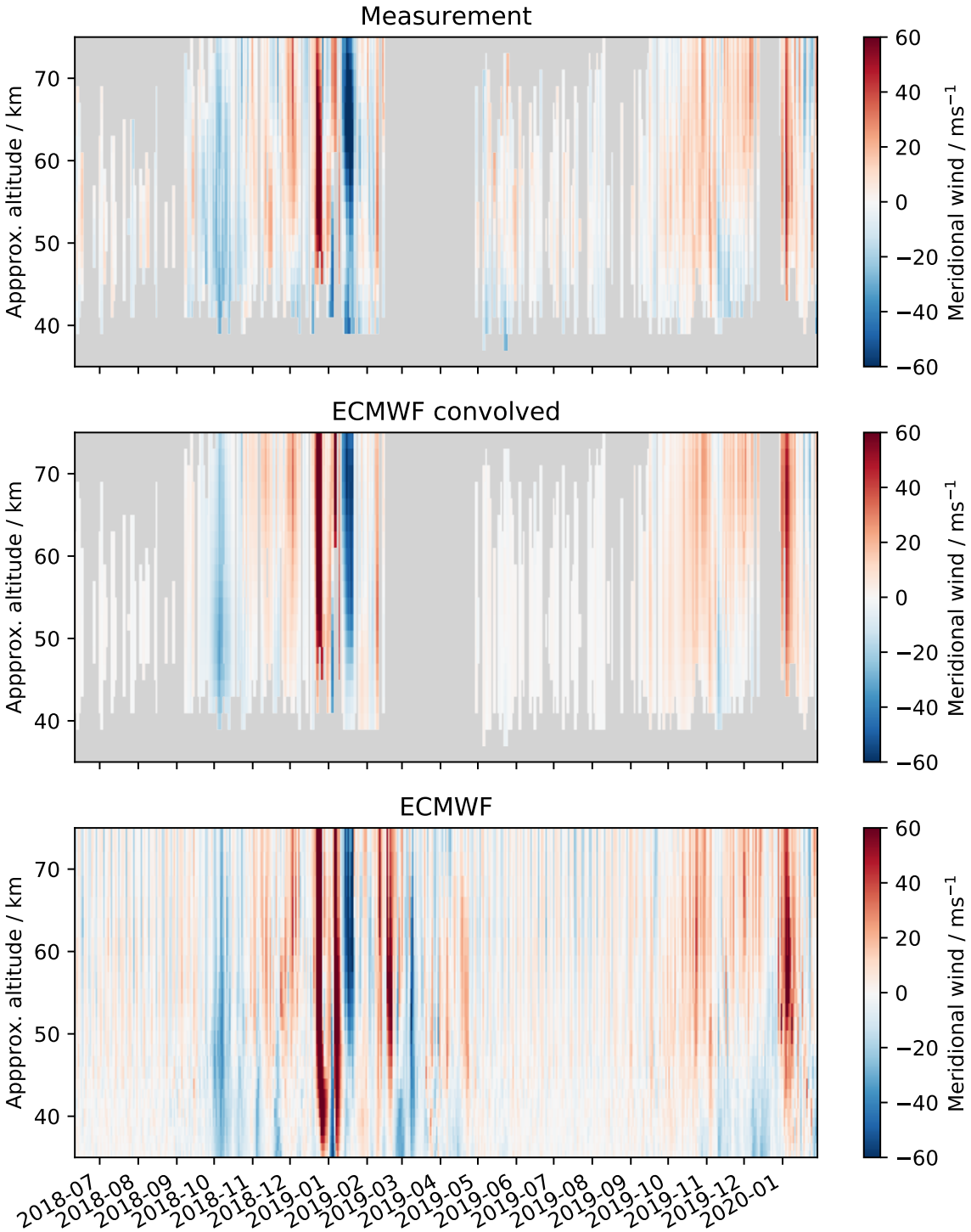

Figure 4.12 Meridional wind as measured by WIRA-C at ALOMAR (top) with ECMWF operational analysis data, convolved with the averaging kernels (middle) and in its original form (bottom).

Figure 4.13 WIRA on the roof of the building *Exakte Wissenschaften* at the University of Bern. The bird-spikes have been added after a crow ruined the measurement of a sudden stratospheric warming by destroying the protective cover of the feed horn.

4.3 WIRA: Bern

Since April 2018, WIRA is located in Bern, Switzerland on the roof of the building Exakte Wissenschaften of the University of Bern, shown in figure 4.13. The dates and coordinates of this campaign are shown in table 4.3.

Figure 4.14 and figure 4.15 show the measured timeseries during this campaign together with ECMWF operational analysis data with a 24 hour resolution. The time series shows a very strong annual cycle with eastward winds in summer and westwards wind in winter. The middle-atmospheric wind reversals in spring and autumn happens quickly and on all altitudes simultaneously. In winter, very strong eastward wind jets establish with wind speeds of 100 ms^{-1} stable over weeks and peaks up to 120 ms^{-1}. Meridional wind speeds are below 20 ms^{-1} during summer time.

As can be seen in figure 4.10 (previous section), the sudden stratospheric warming in winter 2019/2020 affected also the middle atmosphere in mid-latitudes. The reversals of meridional wind would have been observable in Bern (47 °N) by WIRA. Unfortunately a rather curious event foiled this observation. On December 24th 2018 (Christmas Eve), a crow destroyed the protective cover over the feed horn of WIRA, leaving the receiver chain unprotected against humidity and precipitation. This has not immediately been discovered, but since the feed horn is pointing upwards, the receiver chain filled with water during the next rainfall. Astonishingly the microwave components recovered after the first light rainfall and the failure was not discovered until the instrument failed permanently. All parts have been replaced and operation was back to normal in July 2019.

The data acquired from WIRA in Bern has not been used in the publications contained in this thesis, but has a big potential which is to be exploited in following studies. For example:

- Examine tides in the wind field in mid-latitudes
- Examine the phase relation of tides in the wind and temperature field together with the TEMPERA radiometer located in Payerne, Switzerland.
- Compare wind measurements to the (recently updated) lidar at the Haute-Provence Observatory (French Alps)
- Retrieve ozone data using the frequency-agile FFTS technique and compare ozone data to GROMOS (co-located)

Location	EXWI, University of Bern, Bern, Switzerland
Coordinates	47 °N, 7.4 °E
Altitude	575 m.a.s.l
Period	2018-04-11 (ongoing)
Duration	approx. 24 months

Table 4.3 Coordinates and dates of the Bern Campaign of WIRA.

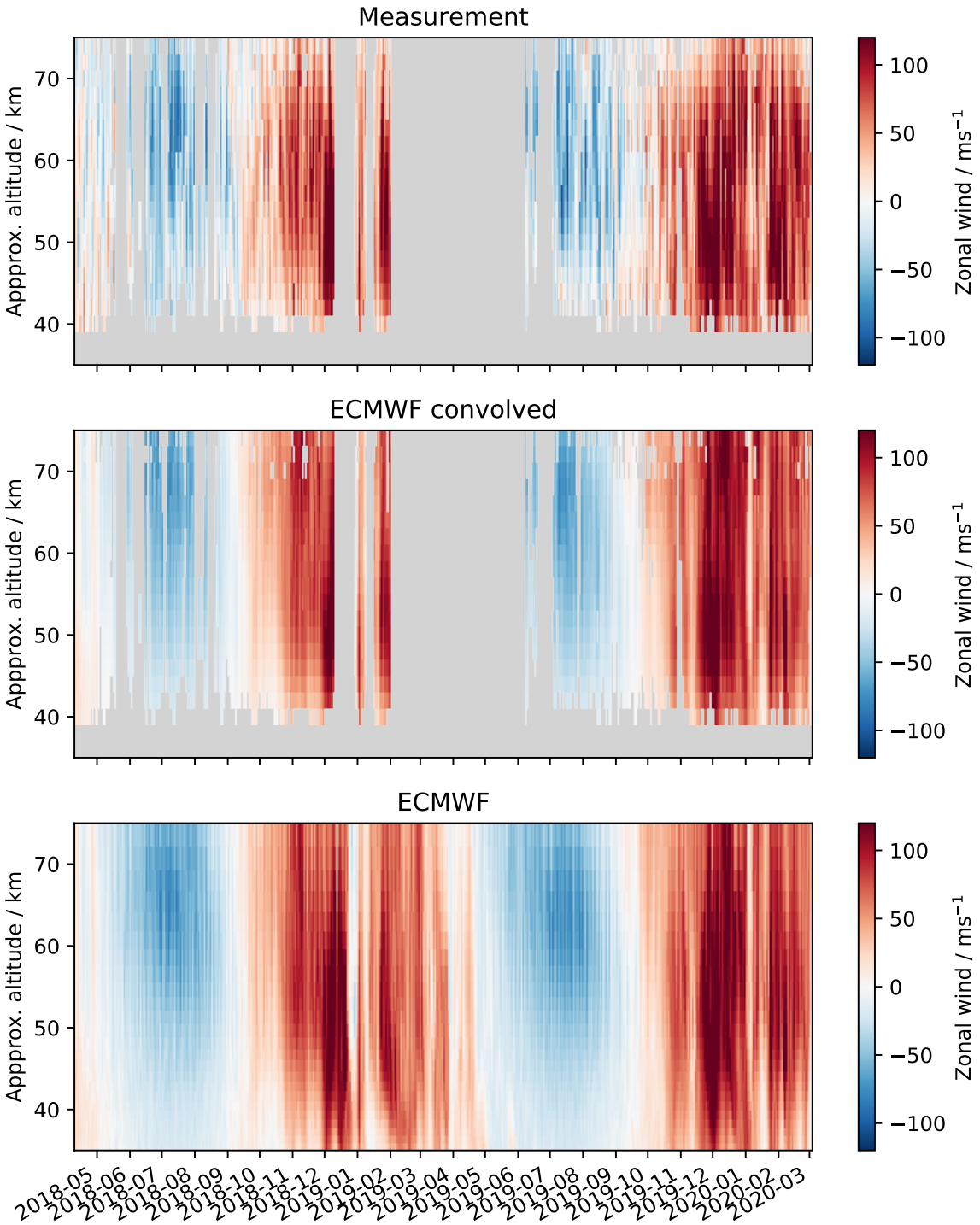

Figure 4.14 Zonal wind as measured by WIRA in Bern (top) with ECMWF operational analysis data, convolved with the averaging kernels (middle) and in its original form (bottom).

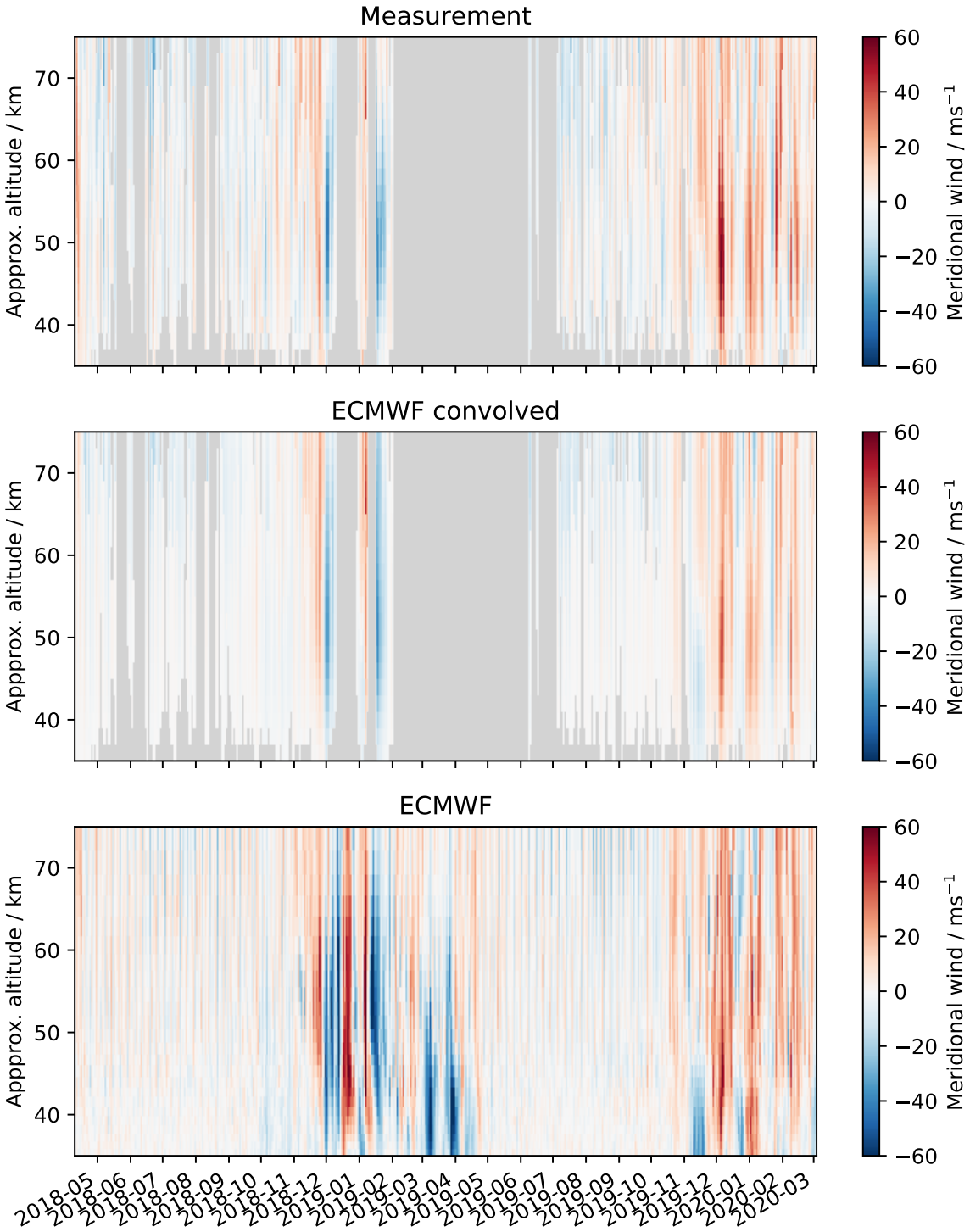

Figure 4.15 Meridional wind as measured by WIRA in Bern (top) with ECMWF operational analysis data, convolved with the averaging kernels (middle) and in its original form (bottom).

5 Publication: The WIRA-C instrument

Summary

This publication presents the WIRA-C instrument for the first time. While wind in the atmosphere can be measured using various techniques (see chapter 1), continuous measurements of altitude resolved wind profiles in the middle atmosphere (30 to 75 km) are very scarce. Passive microwave wind radiometry is capable to cover this gap and provides a method to retrieve robust and high quality continuous measurements of zonal and meridional wind speeds in this altitude region. While many publications are available on the WIRA instrument (e.g. Rüfenacht, Kämpfer, and Murk, 2012; Rüfenacht et al., 2014), this publication is fully dedicated to the technical details and first measurements of WIRA-C.

The manuscript contains a detailed description of many instrumental aspects, including the receiver system, calibration, wind retrieval algorithm and a detailed uncertainty budget. Further, we presented measurements of horizontal wind speeds between 30 and 75 km as acquired during the Maïdo campaign. Seven coincident lidar measurements form the Doppler wind lidar at the Maïdo observatory and ECMWF operational model output are used for comparison.

We show, that WIRA-C delivers profiles of zonal and meridional wind speeds for the altitude range of 35 to 75 km with a temporal resolution of 12 hours. The uncertainty budget shows that the random error sources (instrumental noise) are larger than the estimated systematic uncertainties and we put an uncertainty of 15 ms^{-1}(lowermost altitude) to 26 ms^{-1}(uppermost altitude) to our measurements of 12 hourly resolved wind profiles. The altitude resolution is as good as 10 km for the whole altitude range.

The comparisons with the lidar instrument and the ECMWF model data do not expose any systematic biases and agree within or close to their respective uncertainties.

Publication

The following article has been published in *Atmospheric Measurement Techniques (AMT)*.

Citation: Jonas Hagen, Axel Murk, Rolf Rüfenacht, Sergey Khaykin, Alain Hauchecorne, and Niklaus Kämpfer. "WIRA-C: A Compact 142-GHz-Radiometer for Continuous Middle-Atmospheric Wind Measurements". In: *Atmospheric Measurement Techniques* 11.9 (Sept. 4, 2018), pp. 5007–5024. ISSN: 1867-8548. DOI: 10.5194/amt-11-5007-2018

Atmos. Meas. Tech., 11, 5007–5024, 2018
https://doi.org/10.5194/amt-11-5007-2018

Atmospheric Measurement Techniques
Open Access
EGU

WIRA-C: a compact 142-GHz-radiometer for continuous middle-atmospheric wind measurements

Jonas Hagen[1], **Axel Murk**[1], **Rolf Rüfenacht**[1], **Sergey Khaykin**[2], **Alain Hauchecorne**[2], **and Niklaus Kämpfer**[1]

[1]Institute of Applied Physics, University of Bern, Bern, Switzerland
[2]LATMOS-IPSL, Univ. Versailles St.-Quentin, CNRS/INSU, Guyancourt, France

Correspondence: Jonas Hagen (jonas.hagen@iap.unibe.ch)

Received: 28 February 2018 – Discussion started: 4 April 2018
Revised: 12 July 2018 – Accepted: 31 July 2018 – Published: 4 September 2018

Abstract. Ground-based microwave wind radiometry provides a method to measure horizontal wind speeds at altitudes between 35 and 75 km as has been shown by various previous studies. No other method is capable of continuously delivering wind measurements in this altitude region. As opposed to lidar systems, microwave radiometers operate autonomously and independent of daylight and clouds.

In this paper, we present the WIRA-C (Wind Radiometer for Campaigns) instrument that observes the 142.17504 GHz rotational transition line of ozone with a high spectral resolution using a low noise single side band heterodyne receiver. Because the emitting molecules are drifting with the wind, the line is Doppler shifted. Together with the pressure broadening effect, this allows the retrieval of altitude resolved wind profiles.

The novel WIRA-C instrument represents the newest development in microwave wind radiometry and implements many improvements over its predecessor, the WIRA instrument. The main improvements include the compact structure, lower noise and an advanced retrieval setup. This paper describes the instrument and the data processing with a focus on the retrieval that takes into account a three-dimensional atmosphere and has never been used in ground-based radiometry before. The retrieval yields profiles of horizontal wind speeds with a 12 h time resolution and a vertical resolution of 10 km for zonal and 10 to 15 km for meridional wind speeds. We give an error estimate that accounts for the thermal noise on the measured spectra and additionally estimate systematic errors using Monte Carlo methods.

WIRA-C has been continuously measuring horizontal wind speeds for 1 year at the Maïdo observatory on Réunion (21.4° S, 55.9° E). We present the time series of this campaign and compare our measurements to model data from the European Centre for Medium-range Weather Forecasts (ECMWF) and coincident measurements of the co-located Rayleigh–Mie Doppler wind lidar. We find a good agreement between our measurements and the ECMWF operational analysis for the time series, where many features are present in both datasets. The wind profiles of the coincident WIRA-C and lidar observations are consistent and agree within their respective uncertainties for the lidar measurements with long integration times.

1 Introduction

Wind is a key parameter of dynamics throughout the atmosphere. In the troposphere, wind is directly related to weather phenomena. Dynamics in the stratosphere also have an influence on tropospheric dynamics and thus on weather phenomena (Baldwin et al., 2003; Charlton et al., 2004). Hence, many numerical weather prediction models have extended their upper limit to the mesosphere region in the past few years. At the same time, it is a fact that nearly no measurements of wind speeds in the upper stratosphere and the lower mesosphere exist. This region roughly corresponds to the so called radar gap, where too few scatterers for radar observations are present. The first wind radiometer WIRA proved Doppler microwave radiometry to be a suitable method to achieve wind profile observations between 35 and 75 km altitude on a campaign basis as well as for long term stationary measurements (Rüfenacht et al., 2012, 2014). In contrast, Rayleigh–Mie Doppler wind lidar techniques can also reach the upper stratosphere or even the mesosphere at 80 km

(Souprayen et al., 1999; Baumgarten, 2010; Yan et al., 2017). Lidar systems can provide wind profiles with a high temporal and spacial resolution; however, they always need clear sky conditions and measurements during daytime are difficult to achieve. In addition, they are not operating autonomously and are thus not very well suited for continuous wind measurements.

Rogers et al. (2016) observed the 11 GHz ozone line using low-cost satellite television electronics and derived seasonal and local solar time aggregated wind speeds at 95 km altitude using 5 years of measurements.

Spaceborne instruments like the Microwave Limb Sounder (MLS) measured wind speeds between 70 and 95 km (Wu et al., 2008) using the Doppler shift introduced to the 118 GHz emission line of oxygen and proposed to extend this range towards 40 km by using other emission lines. The Superconducting Submillimeter Wave Limb-Emission Sounder (SMILES) observed winds between October 2009 and April 2010 between 30 and 80 km by observing the Doppler shift of the 625 GHz ozone emission line and the HCl emission line at 625 GHz (Baron et al., 2013).

Ground-based passive microwave instruments are autonomous and independent of daylight or clouds and can thus deliver continuous measurements, even though with lower spacial and temporal resolution compared to lidar. Such measurements are important for the validation of models and other instruments, as demonstrated by Rüfenacht et al. (2018). In addition Le Pichon et al. (2015) showed that microwave wind radiometry is a valuable complement to other techniques like lidar and infrasound at multi instrument sites and contributes to the general understanding of middle atmospheric dynamics.

The WIRA-C instrument (Wind Radiometer for Campaigns) presented here, represents the newest development in microwave wind radiometry. It is capable to deliver 12 hourly resolved wind profiles in an altitude range of 35 to 75 km. Compared to the WIRA instrument (Rüfenacht et al., 2012), it is more compact, and thus easier to deploy and operate on campaigns. All optical elements, including the calibration target and the corrugated feed horn antenna, are integrated in a single housing with a stable temperature and stay dry and clean at all times, which allows us to resume high-quality observations immediately after rainfall. Furthermore, we apply a three-dimensional retrieval method (Christensen, 2015) that has never been used for ground based radiometry before.

After a short introduction of the measurement principle, we present the instrument, its optics and receiver system in Sect. 3. The data processing and the retrieval process used to obtain wind profiles from radiometric measurements is presented in Sect. 4. Also in Sect. 4, we present error estimations for random and systematic errors of our retrieval. Finally, the results from the 1-year campaign of WIRA-C on the Maïdo observatory on Réunion are shown in Sect. 5 and we compare our measurement data to the European Centre for Medium-range Weather Forecasts (ECMWF) operational model that is widely used in middle atmospheric research and to coincident lidar measurements.

2 Measurement principle

WIRA-C measures the spectral intensity of the 142.17504 GHz ozone rotational transition emission line. Wind information is introduced to the emission line by the classical Doppler shift, the linear relation between the line-of-sight speed of an emitter drifting with the wind flow v_{los} and the observed frequency shift $\Delta\nu$:

$$\Delta\nu = \frac{v_{\mathrm{los}}}{c}\nu_0. \tag{1}$$

Further, the emission line is pressure broadened, meaning that information about the altitude of the emitters is encoded in the spectrum. This allows the retrieval of wind profiles up to approximately 75 km, where the altitude-independent Doppler broadening effect starts to dominate.

Because the Doppler shift is proportional to the emitted frequency ν_0, it is advantageous to use a high observation frequency. We chose the 142 GHz emission line of ozone because of its strong magnitude and because the troposphere is more transparent in this frequency range than at higher frequencies. This limits the tropospheric contribution to the observed spectrum and increases the signal-to-noise ratio for middle atmospheric emission signals.

Passive microwave wind radiometers require a stable frequency reference as the ratio between observation frequency and the Doppler shift is in the order of 10^{-8} to 10^{-7} for typical atmospheric wind speeds of $10\,\mathrm{m\,s^{-1}}$ or $100\,\mathrm{m\,s^{-1}}$, respectively. Given our observation frequency of 142.17504 GHz, the Doppler shift introduced by line-of-sight wind speeds is 4.75 kHz per $10\,\mathrm{m\,s^{-1}}$. Further, we rely on opposing measurement directions, for example eastwards vs. westwards, to derive an absolute wind speed in the presence of possible frequency drifts and shifts not related to wind. This implies that we assume the horizontal wind speed to be constant over the horizontal distance spanned by the two opposing line-of-sights. For an elevation angle of 22°, this horizontal distance would be 150 km at 30 km altitude and 370 km at 70 km altitude.

3 The instrument

WIRA-C has been designed to be compact and autonomous. As depicted in Fig. 1, it fits into one single housing with the dimensions $0.6 \times 0.75 \times 0.5$ m and is set up on a tripod. It only needs an ethernet and a power connection and thus requires no additional laboratory space. Once set up, it measures autonomously and we supervise and configure the measurement process via remote connection. This makes WIRA-C an ideal instrument for campaigns at remote locations as well as for long term continuous observations.

[t]

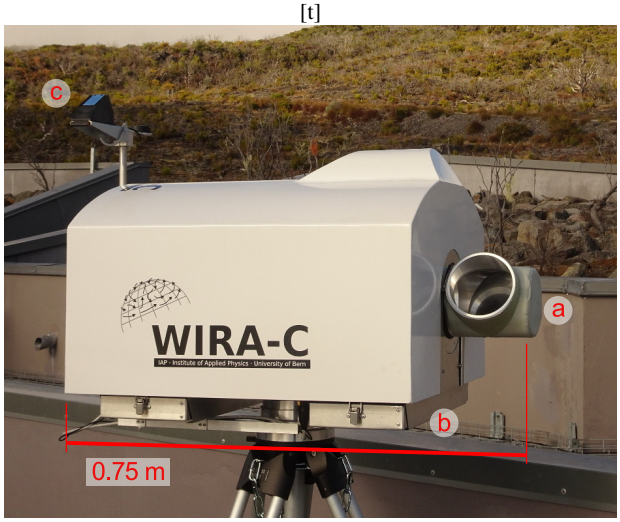

Figure 1. The WIRA-C instrument as installed on the Maïdo observatory on Réunion. It measures $0.6 \times 0.75 \times 0.5$ m and contains the optics, the receiver, a spectrometer, a computer and power supplies. Radiation from the sky enters the instrument through the scan drum **(a)**, which is at the same time the air outlet. The air filters **(b)** are placed below the instrument and the GNSS antenna and a rain sensor **(c)** are attached on top .

Besides the more compact structure, several technical improvements have been made over the WIRA prototype presented by Rüfenacht et al. (2012). Firstly, WIRA-C has a better signal-to-noise ratio than WIRA, thanks to the better low noise amplifier (LNA) in the receiver chain. Secondly, while WIRA observes at a fixed elevation angle of 22°, WIRA-C can freely select the elevation and azimuth angle to look at the sky thanks to independent elevation and azimuth drives. This makes WIRA-C a true all-sky microwave radiometer, similar to the concept of ASMUWARA (Martin et al., 2006), and we will benefit from this flexibility in the future, e.g. for the characterisation of tropospheric inhomogeneities in the context of tipping curve calibration. At the moment we use the all-sky mode only for the geometrical alignment by scanning the sun. For wind measurements we use the same well-established observation scheme as for WIRA because 22° elevation provide an optimum in terms of projection of horizontal wind speed to the line-of-sight vs. decreasing signal to noise ratio with increasing path length through the troposphere. Further, the ambient temperature calibration target is embedded inside the housing and thus better protected against environmental influence such as inhomogeneous heating by solar radiation. In particular, the optics and the calibration target are fully protected against rain. As no highly absorbing water can be deposited on the optical components, the instrument can resume the measurement immediately after rainfall has stopped. In addition many smaller technical improvements have been implemented, for example the path length modulator to mitigate standing waves between calibration target and receiver. The key specifications of WIRA-C are summarised in Table 1.

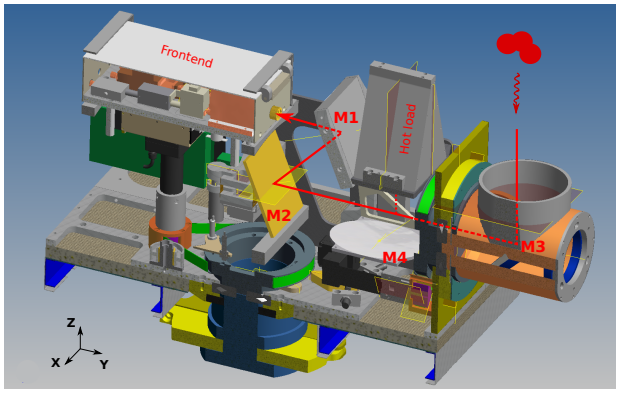

Figure 2. WIRA-C optics with flat mirror M3 (inside the scan-drum), flat mirror M2 (on a linear stage), elliptical mirror M1, elliptical mirror M4 (slewable, drawn in inactive state), hot load and the front end with the feed horn.

3.1 Receiver optics

Figure 2 shows the optical system with its four mirrors. Radiation from the sky enters the instrument through the scan drum that contains the flat mirror M3 and is rotatable to select any elevation angle. Together with the azimuthal drive at the bottom of the instrument, all cardinal directions (north, east, south, west) can be observed. This is important for robust wind retrievals, as the observation of opposite directions allows us to compensate for possible shifts in absolute frequency scale and also makes the calibration more robust as will be explained in Sect. 4.1.

From mirror M3, the radiation is deflected by the flat mirror M2 and coupled into the feed horn antenna by the elliptical mirror M1. The mirror M2 is mounted on a linear stage that can be shifted back and forth to make a $\lambda/4$ difference in optical path length between two measurements. This path length modulation is especially useful for calibration with the internal hot load as it mitigates standing waves between the receiver and the calibration target by destructive interference.

The calibration target is an aluminium wedge with a half angle of 12°, coated with absorbing material Eccosorb MMI-U. This absorber type from Laird NV is particularly well suited for those frequencies as shown by Fernandez et al. (2015b). Mirror M4 can be moved into the optical path to perform a hot load measurement and because of its elliptical shape focuses the beam to fit the load aperture, which results in a very compact calibration wedge. The calibration wedge is placed with its plane of incidence perpendicular to the electric field, which is generally referred to as transversal-magnetic (TM) mode. As measured with the setup described

Table 1. Key specifications of the WIRA-C microwave Wind Radiometer for Campaigns.

Optics	Ultra-Gaussian feed horn + elliptical and flat mirrors
Beam width	2.3° FWHM
Receiver type	Pre-amplified single-side band heterodyne
Frequency	142.17504 GHz
Bandwidth	2 × 120 MHz
Backend	Ettus Research USRP, FFTS
Spectral resolution	12.2 KHz
System Temperature	550 K
Calibration	Hot load + tipping curve
Elevation range	All sky

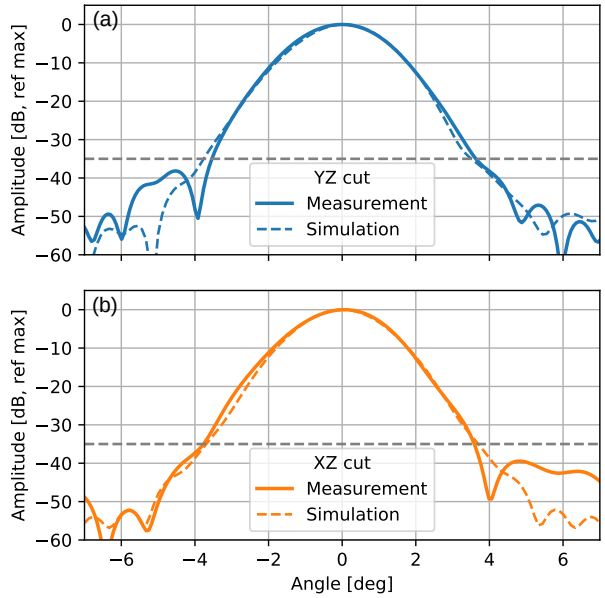

Figure 3. Measured and simulated far-field beam cuts of the whole instrument when pointing to zenith direction. Panel **(a)** shows the cut along the Y-Z-plane which is also the plane of reflection on the last mirror (see Fig. 2 for the coordinate system). Panel **(b)** shows the perpendicular cut. The gray dashed line marks the −35 dB level.

in Murk et al. (2006), the calibration wedge performs well with a reflectivity lower than −60 dB at 142 GHz.

A narrow beam with low side lobes is required for a well defined pointing. This is important for ground based radiometric measurements of the middle atmosphere, as the path length through the troposphere, and thus the tropospheric signal, increases rapidly with decreasing elevation angle, especially at low elevation angles used for wind measurements. The antenna of WIRA-C is an ultra low side lobe Gaussian corrugated feed horn with a divergence angle of $\Theta_{\text{feed}} = 14.3°$. The elliptical mirror M1 transforms this beam to the near-pencil instrument beam that has a full width at half maximum divergence angle of $\Theta_{\text{instr}} = 2.1°$.

We measured the beam pattern of the instrument using a vector network analyzer (VNA) in the near-field. The experimental setup for this measurement includes an open-ended waveguide probe placed in front of the instrument on a linear scanning stage that allows scanning along the x and y axis (see Fig. 2 for the coordinate system). The VNA source signal at 142 GHz is coupled into the optics by the WIRA-C feed horn. Figure 3 shows the far-field transformation of the scanning along the two axes as well as the corresponding physics simulations carried out with GRASP (TICRA, 2015). The measurements and simulations agree on a full width at half maximum of the beam of 2.1° and confirm the side lobes to be below −35 dB.

3.2 Receiver electronics

The receiver front end (Fig. 4) of WIRA-C contains a temperature-stabilised heterodyne single side-band receiver. The observed radio frequency (RF) of 142 GHz is collected by the feed horn and then amplified by the low noise amplifier (LNA) by 20 dB (3.29 dB noise figure at 142 GHz and 293 K). This LNA has been built by the Fraunhofer IAF based on the 50 nm M-HEMT technology described by Leuther et al. (2012). After subsequent selection of a single side band, the sub-harmonic mixer is fed by a local oscillator (LO) with 72.9 GHz, which gives an intermediate frequency (IF) of 3.65 GHz. The microwave components of the front end are all mounted on a rigid aluminium plate that is temperature stabilised by thermo-electrical elements to maintain a stable temperature at 295 K.

We use a Universal Software Radio Peripheral (USRP X310 with CBX-120 daughterboard, see Ettus Research, 2018) as Fast Fourier Transform Spectrometer (FFTS). It has a bandwidth of 200 MHz and a channel width of 12.2 kHz but due to some constraints by filters in the USRP, only the central 120 MHz of the full bandwidth can be used for our measurements. As shown in Fig. 4, the USRP provides two channels with independent local oscillators and AD converters. In the current setup, the primary channel (channel A) is centred around the resonance frequency of the ozone thermal emission line at 142 GHz while the secondary channel is offset by 120 MHz to extend the spectrum towards the off-resonance frequencies. The Fast Fourier Transformation (FFT) and accumulation algorithms are implemented using LabVIEW and programmed on the FPGA chip aboard the USRP.

The system noise temperature of the single-sideband receiver system is 510 K at 142 GHz, as measured in the laboratory by a hot–cold calibration using liquid nitrogen and confirmed by the routine tipping curve calibration. This is about 300 K lower than for the WIRA instrument, mainly due to the better quality of the 20 dB low noise amplifier.

As wind measurements require a stable frequency reference, we use a GPS disciplined and oven-controlled quartz oscillator to improve the long and short-term stability of the local oscillators of the front end and the back end.

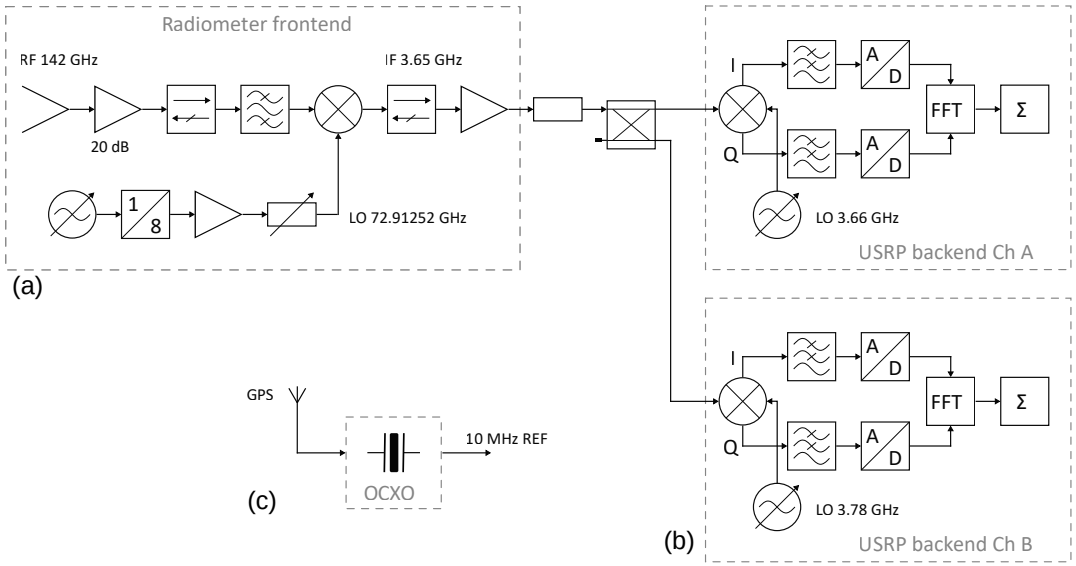

Figure 4. Block diagram of the WIRA-C single side-band receiver with radiometer front end **(a)** and USRP spectrometer **(b)** with channels A and B. The oven-controlled and GPS-disciplined crystal oscillator (OCXO) **(c)** provides the 10 MHz reference frequency for all local oscillators (LO) in the front and back end.

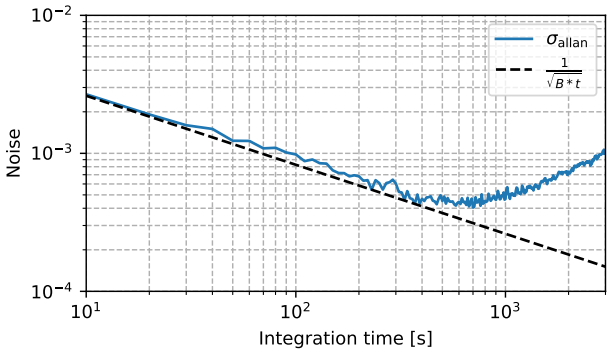

Figure 5. Allan variance of the receiver measured for a bandwidth of 14.6 kHz compared to the radiometric noise formula. The minimal Allan variance is reached after 4 min of integration.

The receiver gain typically drifts with time and periodical calibration is important to get consistent measurements. The Allan variance computation scheme (Ossenkopf, 2007) gives a timespan for which a receiver can be considered stable. Figure 5 shows the Allan variance for a 14 h measurement with the WIRA-C receiver. The noise of the WIRA-C receiver drops for an integration time up to 4 min for a single channel with a bandwidth of 14.6 kHz, then starts to increase again because of drifts. The duration of one measurement cycle was thus chosen to be 2 min.

4 Data processing

The primary measurement cycle of WIRA-C alternates between the six targets, which are the hot load, zenith (used as cold load), and the four 22° elevation observations (north, south, east, west). For all six targets the linear stage is placed in two different positions to make a difference in path length of $\lambda/4$. The integration time for each position of the linear stage is 10 s and the two measurements are averaged prior to calibration to cancel standing waves. Notably, we use the time during the relatively slow rotation around the azimuthal axis for the zenith and hot-load measurements to save valuable integration time. The twelve measurements of one cycle are then processed further, as described in the following sections.

4.1 Calibration

Compactness and low maintenance requirements were major design goals of WIRA-C, ruling out liquid nitrogen or a Peltier calibration target (Fernandez et al., 2015b) as cold reference that is needed in addition to the hot reference for radiometric calibration. This is why we opted for an ambient temperature hot load complemented with the tipping curve method for the radiometric calibration. Essentially, this method has been explained by Han and Westwater (2000) and uses the sky as cold load by assuming a mean tropospheric temperature and fitting the tropospheric opacity to a set of observations at different elevation angles. We use the measurements at 22° elevation and zenith, and estimate the mean tropospheric temperature T_m according to

Ingold et al. (1998) from the ambient temperature T_{amb} as $T_m^{22} = T_{amb} - 9.8\,K$ and $T_m^{90} = T_{amb} - 10\,K$, respectively.

The temperature of the hot load is measured by two temperature sensors mounted on its aluminium backing and follows the internal temperature of the instrument which we stabilise at about 10 K above the typical maximum ambient temperature by regulating air flow and additional heaters.

In order to include as little wind information in the tipping calibration process as possible, we average the northwards and southwards measurement to provide the input for the 22° elevation measurement to the tipping curve algorithm. We prefer that in favour of the eastwards and westwards measurements, as zonal winds are expected to be stronger and thus the slight broadening of the spectral line when averaging the two measurements would be increased.

4.2 Tropospheric correction

The calibrated brightness temperature as seen on the ground, $T_b(z_0)$, can be modelled as a sum of the tropospheric contribution driven by the same mean temperature T_m used above and a middle-atmospheric contribution $T_b(z_{trop})$ that would be observed if the instrument was above the troposphere (Ingold et al., 1998):

$$T_b(z_0) = T_m\,(1 - \exp(-\tau/\sin\eta)) + T_b\left(z_{trop}\right)\exp(-\tau/\sin\eta)\,, \quad (2)$$

where τ is the zenith opacity of the troposphere and η is the elevation angle of the observation. The opacity itself can be estimated in different ways. We are applying the same technique as Fernandez et al. (2015a) and use the brightness temperature at the wings of the measured spectra, as far away from the ozone rotational transition resonance frequency as possible. In practice we use an average over 10 MHz at the left wing of the spectrum measured by the second spectrometer channel (USRP channel B) depicted in Fig. 4. The Zenith opacity is then given by

$$\tau = -\sin(\eta)\,\ln\left(\frac{T_m - T_b^{\text{off-resonance}}}{T_m - T^{bg}}\right), \quad (3)$$

where we set the background temperature T^{bg} to 2.7 K. We apply this estimation for all four cardinal directions independently and thus account for direction-dependent tropospheric conditions.

As described in Sect. 3.2, the second channel of the USRP is offset by 120 MHz, giving us information up to 180 MHz off-resonance. At this offset from the line centre the ozone signal is still relatively strong and we see more than just the microwave background T^{bg}. However, for wind measurements we are more interested in a normalisation of the spectra of the four cardinal directions against each other to compensate for the tropospheric inhomogeneities than in absolute brightness temperature calibration.

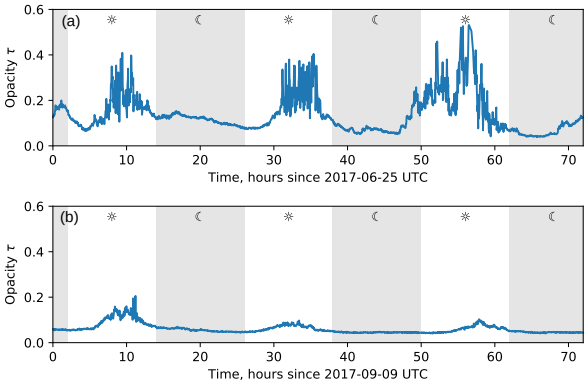

Figure 6. Opacity τ at the off-resonance observation frequency obtained from tipping calibration for three days in June **(a)** and September **(b)** at the Maïdo observatory. The gray areas mark nighttime, with sunrise and sunset at 02:00 and 14:00 UTC, respectively.

This gives us an estimate on τ for each observation direction and we can estimate the non-tropospheric contribution through

$$T_b\left(z_{trop}\right) = \frac{T_b(z_0) - T_m\,(1 - \exp(-\tau/\sin\eta))}{\exp(-\tau/\sin\eta)}. \quad (4)$$

As Eq. (4) is not linear in τ, it does not hold exactly for average values of τ and T_b for long integration times or highly variable tropospheric conditions. We encounter such conditions, for example, on the Maïdo observatory on Réunion (21.4° S, 55.9° E). There, during nighttime, the conditions are optimal for radiometric observations because the observatory is located at 2200 m above sea level and near the free troposphere during the night (Baray et al., 2013). However, during daytime, when microclimatic effects and convection are dominant, the opacity is highly variable as shown in Fig. 6. At the same time the signal-to-noise ratio for wind measurements is quite low and long integration times of several hours are required. The high variability of the opacity and the long integration times are the reasons why we apply the tropospheric correction directly to the calibrated spectra before integration and use the 12 h integration of the corrected brightness temperatures $T_b(z_{trop})$ for the wind retrievals. This integration time showed to be suited for the objective of instrument validation, but for other studies one might also consider shorter or longer integration times.

Figure 7 shows an example of a measured spectrum from one calibration cycle before and after tropospheric correction. Without tropospheric correction, the measurements in eastward and westward direction differ by 20 K because of tropospheric inhomogeneities. If we apply the tropospheric correction as described above using the left wing as reference, the spectra are on the same level and have the same magnitude. While we use the measurement form channel A

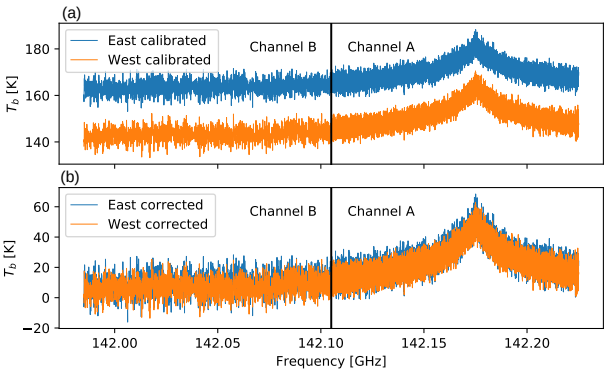

Figure 7. Measured spectrum of the ozone line from a single calibration cycle on 25 June 2017 at 09 h (UTC). Panel **(a)** shows the eastward and westward measurement after calibration, panel **(b)** shows the same measurement but with tropospheric correction applied. Channel A of the USRP has 12.2 kHz resolution and is centred around the line centre while channel B has 97.7 kHz resolution and observes the line wing.

for the retrieval of wind speeds, channel B is used solely for the tropospheric correction.

4.3 Retrieval of wind profiles

We retrieve wind information from the measured spectra by inverting a radiative transfer model that describes the relation between the atmospheric state vector $\boldsymbol{x}$ and the measurement vector $\boldsymbol{y}$ as $\boldsymbol{x} = F(\boldsymbol{y})$. The inversion thereof is typically ill-posed because many (unphysical) configurations of the atmosphere lead to the same measured brightness temperature. The optimal estimation method uses an a priori value with associated uncertainties for the atmospheric configuration to regularise the inverse problem as described by Rodgers (2000).

The WIRA-C retrieval of zonal wind uses the brightness temperature measured in eastern and western direction and combines these measurements to retrieve a single wind profile. The retrieval of the meridional wind is set up analogously. This is in contrast to the wind retrieval procedures used for WIRA, where wind profiles have been estimated for east and west separately and are then averaged to get a single zonal wind profile (Rüfenacht et al., 2014). By combining both observations in one inversion, we can effectively maximise the a posteriori likelihood of the wind profile given our two measurements in opposite directions. This is especially important in the presence of frequency shifts or drifts that are not related to wind. Such shifts are of a systematic or random nature and can originate from instrumental instabilities or offsets or even uncertainties in the molecular resonance frequency.

Fitting one atmosphere to two measurements drastically increases the overdetermination of the retrieval as the number of measurements is increased. This is explicitly wanted for wind and frequency shift where we need to combine all our measurements, but not ideal for ozone abundance that is also being retrieved to fit the observed line. Fitting one common ozone profile to the eastward and westward direction constrains the retrieval too much resulting in non-convergence or oscillations of the ozone profiles. This might be due to actual spatial variations in ozone abundances, which we consider to be unlikely as they are not expected to be that big in tropical latitudes. More probably, tropospheric inhomogeneities or clouds affecting the eastward and westward observations differently could have an influence on the ozone profile. However, this is not expected to have an influence on the retrieved wind speed, as the Jacobian of the forward model is completely antisymmetric with regard to wind as elaborated in Rüfenacht et al. (2014). This is why we model a three-dimensional atmosphere and include independent ozone profiles, and thus more freedom in our retrieval for the opposing observations.

In case of WIRA-C, the state vector $\boldsymbol{x}$ and the measurement vector $\boldsymbol{y}$ have the following form for the zonal wind retrieval (and analogous for the meridional wind retrieval):

$$\boldsymbol{x} = \begin{bmatrix} \boldsymbol{u} & \boldsymbol{x}_{\mathrm{O_3},\,1} & \dots & \boldsymbol{x}_{\mathrm{O_3},\,M} & \Delta f & \boldsymbol{b} \end{bmatrix}^{\mathsf{T}}, \tag{5}$$

$$\boldsymbol{y} = \begin{bmatrix} \boldsymbol{T}_{\mathrm{b,\,east}} & \boldsymbol{T}_{\mathrm{b,\,west}} \end{bmatrix}^{\mathsf{T}}, \tag{6}$$

where the elements of $\boldsymbol{x}$ are itself vectors. For example the zonal wind speed profile is given by $\boldsymbol{u} = \begin{bmatrix} u(p_1) & u(p_2) & \dots & u(p_N) \end{bmatrix}$ for N pressure levels. Besides the zonal wind profile $\boldsymbol{u}$, the $\boldsymbol{x}$ vector also contains the profiles of volume mixing ratio of ozone $\boldsymbol{x}_{\mathrm{O_3}}$ at M different spacial grid points as well as the frequency shift parameter Δf and one or more baseline parameters $\boldsymbol{b}$. Finally, the temperatures $\boldsymbol{T}_{\mathrm{b,\,east}}$ and $\boldsymbol{T}_{\mathrm{b,\,west}}$ are the calibrated and corrected brightness temperatures from Eq. (4).

The optimal estimation method then minimizes the cost function

$$\begin{aligned} \chi^2 = {} & \left(\hat{\boldsymbol{x}} - \boldsymbol{x}_{\mathrm{a}}\right)^{\mathsf{T}} \mathbf{S}_{\mathrm{a}}^{-1} \left(\hat{\boldsymbol{x}} - \boldsymbol{x}_{\mathrm{a}}\right) \\ & + \left(\boldsymbol{y} - F\left(\hat{\boldsymbol{x}}\right)\right)^{\mathsf{T}} \mathbf{S}_{\epsilon}^{-1} \left(\boldsymbol{y} - F\left(\hat{\boldsymbol{x}}\right)\right), \end{aligned} \tag{7}$$

for finding the most probable atmospheric state $\hat{\boldsymbol{x}}$ given the a priori profile $\boldsymbol{x}_{\mathrm{a}}$ and the measurement $\boldsymbol{y}$. It does so using the assigned statistics in form of the covariance matrices $\mathbf{S}_{\mathrm{a}}$ and $\mathbf{S}_{\epsilon}$ for the a priori data and the measurement, respectively.

They are constructed as block diagonal matrices, analogous to the $\boldsymbol{x}$ and $\boldsymbol{y}$ vectors in Eqs. (5) and (6):

$$\mathbf{S}_\mathrm{a} = \begin{bmatrix} \mathbf{S}_{\mathrm{a},\,u} & & & & & \\ & \mathbf{S}^{1,\,1}_{\mathrm{a},\,X_{\mathrm{O}_3}} & \cdots & \mathbf{S}^{1,\,M}_{\mathrm{a},X_{\mathrm{O}_3}} & & \\ & \vdots & \ddots & \vdots & & \\ & \mathbf{S}^{M,\,1}_{\mathrm{a},\,X_{\mathrm{O}_3}} & \cdots & \mathbf{S}^{M,\,M}_{\mathrm{a},X_{\mathrm{O}_3}} & & \\ & & & & \mathbf{S}_{\mathrm{a},\,\Delta f} & \\ & & & & & \mathbf{S}_{\mathrm{a,\,b}} \end{bmatrix}, \quad (8)$$

$$\mathbf{S}_\epsilon = \begin{bmatrix} \mathbf{S}_{T_{\mathrm{b,\,east}}} & \\ & \mathbf{S}_{T_{\mathrm{b,\,west}}} \end{bmatrix} = \sigma_y \mathbb{I}, \quad (9)$$

where the off-diagonal elements $\mathbf{S}^{i,\,j}_{\mathrm{a},\,X_{\mathrm{O}_3}}$ $(i \neq j)$ describe the covariance of the spatially distributed ozone profiles. Details about the setup of covariance matrices for multi-dimensional retrievals are described by Christensen (2015). The value σ_y on the diagonal of $\mathbf{S}_\epsilon$ is directly determined as the Allan-deviation of the measurement vector $\boldsymbol{y}$ by $\sigma_y^2 = \frac{1}{2}\langle(\boldsymbol{y}_{n+1} - \boldsymbol{y}_n)^2\rangle$.

Following Rodgers (2000) and using a linearised form of the forward model with Jacobian $\mathbf{K}$, the solution that minimizes Eq. (7) in a linear case is

$$\hat{\boldsymbol{x}} = \boldsymbol{x}_\mathrm{a} + \mathbf{G}\,(\boldsymbol{y} - \mathbf{K}\boldsymbol{x}_\mathrm{a})\,, \quad (10)$$

where $\mathbf{G}$ is the gain-matrix and describes the sensitivity of the retrieved profile to changes in the spectra:

$$\mathbf{G} = \frac{\partial \hat{\boldsymbol{x}}}{\partial \boldsymbol{y}} = \left(\mathbf{K}^T \mathbf{S}_\epsilon^{-1} \mathbf{K} + \mathbf{S}_\mathrm{a}^{-1}\right)^{-1} \mathbf{K}^T \mathbf{S}_\epsilon^{-1}. \quad (11)$$

As the frequency shift introduced by wind has a non-linear impact on the brightness temperature, the final solution $\hat{\boldsymbol{x}}$ is found by a Levenberg–Marquardt algorithm and Eq. (10) is applied iteratively while updating the point of linearisation for $\mathbf{K}$ but leaving $\boldsymbol{x}_\mathrm{a}$ fixed.

Assuming that $\mathbf{S}_\epsilon$ characterises the radiometric noise on the spectra, the uncertainty of the retrieved profiles due to thermal noise, the so called observational error σ_o, is defined as

$$\sigma_\mathrm{o}^2 = \mathrm{diag}\left(\mathbf{G}\mathbf{S}_\epsilon\mathbf{G}^T\right). \quad (12)$$

We assume that the major contribution to the uncertainty on the retrieved profiles is due to radiometric noise and thus use the observational error σ_o as a measure for the uncertainty in this study. It is important to note, that the observational error is influenced by the a priori statistics via Eq. (11) and the observational error grows with increasing a priori covariance because then the measurement and its noise have a bigger impact on the retrieved quantity. We accept this as an inherent property of the optimal estimation method: for a given thermal noise on the spectrum, the uncertainty of the retrieved value is smaller if there is less ambiguity in the a priori state.

Another measure for quality of our retrieved state $\hat{\boldsymbol{x}}$ is the averaging kernel matrix given by

$$\mathbf{A} = \frac{\partial \hat{\boldsymbol{x}}}{\partial \boldsymbol{x}} = \mathbf{G}\mathbf{K}. \quad (13)$$

Each row of the matrix $\mathbf{A}$ is called an averaging kernel and describes the smoothing of information. We use the averaging kernels for quality control as described in Sect. 4.5.

The forward model and OEM implementation is provided by ARTS/QPACK2 (version 2.3) (Eriksson et al., 2011). In the current setup for WIRA-C wind retrievals we use 6 ozone profiles equally spaced around the instrument location inside the east–west observation plane for zonal wind. We choose $M = 6$ as this showed to give superior retrieval results in terms of measurement response and altitude resolution than lower values. This is a detail related to the grid interpolations done by ARTS/QPACK2 and the construction of the covariance matrix for ozone. The covariance matrices for ozone are set up using separable statistics with a horizontal correlation length of 200 km, which we assume to be height independent.

4.4 A priori data and model parameters

For the a priori data for wind, we always use a $0\,\mathrm{m\,s^{-1}}$ profile. This equalises the probability to retrieve easterly and westerly winds, which is desirable in case of sudden wind reversals like they are observed around equinox and in context of sudden atmospheric events. To put it in other words, even though wind speeds in the atmosphere are generally not normally distributed we assume that the wind in the atmosphere is $(\mathbf{0} \pm \boldsymbol{s}_u)\,\mathrm{m\,s^{-1}}$ and we use climatological statistics from 6 years of ECMWF data at the campaign location to estimate $\boldsymbol{s}_u$ which then depends on altitude but not on time. The same applies for meridional wind, and $\boldsymbol{s}_v$ turns out to be smaller than $\boldsymbol{s}_u$ because meridional winds are typically slower than zonal winds. We multiply these statistics by a factor of 2 in order not to have a bias towards zero, as elaborated by Rüfenacht et al. (2014) and additionally we impose a vertical correlation length of 0.5 pressure decades to construct the covariance matrix. Like this, our retrieved wind speeds are regularised but in no case biased towards either direction by the a priori wind profile.

For the ozone a priori data, we rely on a F 2000 WACCM scenario from a simulation by Schanz et al. (2014). This allows us to extend the retrieval grid up to 110 km altitude and thus includes the nighttime secondary ozone maximum at 10^{-3} Pa. We determine the a priori profile and variance in a window of 11 days around the day-of-year of our measurement while only regarding the same hours of the day that we integrated over (either day or nighttime). Extending the retrieval grid and separating day and nighttime retrievals is important because signals from the secondary ozone maximum can have an influence on wind retrievals below 75 km if not properly handled as elaborated by Rüfenacht and Kämpfer (2017).

We multiply the variance of ozone by a factor of 4 for the same reasons as above and impose a vertical correlation length of 0.3 pressure decades to get the covariance matrix. As explained in Sect. 4.3, the horizontal covariance of ozone is assumed to be height independent with a horizontal correlation length of 200 km. The ozone a priori profile and covariance matrix thus depend on altitude and time (day or night and time of year).

The forward model also needs additional information about the atmosphere, namely it includes the temperature profile (from MLS and ECMWF complemented with WACCM) and volume mixing ratio profiles for the less critical species N_2 and O_2 (from standard atmospheres) that are known well enough and thus will not need to be optimised.

4.5 Quality control and uncertainty

A big advantage of the optimal estimation method over other regularisation methods is the availability of error estimations and quality control information.

As expressed by Eq. (13), the averaging kernel matrix (AVKM) describes the sensitivity of our estimated atmospheric state $\hat{\boldsymbol{x}}$ for the true state $\boldsymbol{x}$. We derive three quantities from the averaging kernel matrix: firstly, the measurement response that is the sum of the rows of the AVKM and describes the sensitivity of our retrieved state to the true state as can readily be seen in Eq. (13). Ideally it is exactly 1, meaning that a change in the true atmospheric state is exactly represented in the retrieved state. Secondly, the full width at half maximum of the averaging kernels gives information about the spatial smoothing of the data. Ideally these kernels would be delta peaks (which would make the AVKM diagonal). Finally, we examine the difference between the peak of the averaging kernels to their respective nominal height. In the ideal case (diagonal AVKM), the offset would be zero, meaning that all information is mapped to the correct grid points. We use the information in the AVKM for quality control of the wind retrieval: the measurement response must be between 0.8 and 1.2 and the offset of the peak to the nominal height of the kernel must not exceed 5 km. If these criteria are fulfilled for an extended altitude range, the retrieved values are valid. Further, the full width at half maximum (FWHM) of the individual kernels gives information about the altitude resolution.

Figure 8 shows the averaging kernels and the derived quality control parameters for one measurement. The retrieved values are considered to be valid between 38 and 75 km altitude. The measurement response would be acceptable on higher altitudes but the upper points are rejected by the offset parameter. We see the offset parameter jumping from −7 to 10 km at approximately 80 km altitude. This is because Doppler broadening starts to dominate the pressure broadening above approximately 75 km altitude and signals can not be attributed to the exact height they originate from. This means that they are attributed to lower or higher altitudes

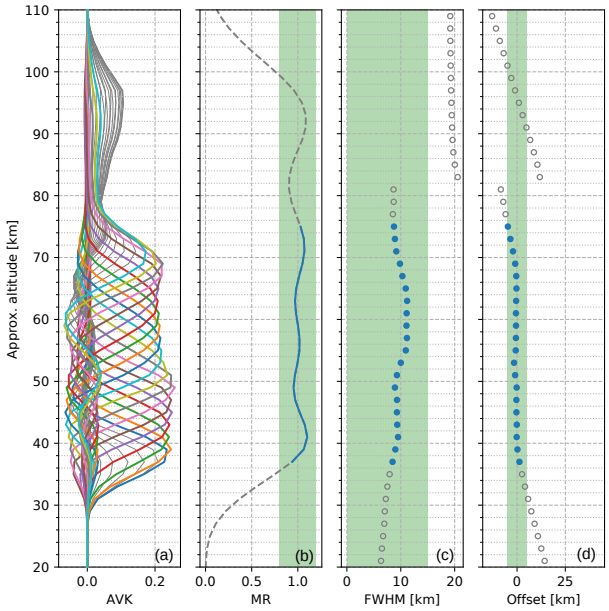

Figure 8. Visualisation of the averaging kernel matrix (AVKM) for the nighttime measurement of 26 June 2017. The individual averaging kernels (rows of the AVKM) for each altitude **(a)** are characterized by the measurement response (MR), their full width at half maximum (FWHM) and the difference of their maximum to the nominal height (Offset). The valid ranges for all parameters are marked by the green areas. Valid components that fulfill all criteria are shown in colours and others in gray (or dashed lines and hollow markers, respectively).

depending on the ozone a priori profile. Even though the measurement response stays within the bounds of validity in these altitudes, offset criteria reject these points reliably.

The FWHM in Fig. 8 indicates an altitude resolution between 9 and 11 km for the whole altitude range. This is an improvement in comparison to the WIRA retrieval, where the altitude resolution for zonal wind is about 10 to 16 km (Rüfenacht et al., 2014). We attribute this improvement to the lower noise of the instrument and the simultaneous inversion of the two measurements, which gives more independent information than the inversion of one spectrum after the other.

Further, Fig. 9 shows the residuals for the same retrieval shown in Fig. 8. The residuals look random, indicating that we properly model our observations.

Figure 10 shows the observation error σ_o for four different measurements together with the FWHM and the measurement response. We see that the observation error for zonal wind retrievals is approximately $15\,\mathrm{m\,s^{-1}}$, up to 64 km altitude for the nighttime measurement with the chosen integration time of 12 h. Below 55 km, the errors of the day and nighttime measurement are nearly identical, but above 60 km the error for the day time measurements increase rapidly. As tropospheric opacity has a big impact on the signal-to-noise

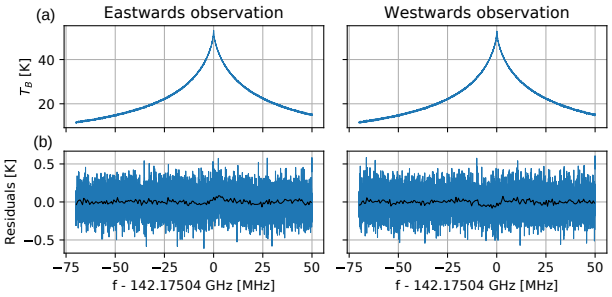

Figure 9. Corrected and integrated (12 h) brightness temperature spectra as used for the retrieval of 26 June 2017 nighttime for eastwards and westwards direction **(a)** together with the residuals (observed minus computed, **b**). Smoothed residuals (by binning 50 channels) are shown in black.

ratio of the spectra, the bigger uncertainty for the daytime measurements can be explained by the higher opacity during daytime as is shown in Fig. 6. Also the ozone concentration is lower during daytime as studied for example by Studer et al. (2014), resulting in less emitters and lower signal-to-noise ratio during daytime compared to nighttime. The observation error is smaller for the meridional wind than it is for the zonal wind. As elaborated in Sect. 4.3, this is because the observation error is not independent of the a priori statistics and the covariance for meridional wind is smaller than for zonal wind.

The full width at half maximum, that is also shown in Fig. 10, describes the altitude resolution. For zonal wind, the altitude resolution is approximately 10 km up to 68 km. For meridional wind, the resolution is between 10 and 15 km, which is a direct consequence of the more restrictive a priori profile for meridional wind. While the measurement response is even between 0.9 and 1.1 (as opposed to the quality requirement of 0.8 to 1.2) for nearly the entire altitude domain for zonal wind indicating that our retrieval is highly sensitive to changes in the atmospheric wind speed and largely independent of the a priori profile. The measurement response for the meridional wind is somewhat more variable, which is related to the constriction by the a priori profile, because a smaller a priori covariance also implies less weight on the measurement and thus lower sensitivity. Nevertheless, the quality requirement is fulfilled between 38 and 65 km.

4.6 Estimation of systematic errors

In the above section, we discussed the random errors caused by thermal noise on the spectrum as determined by the optimal estimation method. Additionally we perform a Monte Carlo error estimation to further characterise uncertainties not related to noise. These uncertainties are of systematic nature, as they are inherent to the retrieval setup and choice of a priori profiles and covariance matrices. Table 2 gives a list of the variables we considered in this analysis together

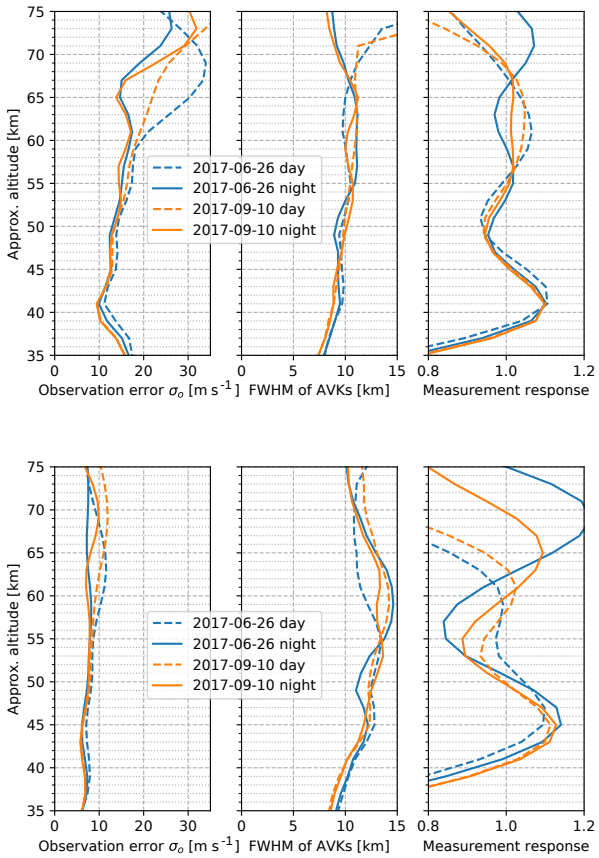

Figure 10. Characterisation of the retrieval quality for zonal and meridional wind for the day and nighttime period of 2 days. The observation error represents the measurement uncertainty. The full width at half maximum (FWHM) of the averaging kernels describes the altitude resolution, which is approximately 10 km, up to 68 km altitude. The measurement response is a measure for the sensitivity of our retrieved wind speeds to changes in actual wind speeds. In the perfect case it would be 1.0 but values between 0.8 and 1.2 are acceptable.

with their expected distribution. The Monte Carlo estimation involves sampling from these distributions and retrieving a wind profile for every sample. The estimated systematic error is then derived from the standard deviation of the retrieved wind speeds.

All the profiles (temperature, a priori and covariances) are expected to follow a Gaussian distribution as they are derived from statistics as described in Sect. 4.4. We perturb the profiles on all altitudes simultaneously using the value sampled from the respective distribution. The elevation is expected to have a systematic error of maximum $\pm 0.2°$, as this is the estimated precision we reach when levelling the instrument. The calibration subject in Table 2 accounts for the uncertainty in the calibration and tropospheric correction. This uncertainty has a random and a systematic component. We only

Table 2. Considered uncertainties for the Monte Carlo error analysis together with the estimated error. The resulting error is given as the maximum error in three altitude domains: lower, from 5 to 1 hPa (36 to 48 km), middle, from 1 to 0.2 hPa (48 to 59 km) and upper, from 0.2 to 0.02 hPa (59 to 75 km).

				Estimated 1σ error, $\mathrm{m\,s^{-1}}$		
Subject	Distribution	Type	Parameters	Lower	Middle	Upper
Temperature profile	Gaussian	absolute	$2\sigma = 10\,\mathrm{K}$	0.86	0.94	0.57
Ozone a priori profile	Gaussian	absolute	$2\sigma = 0.4\,\mathrm{ppm}$	0.91	1.2	3.2
Ozone covariance	Gaussian	relative	$2\sigma = 50\,\%$	2.4	4.6	10
Wind covariance	Gaussian	relative	$2\sigma = 50\,\%$	2.5	3.0	4.3
Elevation	uniform	absolute	$\pm 0.2°$	3.4	1.5	2.0
Calibration	uniform	relative	[1, 1.3]	2.4	3.0	6.5
Total systematic				5.6	6.6	13
Retrieval noise				15	17	26

$2\sigma = 50\,\%$ means $\sigma = \frac{1}{4}\mu$ for a Gaussian distribution with mean μ.

consider the systematic part that comes from the fact that our off-resonance frequencies used to determine the tropospheric opacity is still somewhat closer to the line centre than would be desirable (see Sect. 4.2). In our Monte Carlo estimation we simulate this error by introducing a factor in the range [1, 1.3] to the $\boldsymbol{y}$ prior to the retrieval, which corresponds to an assumed uncertainty of 10 % of the tropospheric opacity. Further, we neglect all correlations between systematic errors and among systematic and random errors.

We performed the Monte Carlo estimation for four different cases (same as shown in Fig. 10). The results for the setup of one retrieval (26 June 2017, nighttime) is shown in Table 2 for three different altitude domains. The biggest systematic error is evident in higher altitude domains and comes from the ozone a priori profile. The influence of the ozone a priori profile has been thoroughly examined by Rüfenacht and Kämpfer (2017), concluding that a careful choice of ozone a priori and covariance data is important for the retrieval of wind speeds in higher altitudes. The total systematic error is approximately half the retrieval error in the worst case and by just looking at the retrieval noise, we thus underestimate the total error by approximately 10 %.

5 Validation

5.1 The Maïdo campaign

From August 2016 until February 2018, the WIRA-C instrument has been operated at the Maïdo observatory on Réunion(21.4° S, 55.9° E) at 2200 m above sea level. After having been operational for a few days in August 2016, a very uncommon failure of the synthesiser–multiplier chain occurred and the campaign could continue only in mid-November. Since then, WIRA-C measured continuously, except for a period of tropical cyclone alert and some power outages. The few measurements in August 2016 are very valuable because they coincide with three lidar measurements.

For all retrievals presented in this section, we used an integration time of 12 h, from 02:00 to 14:00 UT which is 06:00 and 18:00 local time (LT) and roughly corresponds the times of sunrise and sunset in the tropics. We set up the a priori profiles and covariances as described in Sect. 4.4 and most notably use an a priori of $0\,\mathrm{m\,s^{-1}}$ for all pressure levels for zonal and meridional wind. Quality control for the retrieved data is done as described in Sect. 4.5.

5.2 Comparison data

5.2.1 ECMWF model data

The ECMWF operational analysis provides atmospheric data on 137 layers up to 80 km altitude. However, the main focus lies on delivering data on the atmospheric layers below 35 km for weather forecasts. Especially above 68 km the data quality is supposed to decrease because the uppermost layers do not assimilate measurements but are artificially forced to model stability.

The ECMWF operational analysis has a higher time and altitude grid resolution than the WIRA-C retrieval. The time resolution is 6 h, whereas WIRA-C has a time resolution of 12 h. Thus, to check the two datasets for consistency we always average the two ECMWF time steps which are within the respective integration period of WIRA-C.

To adapt the vertical resolution of the model to our retrieval, we convolve the model data with the averaging kernels of the retrieval.

Integrated forecast system cycles Cy41r2, Cy43r1 and Cy43r3 have been used for this study.

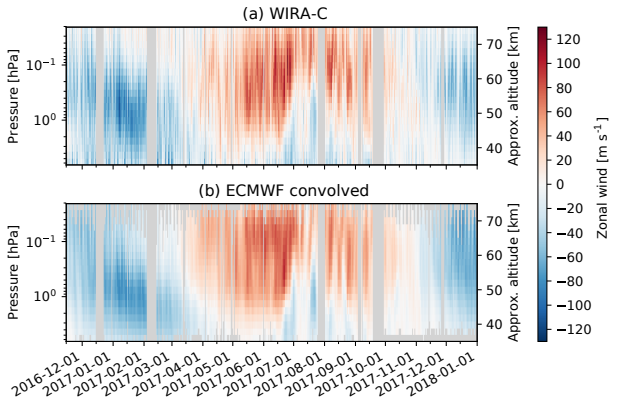

Figure 11. Time series of zonal wind speeds measured by WIRA-C **(a)** and ECMWF analysis data **(b)** between 14 November 2016 and 31 December 2018 for the altitude range of 35 to 75 km with a time resolution of 12 h (day and nighttime). The ECMWF data has been convolved with the averaging kernels of the retrieval in order to get the same spatial and temporal resolution for both datasets. Invalid data points are grayed out, resulting in different altitude ranges for different days. The few data gaps are due to a tropical cyclone and power outages.

5.2.2 The Rayleigh–Mie Doppler wind lidar

The Rayleigh–Mie Doppler wind lidar is an active sounder, measuring the Doppler shift of backscattered visible light using Fabry–Perot interferometry and can provide wind profiles from 5 up to approximately 60 km. Up to 30 km, the vertical resolution is 100 m and the accuracy is better than 1 m s^{-1} for 1 h integration time. Because of decreasing density of molecular backscatters and the inverse-square law of light, the uncertainties of the lidar measurements increase with altitude and finally limit the altitude domain to approximately 60 km depending on integration time. Between 30 and 60 km, the vertical resolution varies between 0.5 to 3 km and the measurement error is 10 m s^{-1} at 50 km altitude for an integration time of 3 h. The instrument and the retrieval scheme is described in Khaykin et al. (2016) and references therein.

The lidar only measures at nighttime and has a variable integration time that depends on meteorological conditions (clear sky) and available man power. As the integration time often is below 4 h, we cannot run a retrieval for the microwave radiometer for exactly the same integration time because of the noise. We currently have no opportunity to adapt our measurement to the short integration times of the lidar and thus we just compare the nighttime measurement of WIRA-C and the lidar while noting the respective integration times. For the vertical resolution we convolve the lidar data with the averaging kernels of the retrieval to have comparable altitude resolution of the profiles.

The lidar measures at an elevation angle of 45° as opposed to the 22° of WIRA-C. However, the difference between

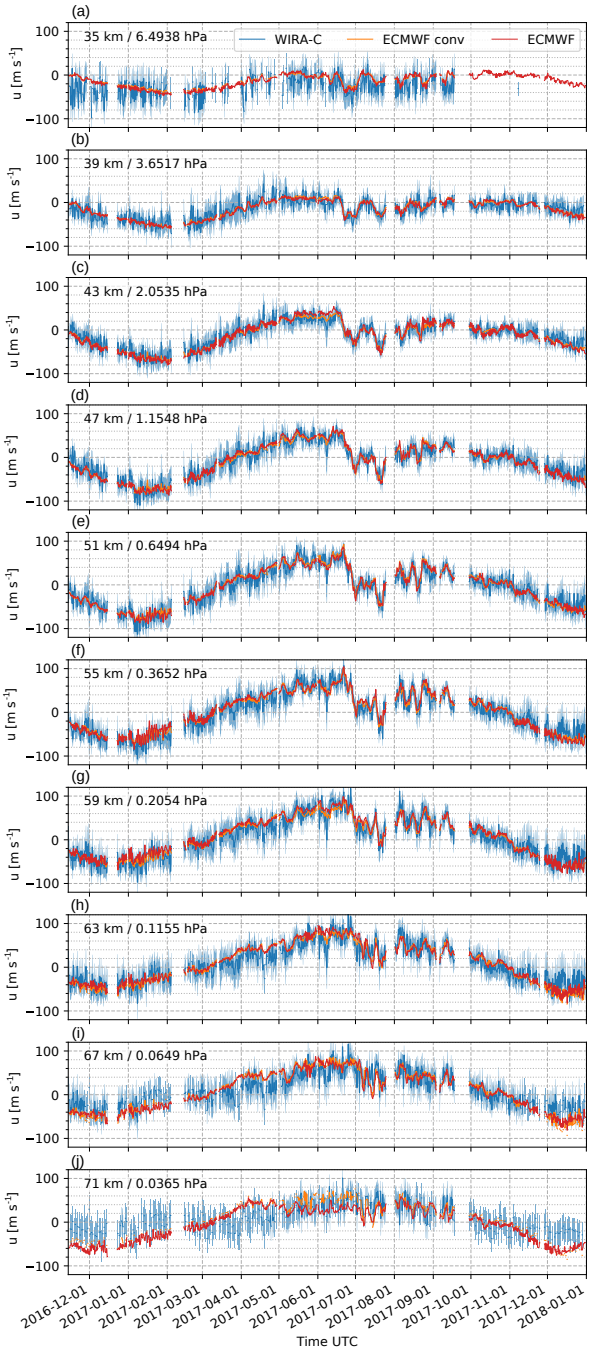

Figure 12. Zonal WIRA-C wind measurements on 10 distinct pressure levels between 35 km **(a)** to 71 km **(j)**. The fully convolved ECMWF model data as well as the ECMWF data from the nearest pressure level (but still smoothed in time) is given for comparison. Often the raw and convolved ECMWF curves coincide. Time resolution is 12 h (day and nighttime). The light-blue area represents the uncertainty σ_o of the WIRA-C data.

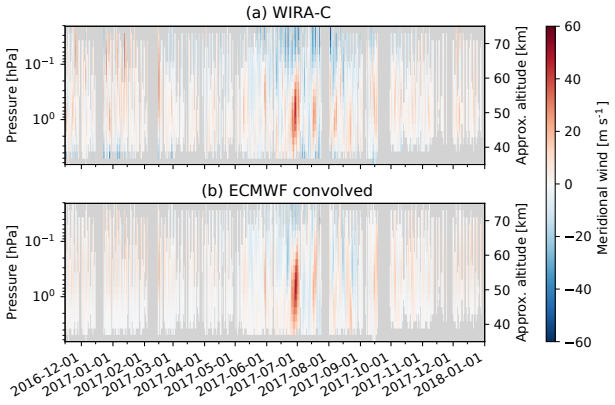

Figure 13. Same as Fig. 11 but for meridional wind. Time series of meridional wind speeds measured by WIRA-C **(a)** and ECMWF analysis data **(b)** between 14 November 2016 and 1 January 2018 for the altitude range of 35 to 75 km with a time resolution of 12 h (day and nighttime). The ECMWF data has been convolved with the averaging kernels of the retrieval in order to get the same spatial and temporal resolution for both datasets. Invalid data points are grayed out, resulting in different altitude ranges for different days. The few data gaps are due to a tropical cyclone and power outages.

the two lines-of-sight is not relevant, as WIRA-C retrieves a wind profile that best fits both observations in opposing directions. As the retrieval is not linear, this does not necessarily deliver the mean profile but an approximation thereof. For our retrieval and comparisons, we thus assume that the variation of horizontal wind speeds are negligible for 12 h integration time and horizontal distances from 150 km at 30 km altitude up to 370 km at 75 km altitude.

5.3 Results

Figures 11 and 13 show an overview over the zonal and meridional measurements from the Maïdo campaign, together with the corresponding ECMWF data, convolved in space and time. A more detailed view is given in Figs. 12 and 14 for zonal and meridional wind, respectively. There, besides the convolved ECMWF data, the model data of the nearest level is also given for comparison. At the lowest and highest levels, the difference between the fully convolved and the original ECMWF data is quite obvious. This difference is an indicator for the smoothing error, and is a consequence of the slightly worse altitude resolution and accuracy at the lowest and uppermost levels compared to the central levels where the difference nearly vanishes.

In general, the zonal and meridional wind for WIRA-C and ECMWF are consistent: firstly, the zonal wind reversal around equinox is resolved by the model as well as WIRA-C and they agree on the time of this event as well as on the magnitude. Secondly, the well-defined periods of stronger westward winds between 35 and 55 km in June are present in both datasets. Further, the increased variability with a period of approximately 10 days present at the layers between 50 and 60 km in August and September 2017 are also present in both datasets.

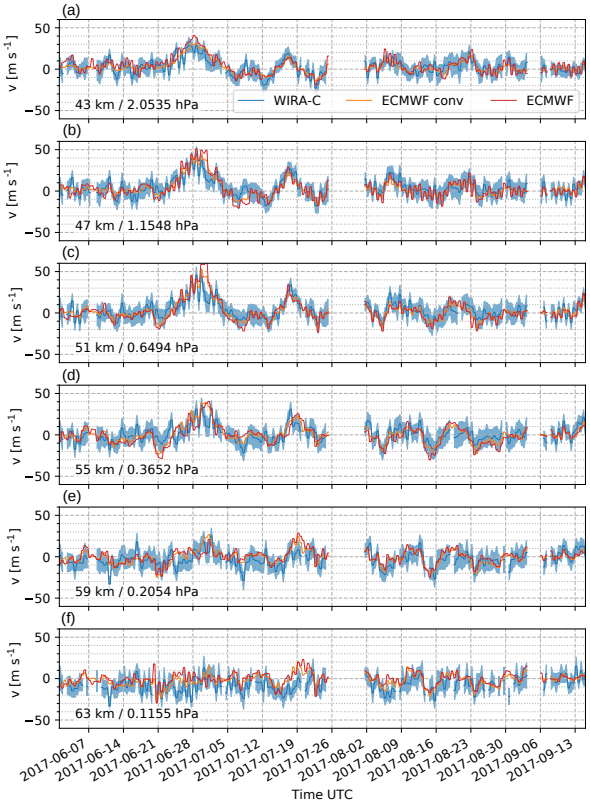

Figure 14. Same as Fig. 12 but for meridional wind. WIRA-C measurements on 10 distinct pressure levels between 35 km **(a)** to 71 km **(f)** for 1 June 2017 to 19 September 2017. The data before June 2017 and after September 2017 (shown in Fig. 11) is not represented here in order to focus on the period with more variability. The fully convolved ECMWF model data as well as the ECMWF data from the nearest pressure level (but still smoothed in time) is given for comparison. Time resolution is 12 h (day and nighttime). The light-blue area represents the uncertainty σ_o of the WIRA-C data.

There are also short periods where we can see a clear discrepancy between the model data and the measurement. For example at the layers below 45 km for the end of January and beginning of February 2017, where WIRA-C measured a smaller magnitude of zonal wind than predicted by the model for several days. This might be connected to the tropical cyclone in the Indian ocean that was the reason for the subsequent interruption of the measurement, as the instrument had to be dismounted and protected inside the building. At the uppermost levels, ECMWF has the tendency to predict a higher magnitude in zonal wind speed and to some extent also in meridional wind speed than WIRA-C. Most prominently at the end of April 2017, the model predicts a much

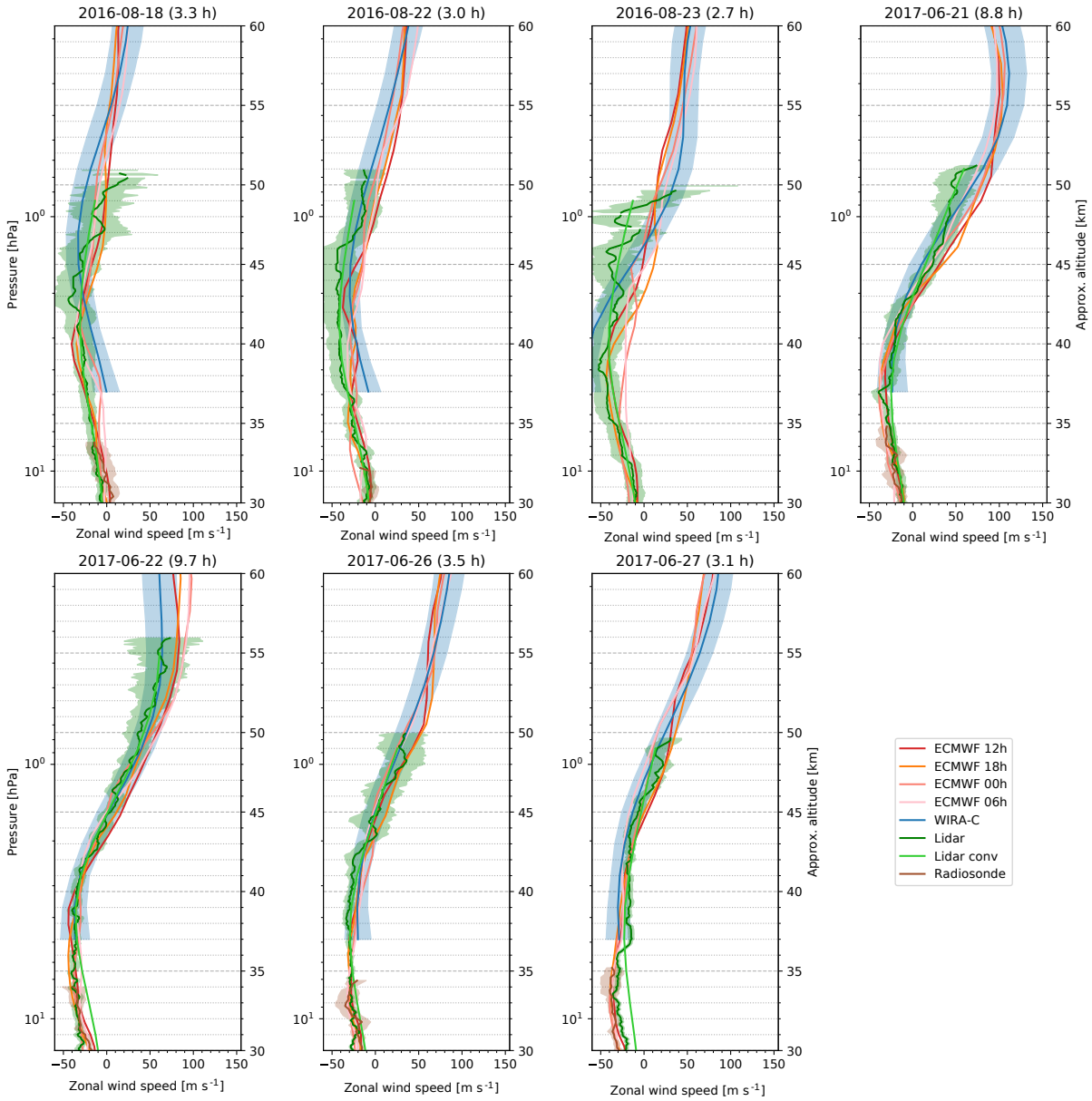

Figure 15. Seven coincident observations of zonal wind from WIRA-C and Doppler lidar from August 2016 and June 2017 together with radio soundings and ECMWF operational model data at different times, WIRA-C measurements start at 14:00 UT (18:00 LT) and lidar measurements typically between 17:00 and 20:00 UT (21:00 and 24:00 LT). The measurement time for WIRA-C is 12 h for every profile while the measurement time for the lidar observation (given in parenthesis) is typically between 3 and 3.5 h, with the exception of 21 and 22 June 2017, where measurement took 8.8 and 9.7 h, respectively. Source of radiosonde data: Météo-France.

higher magnitude in zonal wind but a lower variability. This might be an effect of the artificial forcing in the model at the uppermost layers. At the same time, our observation error increases with altitude and we cannot completely rule out, that the variability is caused by retrieval noise.

Figures 15 and 16 show all seven coincident measurements of WIRA-C and the Rayleigh–Mie Doppler wind lidar available to date for the zonal and meridional wind component, respectively. The lidar profiles have been acquired in August 2016 during routine measurements and in June 2017 during the LIDEOLE-III campaign. In addition, the corresponding ECMWF model data is shown at the four closest time steps of the model. In case of zonal wind, these ECMWF profiles are nearly identical but for the meridional

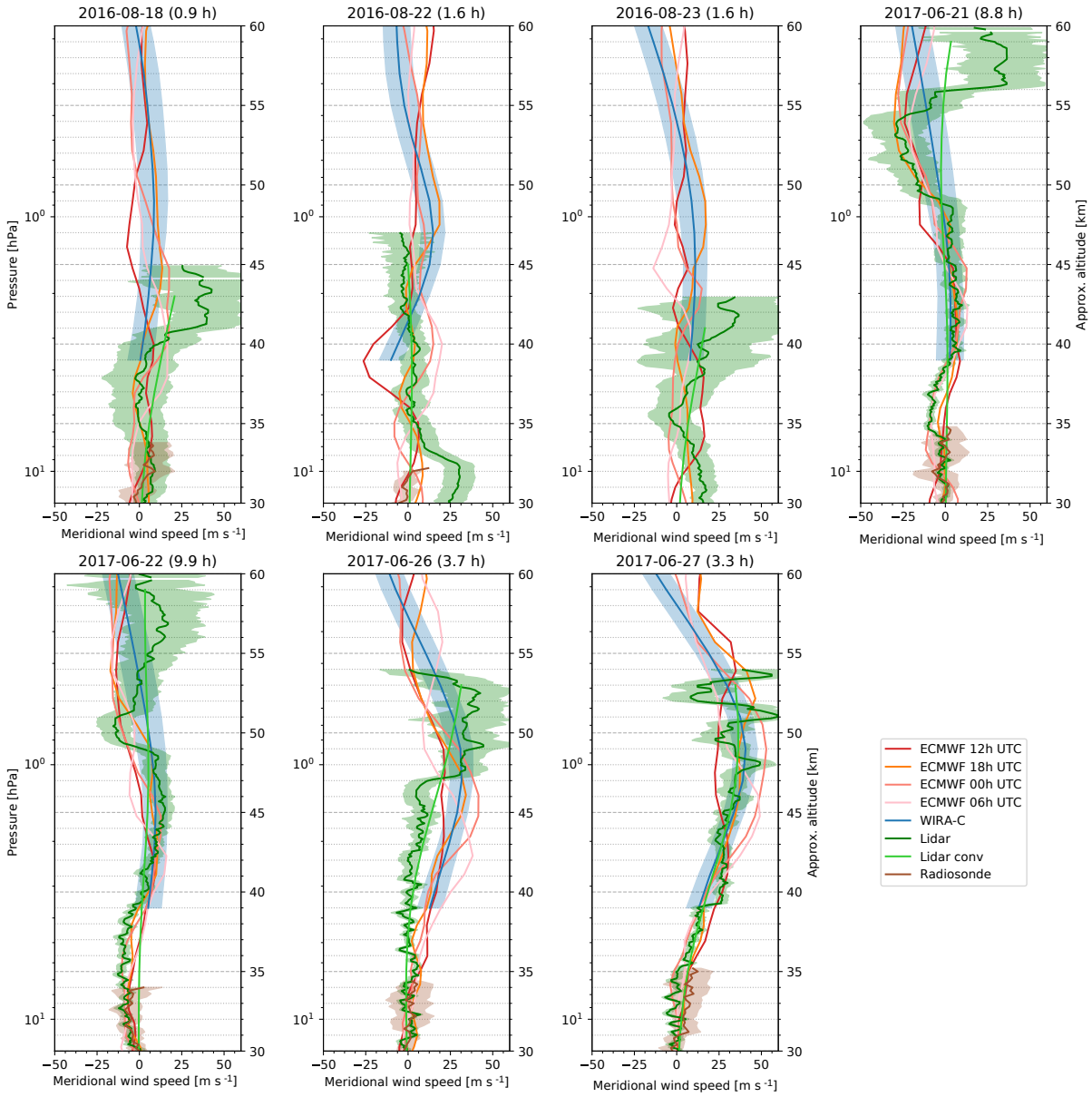

Figure 16. Seven coincident observations of meridional wind from WIRA-C and Doppler lidar from August 2016 and June 2017 together with radio soundings and ECMWF operational model data at different times, WIRA-C measurements start at 14:00 UT (18:00 LT) and lidar measurements typically between 17:00 and 20:00 UT (21:00 and 24:00 LT). The measurement time for WIRA-C is 12 h for every profile while the measurement time for the lidar observation (given in parenthesis) is typically between 1 and 4 h, with the exception of 21 and 22 June 2017, where measurement took 8.8 and 9.9 h, respectively. Source of radiosonde data: Météo-France.

wind, they indicate a high temporal variability in the model data. At the lowermost levels, the radiosonde launched at the nearby Gillot airport at noon is given for comparison where available.

For both horizontal wind components, the profiles of the three sources (WIRA-C, lidar, ECMWF) are consistent. Especially for the lidar measurements on 21 and 22 June 2017, where the whole night was used for lidar acquisition, the agreement of the two independent measurements is well within their respective uncertainties. We would like to emphasise that favourable conditions for lidar measurements, namely clear sky and nighttime, also imply lower uncertainties for the WIRA-C measurements. Remarkably, the zonal wind measurements from 22 June 2017 of WIRA-C and the

lidar are nearly identical, while the ECMWF model is offset by 20 m s^{-1} at 55 km altitude.

For the meridional wind, the lidar shows some patterns with very large vertical gradients in the wind speeds as on 18 August 2016 and 21, 22 and 26 June 2017 at an altitude around 40, 55, 48 and 47 km, respectively. These patterns are not present in the other datasets and are probably caused by internal gravity waves. For characteristics and details about such structures observed by lidar, see Khaykin et al. (2015). It is conceivable that the vertical structures observed by the lidar are simply not resolved by the ECMWF model and smoothed out by the radiometer. For example, for the measurement of the meridional wind on 21 and 22 June 2017, we can see that the convolved lidar profile and the WIRA-C measurement agree quite well while the high resolution profile of the lidar shows a layer of wind speeds with higher magnitude at 50 km altitude. This indicates that WIRA-C indeed smoothes out the feature, but that the two measurements are consistent.

6 Conclusions

WIRA-C is a new passive microwave wind radiometer designed for campaigns as well as long-term measurements. With it, the successful prototype WIRA has been replicated and improved. The optical system and the pre-amplified single side band heterodyne receiver and the spectrometer are embedded in a single housing with compact dimensions. Calibration is performed with the tipping curve scheme and tropospheric correction accounts for tropospheric inhomogeneities and normalises the spectra acquired in the four cardinal directions.

We applied an optimal estimation retrieval to combine observations in opposing directions to get a single wind profile that best represents all our measurements. The main benefit of our retrieval scheme is the availability of quality control parameters representing the whole inversion process and the increased altitude resolution of 9 to 11 km (as opposed to 10 to 16 km for WIRA). The observation error gives an estimate on the uncertainty in wind speeds caused by the thermal noise on our measurements. Its 1σ value for zonal wind is typically around 15 m s^{-1} up to 68 km or 60 km for nighttime and daytime measurements, respectively. The error on the meridional wind is approximately 9 m s^{-1} due to the smaller covariance of the a priori profile that represents the expected magnitude of the wind speeds. To complement the estimation of the random error we performed Monte Carlo estimations of possible systematic error sources. These estimations show that the expected systematic errors are lower than the random errors.

The validation campaign on the Maïdo observatory on Réunion proved that WIRA-C can provide continuous measurements of horizontal wind speeds in the altitude range of 35 to 70 km. We presented a 1-year dataset of measurements with a time resolution of 12 h and an altitude resolution of approximately 10 km for zonal and 15 km for meridional wind. Even though we retrieve ozone profiles as well, we consider them as a by-product that is only needed to fully fit the spectrum and discussion of them is not in the scope of this paper.

The measurements are consistent with the ECMWF operational analysis and also show very good agreement with the available lidar measurements from the co-located Rayleigh–Mie Doppler wind lidar. The main challenge for the comparisons is to properly account for the different integration times and spatial resolutions, especially for the lidar measurements with short acquisition times. The finer structures in the wind profiles as seen by the lidar are not resolved by WIRA-C, but the convolved profiles indicate a high consistency of the measurements. For the lidar measurements where integration has been performed during the whole night, the two independent measurements agree within their respective errors in the entire altitude range of overlap (37 to 50 km). More coincident lidar measurements would certainly be valuable for further validation.

In total we conclude that WIRA-C provides valuable continuous measurements of horizontal wind speeds covering the gap region between 35 and 70 km. These measurements are complementary to the better resolved lidar measurements, as they are continuous over more than one year and cover day and nighttime.

The next steps in passive microwave wind radiometry will go towards optimising the retrieval process and explore the lower limits of time resolution. This could include a time series retrieval as performed by Christensen and Eriksson (2013) for a water vapour instrument. Also, the possibility of wind retrievals above the Doppler broadening range could be further explored as a first comparison between WIRA and meteor radar measurements (Rüfenacht et al., 2018, Fig. A1) was very promising.

Data availability. We acknowledge ECMWF for the operational analysis data (www.ecmwf.int, last access: 23 August 2018) as well as NASA for the Aura MLS temperature profiles (http://disc.gsfc.nasa.gov/acdisc, last access: 23 August 2018) used in the retrieval. The WIRA-C data presented in this manuscript can be made available on request and are available via the ARISE data portal (arise-portal.eu, last access: 23 August 2018).

Competing interests. The authors declare that they have no conflict of interest.

Acknowledgements. This study benefited from the excellent support from the dedicated staff at the Maïdo observatory on Réunion. We acknowledge the European Communities, the Région Réunion, CNRS, and Université de la Réunion for their support and contributions in the construction phase of the research infrastructure OPAR (Observatoire de Physique de l'Atmosphère de La Réunion). OPAR is presently funded by CNRS (INSU) and Université de

La Réunion and managed by OSU-R (Observatoire des Sciences de l'Univers de La Réunion, UMS 3365). We acknowledge the French National Space Agency (CNES – Centre Nationale d'Etudes Spatiales) for supporting the wind lidar maintenance. We acknowledge the work of Jacques Porteneuve and Jean-Francois Mariscal at the Laboratoire Atmosphères, Milieux, Observations Spatiales (LATMOS) in the development an alignment of the lidar. The European Centre for Medium-Range Weather Forecasts (ECMWF) is acknowledged for providing the analysis data. We acknowledge Météo-France for providing the radiosonde data. This project has received funding from the European Union's Horizon 2020 Research and Innovation programme under grant agreement no. 653980 (ARISE2) and was supported by the Swiss National Science Foundation (SNF) under grant no. 200020-160048 and the Swiss State Secretariat for Education, Research and Innovation (SBFI) contract 15.0262/REF-1131-/52107.

Edited by: Jorge Luis Chau
Reviewed by: Alan Rogers and two anonymous referees

References

Baldwin, M. P., Stephenson, D. B., Thompson, D. W. J., Dunkerton, T. J., Charlton, A. J., and O'Neill, A.: Stratospheric memory and skill of extended-range weather forecasts, Science, 301, 636–640, https://doi.org/10.1126/science.1087143, 2003.

Baray, J.-L., Courcoux, Y., Keckhut, P., Portafaix, T., Tulet, P., Cammas, J.-P., Hauchecorne, A., Godin Beekmann, S., De Mazière, M., Hermans, C., Desmet, F., Sellegri, K., Colomb, A., Ramonet, M., Sciare, J., Vuillemin, C., Hoareau, C., Dionisi, D., Duflot, V., Vérèmes, H., Porteneuve, J., Gabarrot, F., Gaudo, T., Metzger, J.-M., Payen, G., Leclair de Bellevue, J., Barthe, C., Posny, F., Ricaud, P., Abchiche, A., and Delmas, R.: Maïdo observatory: a new high-altitude station facility at Reunion Island (21° S, 55° E) for long-term atmospheric remote sensing and in situ measurements, Atmos. Meas. Tech., 6, 2865–2877, https://doi.org/10.5194/amt-6-2865-2013, 2013.

Baron, P., Murtagh, D. P., Urban, J., Sagawa, H., Ochiai, S., Kasai, Y., Kikuchi, K., Khosrawi, F., Körnich, H., Mizobuchi, S., Sagi, K., and Yasui, M.: Observation of horizontal winds in the middle-atmosphere between 30° S and 55° N during the northern winter 2009–2010, Atmos. Chem. Phys., 13, 6049–6064, https://doi.org/10.5194/acp-13-6049-2013, 2013.

Baumgarten, G.: Doppler Rayleigh/Mie/Raman lidar for wind and temperature measurements in the middle atmosphere up to 80 km, Atmos. Meas. Tech., 3, 1509–1518, https://doi.org/10.5194/amt-3-1509-2010, 2010.

Charlton, A. J., Oneill, A., Lahoz, W., and Massacand, A.: Sensitivity of tropospheric forecasts to stratospheric initial conditions, Q. J. Roy. Meteorol. Soc., 130, 1771–1792, https://doi.org/10.1256/qj.03.167, 2004.

Christensen, O. M.: Mesospheric measurements using microwave spectroscopy, Doktorsavhandlingar vid Chalmers tekniska högskola, Ny serie, no: 3916, Department of Earth and Space Sciences, Global Environmental Measurements and Modelling, Chalmers University of Technology, 2015.

Christensen, O. M. and Eriksson, P.: Time series inversion of spectra from ground-based radiometers, Atmos. Meas. Tech., 6, 1597–1609, https://doi.org/10.5194/amt-6-1597-2013, 2013.

Eriksson, P., Buehler, S., Davis, C., Emde, C., and Lemke, O.: ARTS, the atmospheric radiative transfer simulator, version 2, J. Quant. Spectrosc. Ra., 112, 1551–1558, https://doi.org/10.1016/j.jqsrt.2011.03.001, 2011.

Ettus Research: USRP X310 High Performance Software Defined Radio (SDR) – Ettus Research, available at: https://www.ettus.com/product/details/X310-KIT (last access: 20 August 2018), 2018.

Fernandez, S., Murk, A., and Kämpfer, N.: GROMOS-C, a novel ground-based microwave radiometer for ozone measurement campaigns, Atmos. Meas. Tech., 8, 2649–2662, https://doi.org/10.5194/amt-8-2649-2015, 2015a.

Fernandez, S., Murk, A., and Kämpfer, N.: Design and Characterization of a Peltier-Cold Calibration Target for a 110-GHz Radiometer, IEEE T. Geosci. Remote, 53, 344–351, https://doi.org/10.1109/TGRS.2014.2322336, 2015b.

Han, Y. and Westwater, E. R.: Analysis and improvement of tipping calibration for ground-based microwave radiometers, IEEE T. Geosci. Remote, 38, 1260–1276, https://doi.org/10.1109/36.843018, 2000.

Ingold, T., Peter, R., and Kämpfer, N.: Weighted mean tropospheric temperature and transmittance determination at millimeter-wave frequencies for ground-based applications, Radio Sci., 33, 905–918, https://doi.org/10.1029/98RS01000, 1998.

Khaykin, S. M., Hauchecorne, A., Marqestaut, N., Posny, F., Payen, G., Porteneuve, J., and Keckhut, P.: Exploring Fine-Scale Variability of Stratospheric Wind Above the Tropical La Reunion Island Using Rayleigh-Mie Doppler Lidar, EPJ Web Conf., 176, 03004, https://doi.org/10.1051/epjconf/201817603004, 2015.

Khaykin, S. M., Hauchecorne, A., Porteneuve, J., Mariscal, J.-F., D'Almeida, E., Cammas, J.-P., Payen, G., Evan, S., and Keckhut, P.: Ground-Based Rayleigh-Mie Doppler Lidar for Wind Measurements in the Middle Atmosphere, EPJ Web Conf., 119, 13005, https://doi.org/10.1051/epjconf/201611913005, 2016.

Le Pichon, A., Assink, J. D., Heinrich, P., Blanc, E., Charlton-Perez, A., Lee, C. F., Keckhut, P., Hauchecorne, A., Rüfenacht, R., Kämpfer, N., Drob, D. P., Smets, P. S. M., Evers, L. G., Ceranna, L., Pilger, C., Ross, O., and Claud, C.: Comparison of co-located independent ground-based middle atmospheric wind and temperature measurements with numerical weather prediction models, J. Geophys. Res.-Atmos., 120, 8318–8331, https://doi.org/10.1002/2015JD023273, 2015.

Leuther, A., Tessmann, A., Massler, H., Aidam, R., Schlechtweg, M., and Ambacher, O.: 450 GHz amplifier MMIC in 50 nm metamorphic HEMT technology, in: 2012 International Conference on Indium Phosphide and Related Materials, Santa Barbara, CA, USA, 27–30 August 2012, IEEE, 229–232, https://doi.org/10.1109/ICIPRM.2012.6403365, 2012.

Martin, L., Schneebeli, M., and Mätzler, C.: ASMUWARA, a ground-based radiometer system for tropospheric monitoring, Meteorol. Z., 15, 11–17, https://doi.org/10.1127/0941-2948/2006/0092, 2006.

Murk, A., Wylde, R., Spurrett, R., Fürholz, P., and Kämpfer, N.: Blackbody calibration targets with ultralow reflectivity at submillimeter wavelengths, 4th ESA Workshop on Millimetre-Wave Technology and Applications, The 8th Topical Sym-

posium on Millimeter Waves – TSMMW2006, The 7th MINT Millimeter-Wave International Symposium – MINT-MIS2006, 15–17 February, 2006, Espoo, Finland, 359–364, https://doi.org/10.7892/boris.19296, 2006.

Ossenkopf, V.: The stability of spectroscopic instruments: A unified Allan variance computation scheme, Astron. Astrophys., 926, 915–926, https://doi.org/10.1051/0004-6361:20079188, 2007.

Rodgers, C. D.: Inverse Methods for Atmospheric Sounding – Theory and Practice, in: Series on Atmospheric, Oceanic and Planetary Physics, World Scientific, https://doi.org/10.1142/9789812813718, 2000.

Rogers, A. E., Erickson, P. J., Goncharenko, L. P., Alam, O. B., Noto, J., Kerr, R. B., and Kapali, S.: Seasonal and local solar time variation of the meridional wind at 95 km from observations of the 11.072-GHz ozone line and the 557.7-nm oxygen line, J. Atmos. Ocean. Tech., 33, 1355–1361, https://doi.org/10.1175/JTECH-D-15-0247.1, 2016.

Rüfenacht, R. and Kämpfer, N.: The importance of signals in the Doppler broadening range for middle-atmospheric microwave wind and ozone radiometry, J. Quant. Spectrosc. Ra., 199, 77–88, 2017.

Rüfenacht, R., Kämpfer, N., and Murk, A.: First middle-atmospheric zonal wind profile measurements with a new ground-based microwave Doppler-spectro-radiometer, Atmos. Meas. Tech., 5, 2647–2659, https://doi.org/10.5194/amt-5-2647-2012, 2012.

Rüfenacht, R., Murk, A., Kämpfer, N., Eriksson, P., and Buehler, S. A.: Middle-atmospheric zonal and meridional wind profiles from polar, tropical and midlatitudes with the ground-based microwave Doppler wind radiometer WIRA, Atmos. Meas. Tech., 7, 4491–4505, https://doi.org/10.5194/amt-7-4491-2014, 2014.

Rüfenacht, R., Baumgarten, G., Hildebrand, J., Schranz, F., Matthias, V., Stober, G., Lübken, F.-J., and Kämpfer, N.: Intercomparison of middle-atmospheric wind in observations and models, Atmos. Meas. Tech., 11, 1971–1987, https://doi.org/10.5194/amt-11-1971-2018, 2018.

Schanz, A., Hocke, K., and Kämpfer, N.: Daily ozone cycle in the stratosphere: global, regional and seasonal behaviour modelled with the Whole Atmosphere Community Climate Model, Atmos. Chem. Phys., 14, 7645–7663, https://doi.org/10.5194/acp-14-7645-2014, 2014.

Souprayen, C., Garnier, A., Hertzog, A., Hauchecorne, A., and Porteneuve, J.: Rayleigh–Mie Doppler wind lidar for atmospheric measurements. I. Instrumental setup, validation, and first climatological results, Appl. Optics, 38, 2410–2421, https://doi.org/10.1364/AO.38.002410, 1999.

Studer, S., Hocke, K., Schanz, A., Schmidt, H., and Kämpfer, N.: A climatology of the diurnal variations in stratospheric and mesospheric ozone over Bern, Switzerland, Atmos. Chem. Phys., 14, 5905–5919, https://doi.org/10.5194/acp-14-5905-2014, 2014.

TICRA: GRASP, available at: http://www.ticra.com/products/software/grasp (last access: 20 August 2018), 2015.

Wu, D. L., Schwartz, M. J., Waters, J. W., Limpasuvan, V., Wu, Q., and Killeen, T. L.: Mesospheric doppler wind measurements from Aura Microwave Limb Sounder (MLS), Adv. Space Res., 42, 1246–1252, https://doi.org/10.1016/j.asr.2007.06.014, 2008.

Yan, Z., Hu, X., Guo, W., Guo, S., Cheng, Y., Gong, J., and Yue, J.: Development of a mobile Doppler lidar system for wind and temperature measurements at 30–70 km, J. Quant. Spectrosc. Ra., 188, 52–59, https://doi.org/10.1016/j.jqsrt.2016.04.024, 2017.

6 Publication: Measurements of atmospheric tides

Summary

Atmospheric oscillations driven by the diurnal cycle of inslolation are called atmospheric solar tides. They are an important mechanism for the vertical coupling in the atmosphere. The variability of tides in the atmosphere and the phase relation between tides in the temperature and wind field are a topic of active research. Nevertheless, no continuous measurements of middle atmospheric tides in the wind field have been available, even tough such measurements would be highly beneficial for constraining models and retrieving data from satellites with a (quasi-) sun-synchronous orbit. Such measurements are difficult to achieve, and with an integration time of 12 to 24 hours, ground-based microwave wind radiometers have not been capable to resolve diurnal tides in the wind field. With this article, we present composite retrievals as a method to retrieve the amplitude and phase of the diurnal tide from WIRA-C measurements.

We present measurements from two campaigns (at the Maïdo observatory, 21 °S and at the ALOMAR observatory, 69 °N) and extract the amplitude and phase of the diurnal tide for a tri-monthly mean as well as for 7 to 13 day composites. We compare our measurements to the MERRA2 reanalyses data set and check the well-known properties of the diurnal tide. While we find a very good agreement between measurements and models for the tri-monthly mean, we see a much higher variability in our measurements compared to the reanalysis. Indeed we find hints for highly variable diurnal tides in our measurements. Further studies are needed to elaborate on the interesting topic of tidal variability and the phase relation between tides in the temperature and wind field. Passive microwave wind radiometry is a valuable technique to contribute to this future research, which would likely include lidar, infrasound and rocket sounding techniques.

Publication

The following article has been published in *Atmospheric Chemistry and Physics (ACP)*.

Citation: Jonas Hagen, Klemens Hocke, Gunter Stober, Simon Pfreundschuh, Axel Murk, and Niklaus Kämpfer. "First Measurements of Tides in the Stratosphere and Lower Mesosphere by Ground-Based Doppler Microwave Wind Radiometry". In: *Atmospheric Chemistry and Physics* 20.4 (Feb. 28, 2020), pp. 2367–2386. ISSN: 1680-7324. DOI: 10.5194/acp-20-2367-2020

Atmos. Chem. Phys., 20, 2367–2386, 2020
https://doi.org/10.5194/acp-20-2367-2020

Atmospheric Chemistry and Physics
Open Access
EGU

First measurements of tides in the stratosphere and lower mesosphere by ground-based Doppler microwave wind radiometry

Jonas Hagen[1], **Klemens Hocke**[1], **Gunter Stober**[1], **Simon Pfreundschuh**[2], **Axel Murk**[1], **and Niklaus Kämpfer**[1]

[1]Institute of Applied Physics, University of Bern, Bern, Switzerland
[2]Department of Space, Earth and Environment, Chalmers University of Technology, Gothenburg, Sweden

Correspondence: Jonas Hagen (jonas.hagen@iap.unibe.ch)

Received: 25 September 2019 – Discussion started: 2 October 2019
Revised: 23 January 2020 – Accepted: 24 January 2020 – Published: 28 February 2020

Abstract. Atmospheric tides are important for vertical coupling in the atmosphere, from the stratosphere down to the troposphere and up to the thermosphere. They are planetary-scale gravity waves with well-known periods that are integer fractions of a day and can be observed in the temperature or wind fields in the atmosphere. Most lidar techniques and satellites measure atmospheric tides only in the temperature field and continuous measurements of the tides in the wind field of the stratosphere and lower mesosphere are rare, even though, with modern lidars, they would be feasible. In this study, we present measurements of the diurnal tide in the wind field in the stratosphere and lower mesosphere by ground-based microwave wind radiometry for two different campaigns in tropical and polar regions. Further, we compare our measurements to MERRA-2 reanalysis data. In the tri-monthly mean, we find a good correspondence in the amplitude and phase of the diurnal tide between measurements and reanalysis with the most important features of the diurnal tides represented in both data sets. When looking at shorter timescales, we find significant differences in the data sets. We make an attempt to examine these differences and discriminate between atmospheric variability and noise, and we present some hints for intermittent diurnal tides. We conclude that continuous ground-based observations of tides in the middle atmospheric wind field are feasible, and they deliver consistent results for the mean amplitude and phase of the diurnal tide in the tri-monthly mean. We further discuss the limitations in regards to short timescale observations of tides and the possibility to provide additional insight into middle atmospheric dynamics that is complementary to temperature observations and reanalysis data.

1 Introduction

Atmospheric tides are global-scale waves with well-known periods that are integer fractions of a day. They are the result of the periodic solar forcing of the temperature and wind fields and gravity as a restoring force. Just like other gravity waves, tidal waves can propagate up- or downwards, be reflected, and they ultimately deposit energy in the atmosphere when they break. This transport and deposition of energy can cause secondary waves and other disturbances, resulting in a vertical coupling between the horizontal layers of the atmosphere and leading to an exchange of energy and momentum between the forcing regions and the dissipation altitudes. Ultimately, tides in the stratosphere and mesosphere region can affect weather phenomena like, for example, the diurnal cycle of tropical rainfall (Woolnough et al., 2004; Sakazaki et al., 2018).

Due to the global nature of atmospheric tides, they have been studied over decades using models (Lindzen, 1971; Forbes and Wu, 2006; Wang et al., 2016) or global observations from satellites (Oberheide et al., 2009; Häusler et al., 2010; Pancheva and Mukhtarov, 2011). Considering the observational results, Oberheide et al. (2011) introduced a climatology-based model of atmospheric tides covering the most relevant diurnal and semi-diurnal tidal modes at altitudes between 80 and 400 km. While atmospheric tides are

well understood and modelled (Hagan et al., 1999) on a global and seasonal scale, very little is known about tides on a local and sub-seasonal scale.

Tides in the temperature field have been extracted from satellite observations (Sakazaki et al., 2012; Forbes and Wu, 2006; McLandress et al., 1996; Oberheide et al., 2009) and have been compared to different reanalysis data sets by Sakazaki et al. (2018) from the stratosphere to the lower mesosphere. Satellites, however, often need several weeks to sample a full diurnal cycle for a specific location due to their orbit and therefore are not capable to resolve tidal variations at short timescales. The global coverage nevertheless also enables tidal studies on shorter timescales for instruments on these satellites under the assumption of a linear tide model (Ortland, 2017). Satellites with a sun-synchronous orbit, e.g. Aura MLS, overpass each location exclusively at two local times which are specific to the latitude of this location and thus their ability to resolve tides is limited.

Ground-based measurements of tides in the temperature field have been performed by day-light-capable lidars for the stratosphere by Kopp et al. (2015) and Baumgarten and Stober (2019), as well as from meteor radar temperatures (Stober et al., 2008) in the mesosphere and lower thermosphere (MLT) region. Meteor radar and medium-frequency (MF) radar observations are also suitable to obtain tides in the wind fields (Portnyagin et al., 1993, 2004; Merzlyakov et al., 2009; Jacobi, 2012; Wilhelm et al., 2019). Current lidar instruments are able to measure inertial gravity waves in the wind field on short timescales (Baumgarten et al., 2015) and are thus in theory also suited for the observation of atmospheric tides, but the necessity of clear sky conditions reduces the availability of long-term observations drastically, and no observations of atmospheric tides are available to date.

Rogers et al. (2016) derived the local solar time variation of wind at 95 km altitude by integrating a 5-year data set from different ozone radiometers. Rocket soundings of the tides in the wind and temperature fields have been performed by Lindzen and Chapman (1969) up to the upper stratosphere, but they have never been repeated again.

Note that no observations of tides in the wind field for the stratosphere and lower mesosphere have so far been performed.

This leaves reanalysis data with high temporal resolution, like ERA5 and MERRA-2, as the only source for the wind field in studies about atmospheric tides. These products typically depend on satellite measurements, and thus tides in the upper atmospheric region are poorly constrained. Recent findings by Sakazaki et al. (2018) suggest that for the temperature field, differences between the different reanalyses and measurements are systematic in amplitude (approx. 1 K or 50 % above 40 km for northern mid-latitudes, more in the tropics), and the spread between the reanalyses is quite large in the lower mesosphere (0.3 to 1 K at approx. 60 km for northern mid-latitudes).

Recently, the temporal variability of tides at the MLT, which act as lower forcing of the ionospheric and thermospheric systems, became more and more important (e.g. Liu, 2016). There are currently several global circulation models (GCMs) developed which are supposed to describe consistently the vertical coupling between the middle atmosphere and the ionospheric thermospheric system (Pancheva et al., 2012; Yiğit et al., 2016; Liu et al., 2018). In particular, the short-term variability of the tidal forcing is essential for driving the more complex neutral-ionospheric coupling in the upper atmosphere. McCormack et al. (2017) presented a comparison between a meteorological reanalysis from the Navy Global Environmental Model – High Altitude (NAVGEM-HA) and several world-wide distributed meteor radars indicating substantial day-to-day variability of the winds and tides. Recently, Baumgarten and Stober (2019) presented a 10 d continuous lidar observation conducted with the Kühlungsborn Rayleigh–Mie–Raman lidar and estimated the tidal variability using an adaptive spectral filter technique (Stober et al., 2017). They complemented these observations with reanalysis data to investigate the phase relations of temperature and wind tides. However, lidar observations require cloud-free conditions, which usually limits the continuity of such time series.

In this study, we use measurements from the ground-based microwave Doppler wind radiometer WIRA-C (WInd RAdiometer for Campaigns), which can provide continuous measurements of the wind fields in the stratosphere and lower mesosphere (Hagen et al., 2018). The biggest advantage of the radiometers compared to many other ground-based remote-sensing instruments is their ability to measure continuously and independent of daylight and light clouds. Further, their compact design makes it rather easy to deploy these instruments at remote locations and enables their autonomous operation. Rüfenacht et al. (2018) performed an initial validation of the technique with other ground-based instruments, e.g. the ALOMAR (Arctic Lidar Observatory for Middle Atmosphere Research) lidar and the Andenes meteor radar. Particularly when compared to lidar, radiometers often have much coarser vertical and temporal resolutions. Rüfenacht et al. (2016) examined the spectrum of the wind oscillations for radiometric measurements and model data for periods down to 5 d, which is the lower limit of such an analysis due the low temporal resolution of wind radiometry. In this study, we present a method to investigate sub-day periods of oscillations with microwave wind radiometry by applying a different preprocessing to the measured spectra.

Specifically, we present a method to infer diurnal tides and their variability in the wind field in the stratosphere and lower mesosphere. After a short introduction to the measurement principle and analysis methods, we present the measurements from two WIRA-C campaigns, one was conducted on Réunion island at tropical latitudes and the other one on Andøya island at polar latitudes. We show that our instrument is able to capture the mean diurnal wind tide over the

course of a 3-month period, and we compare our measurements to the meteorological reanalysis MERRA-2 (GMAO, 2015) with respect to the amplitude and phase behaviour. We do this comparison for tri-monthly means as well on shorter timescales (days or weeks) to reveal some differences between the observations and the reanalysis.

The article is structured as follows. In Sect. 2 we present a summary of the instrument and the campaigns. The data analysis and retrievals are described in Sect. 3. Our results are presented in Sect. 4, and our conclusions are given in Sect. 5.

2 The WIRA-C instrument and campaigns

2.1 Instrument

The WIRA-C instrument is a Doppler microwave wind radiometer. As described in detail by Hagen et al. (2018), it measures the 142 GHz ozone rotational emission line with a high spectral resolution of 12.5 kHz. Because the ozone molecules are moving with the mean air flow, the Doppler shift introduced to the emission line is directly proportional to the line-of-sight wind speed. In order to be sensitive to the zonal and meridional component of the horizontal wind speed, we observe the emission line for all cardinal directions (north, east, south, west) at a low elevation angle of 22°. Further, the pressure-broadening effect allows for the retrieval of altitude-resolved wind profiles in an altitude range from 30 to 75 km on a 3 km vertical grid with 12 km vertical resolution.

WIRA-C has an un-cooled but temperature-stabilized receiver with a low receiver noise temperature due to a state-of-the-art low-noise amplifier that directly amplifies the observation frequency of 142 GHz. Despite the low noise, integration times of 12 to 24 h are typically applied in the standard retrievals. These long integration times are required to achieve a signal-to-noise ratio that is sufficient for a retrieval of wind speed.

WIRA-C operates autonomously and automatically and the measurements are independent of daylight and light clouds with interruptions only during rain or heavy snowfall. Additionally WIRA-C uses a tipping curve calibration scheme, and thus it only needs very minimal maintenance, most of which can be done remotely. As a result, the WIRA-C instrument is especially well suited for campaigns as well as long-term monitoring observations.

The forward model for the retrieval is supplied by the ARTS software package (Buehler et al., 2018). The inversion of the measured spectra is performed by an optimal estimation method (OEM) developed by Rodgers (2000). We use the OEM algorithm that has recently been implemented directly into the ARTS software.

Optimal estimation is a method where the ill-posed inversion problem is regularized by an a priori profile and a corresponding covariance matrix. It is well suited for the inversion of atmospheric measurements, because the mean background state is often known reasonably well. This applies to this study in particular, where the mean background wind speed is known from models and measurements to a reasonable extent, and the diurnal cycle can be understood as a perturbation of the background state that we can retrieve from the measurements.

Different quality control parameters can be derived for an optimal estimation of a profile. The measurement response, which is the most important to us, estimates the sensitivity of the retrieved quantity to actual changes in the observed system (as opposed to sensitivity to the a priori profile). Ideally, this measurement response is one, with 0.8 or 0.6 being acceptable numbers.

2.2 Campaigns

WIRA-C has been on two major campaigns so far. The first campaign started in August 2016 and took place in the Southern Hemisphere at the Maïdo observatory on Réunion island (France) (Baray et al., 2013), located in the Indian Ocean at 21° S, 55° E. The Maïdo observatory is located at an altitude of 2200 m a.s.l., which provides ideal conditions for radiometry. At this altitude there is less absorption due to tropospheric water vapour, which could be a problem in the tropics at lower altitudes. For tropical latitudes around ±30°, the global scale wave model GSWM (Hagan et al., 1999) predicts a high amplitude of the diurnal tide compared to more polewards or more equatorial latitudes. The campaign ended in January 2018, and we refer to this as the tropical campaign.

For the second (and still ongoing) campaign, WIRA-C was moved to arctic latitudes in June 2018. The instrument is located at the ALOMAR observatory on Andøya (Norway) at 69° N, 16° E. We refer to this as the arctic campaign. The ALOMAR observatory is located on mount Ramnan, at 370 m a.s.l., and hosts many other remote-sensing instruments, e.g. the ALOMAR Rayleigh–Mie–Raman lidar, an Fe-lidar and several radars in the vicinity. The water vapour cycle at ALOMAR is dominated by the tropospheric weather pattern of the marine climate and variable within days rather than within a day.

3 Data processing

For the standard WIRA-C time series retrievals as used in previous studies, the spectra are integrated over continuous blocks of 12 or 24 h, resulting in a time series of wind speed with the same resolution (Hagen et al., 2018). Typically, for the tropical site, an integration over 12 h from sunrise to sunset is performed. However, for the retrieval of the daily cycle, we now aggregate the measurements of the same time of day over multiple days to perform a composite analysis. Typically, we use a window of 7 to 13 d and aggregate by time of

day with a 2 to 4 h resolution. This gives a total integration time of around 20 h, centred around a central day. We refer to the different composites by (δD, δH), where δD indicates the number of days and δH the number of hours for the integration. The main composite used in this study is (13, 2), which gives a total integration time of 26 h.

After integration we run the wind retrieval for the WIRA-C instrument. For MERRA-2 reanalysis data, we apply the same aggregation directly on the model data to get the same temporal smoothing that we have to apply to our measurements. In addition, we also analyse the original reanalysis data.

A major difference to the retrieval described by Hagen et al. (2018) is that we use a non-zero wind a priori profile that corresponds to the mean wind background. This mitigates the effect of the diurnal variability of the troposphere on our measurements. If a zero-wind a priori is used, increased noise during daytime could lead to an overestimation of tidal amplitudes in the subsequent analysis, because the retrieved wind speed would be closer to zero (and thus possibly further away from the background) in the case of increased noise during daytime. In contrast, a mean-background a priori in combination with poor measurement response would lead to an underestimation of tidal amplitudes. This is especially important for locations with high diurnal variability (like our tropical site) or frequent rainfall (like our arctic site close to the sea). We extract the mean wind background from ECMWF operational data and average over the full 13 d centred around the (13, 2) composite, analogously to the other composites. Like this, our a priori wind profile does not include any tidal information at all. For the ozone a priori data, we aggregate WACCM data from Schanz et al. (2014), analogously to our measurements.

Once we have retrieved the wind profiles (or extracted them from the reanalysis data), we fit a simple tidal model to extract amplitude and phase information. The simple model for an arbitrary observable quantity y has the form of

$$y(t) = c + \sum_{k=1\ldots N} A_k \cos\left(t\frac{2\pi}{P_k} - \phi_k\right) \tag{1}$$

$$= c + \sum_{k=1\ldots N}\left[a_k \cos\left(t\frac{2\pi}{P_k}\right) + b_k \sin\left(t\frac{2\pi}{P_k}\right)\right], \tag{2}$$

where $P_k = 24, 12, 8, \ldots$ h is the period of the diurnal, semi-diurnal and ter-diurnal tide. In this study we use $N = 1$ and only consider the diurnal tide, but we write down the full basis in Eq. (2) to point out that the components for $k = 1, 2, 3, \ldots$ are orthogonal and can thus be treated separately. We apply a least-squares optimization on Eq. (2) for the zonal and meridional wind components, and we assume the same weight for all wind measurements. Additionally, we estimate the uncertainty of the fit from the error covariance matrix of the adjusted parameters.

Equation (1) defines the phase ϕ_k as the time of day when the corresponding wind component has its maximum. Note that we present phases in units of mean solar time, so, for example, a phase of 10 h means that the maximum occurs 2 h before noon of the mean solar day. The amplitude A_1 and phase ϕ_1 of the diurnal tide are finally given by

$$A_1 = \sqrt{a_1^2 + b_1^2}, \tag{3}$$

$$\phi_1 = \mathrm{acrtan2}\,(b_1, a_1) \in (-\pi, \pi]. \tag{4}$$

Since we average over multiple days prior to the retrieval, we do not apply a windowing function for the fitting of the tide as it is often suggested to compensate for the intermittency of waves. We assume that the retrieval of averaged spectra yields the average wind speed, so windowing and aggregation can be considered equivalent. This assumption might not hold true in the context of fast changes in the wind field, and we thus prefer periods of a stable wind background for our detailed analysis. We especially do not attempt to retrieve tidal parameters during strong planetary wave activity nor in the context of extreme events like sudden stratospheric warmings. Further, we consider non-tidal gravity waves to be filtered out by the vertical smoothing of the instrument of about 12 km.

Vertical smoothing (artificially or due to instrumental properties) decreases tidal amplitudes depending on the vertical wavelength of the observed tides. If the vertical wavelength is infinite (tidal phase is constant with altitude) the amplitude is not affected, whereas at typical vertical wavelengths of the diurnal tide of around 30 km, the smoothing can reduce the observed amplitude by up to 0.25. In this study, we do not apply any vertical smoothing to the reanalysis data.

To check for the significance and robustness of the diurnal tidal parameters, we compare the outcome for different composites. We run the same analysis for the (13, 2), (11, 2), (9, 3), (9, 2), (7, 4) and (7, 3) composites, which provide different samplings of the same observable. The similarities and differences among all the composites indicate how robust the parameters are and allow us to estimate the influence of noise from instrumental and atmospheric sources in a qualitative way.

We also compute the mean amplitude and phase over a larger time span (3 months) by averaging the wind field prior to fitting the tide model. We estimate the uncertainty of the amplitude and phase for the tri-monthly mean using a bootstrapping method that follows the moving block bootstrap (Lahiri, 2003, p.25ff). For a (δD, δH) composite time series, we sample a synthetic 3-month period (91 d) by choosing $\frac{91}{\delta \mathrm{D}}$ composite days at random, and we estimate the diurnal tidal parameters of the mean diurnal cycle for each sample. The distribution of the parameters gives us an estimate of the uncertainty due to observational errors as well as due to phase variability during the period of observation.

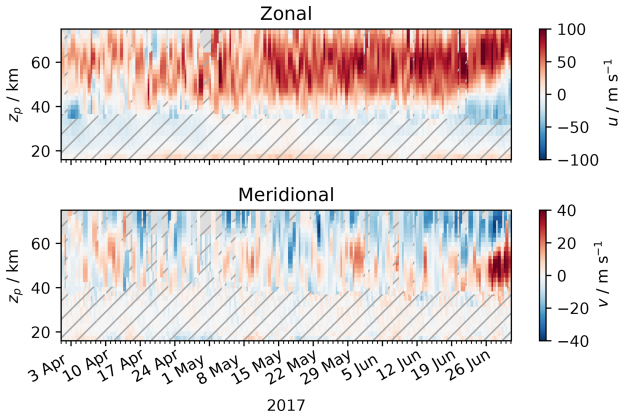

Figure 1. Background wind speed measured by WIRA-C complemented with MERRA-2 reanalysis data (hatching) for the tropical campaign. Note the different scales for the zonal and meridional components.

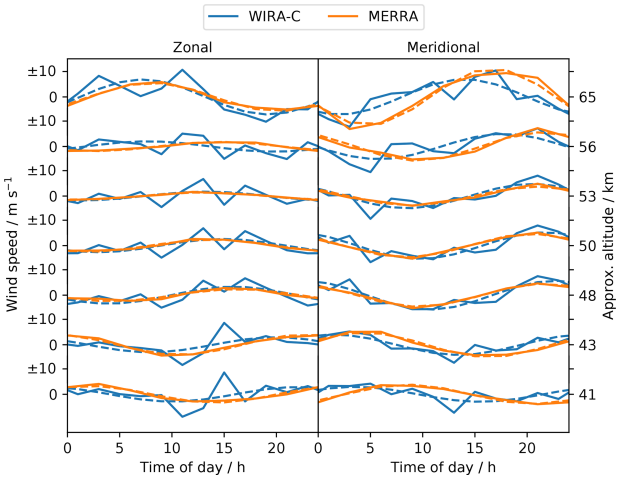

Figure 2. Mean daily cycle of zonal and meridional wind speeds at different altitudes for the 3 months during the tropical campaign from MERRA-2 and WIRA-C. Dashed lines indicate the best fit of the diurnal tide model.

4 Results

From both campaigns we select a 3-month period based on the following criteria. First we look for periods with stable background wind conditions. Due to the aggregation (maximum 13 d) for the wind retrieval, we prefer time intervals with no extreme meteorological events, e.g. sudden stratospheric warmings (SSWs), and a low planetary wave activity, because this might impact the retrieval of tidal amplitudes.

Further, we only considered time intervals with a good overall measurement response, which corresponds mainly to little precipitation. Another important aspect for the data analysis is the continuity of the observations (minimal instrumental downtime) to avoid issues in compiling the temporal averages.

Considering the above-mentioned criteria, we decided to focus on two campaign intervals from April to June 2017 at Maïdo and from September to November 2018 at Andenes (ALOMAR).

This gives us two time series for which we perform the previously described analysis: one for the tropical campaign and one for the arctic campaign. We use local mean solar time for all plots and phases in this study, which is simply a fixed offset depending on longitude. For the tropical campaign at 55.5° E, this is an offset to Universal Time (UT) of 3.7 h. For the arctic campaign at 15.7° E, the offset of local mean solar time to UT is 1 h.

4.1 Results for the tropical campaign

For the tropical campaign, we selected the period from April to June 2017. This period is at the beginning of austral winter, where the reanalysis as well as measurements shows a steady background of strong eastward winds with a small meridional component and relatively low planetary wave activity. Moreover, during this rather dry season, WIRA-C performed well and measured continuously with a good measurement response.

The meteorological background wind field for the selected period at the Maïdo observatory is shown in Fig. 1 as measured by WIRA-C, complemented with MERRA-2 reanalysis data for lower altitudes. The zonal and meridional winds indicate some variability at temporal scales of a few days. Characteristic of the zonal winds are westward winds below 40 km altitude and a strong zonal eastward stratospheric jet from 45 to 70 km altitude, which intensifies at the beginning of May. Meridional winds exhibit a steady change between southward and northward winds within a few days. Corresponding to the zonal wind enhancement, meridional winds become more southward at the beginning of May above a height of 60 km.

The average diurnal cycle at different altitudes over the whole 3-month period is shown in Fig. 2 for WIRA-C measurements and the MERRA-2 reanalysis. In both data sets, the diurnal tide is readily visible. The reanalysis data seem not to contain any other modes than the diurnal tide, and the tide model from Eq. (2) fully fits the data. The measurements expose some more variability, especially at higher altitudes and during the afternoon hours. This is related to increased noise in the measurement in the afternoon hours, which is most prominent for the westward observation direction (and thus only seen in zonal wind retrievals) due to local weather patterns at the Maïdo observatory on Réunion island.

The agreement between MERRA-2 and the WIRA-C wind retrievals with respect to the mean behaviour can be assessed in Fig. 3. The left panel (Fig. 3a) shows the amplitude of the zonal and meridional mean diurnal cycle over the entire campaign period for WIRA-C and MERRA-2. Both data sets

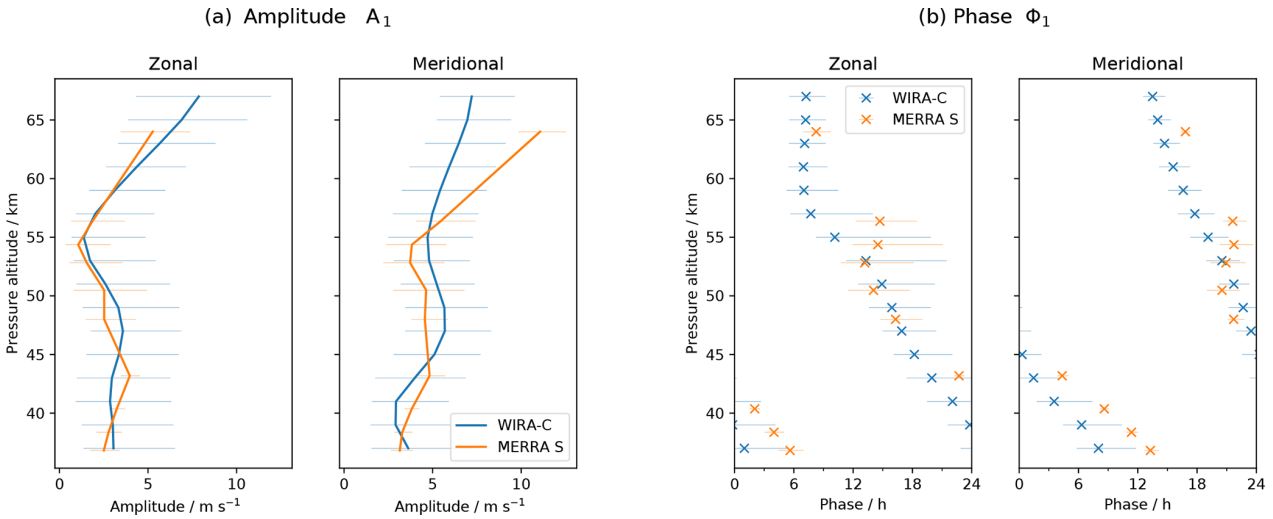

Figure 3. Amplitude and phase of mean daily cycle over 3 months from MERRA-2 reanalysis and WIRA-C measurements from the tropical campaign. Error bars indicate 95 % confidence limits. Phase is equivalent to solar time of maximum.

show a similar profile with relatively low amplitudes of less than 5 m s^{-1} below 55 km and slightly higher amplitudes for the meridional component. Figure 3b shows the same for the vertical phase behaviour. The profiles of measurements and reanalysis are in agreement with respect to the amplitudes and phases up to an altitude of 55 km for the tropical location, where the reanalysis data lie within or are close to the limits of confidence of our measurements. The amplitude of the diurnal tide agrees for the measurement and reanalysis within or close to their limits of confidence. Above 55 km altitude, an increased discrepancy is evident for the meridional wind between MERRA-2 and the radiometer.

The phase of the mean daily cycle measured by WIRA-C as shown in Fig. 3b indicates a vertical wavelength of about 30 km. Approximately the same vertical wavelength is found in the reanalysis. Above 55 km altitude, the vertical wavelength of our measurements increases drastically, and the phase eventually becomes constant with altitude. Evidently, the tide seen by WIRA-C lags behind the tide represented in the reanalysis by 5 h at the lowermost altitude levels. Currently, we cannot explain this offset.

Figure 4b shows the phase difference between zonal and meridional diurnal tide. Measurements and reanalysis show a remarkable agreement and show that the meridional tide leads the zonal tide by approximately 6 h (90° phase angle) as is expected for the Southern Hemisphere.

Besides the tri-monthly mean, we show the diurnal tidal amplitude A_1 and phase ϕ_1 versus time for the whole period in Fig. 5. The upper two panels (Fig. 5a and b) show the WIRA-C retrievals. The central two panels (Fig. 5c and d) are obtained from the aggregated MERRA-2 reanalysis, whereas the bottom two panels (Fig. 5e and f) show the data for the original MERRA-2 reanalysis. These figures present

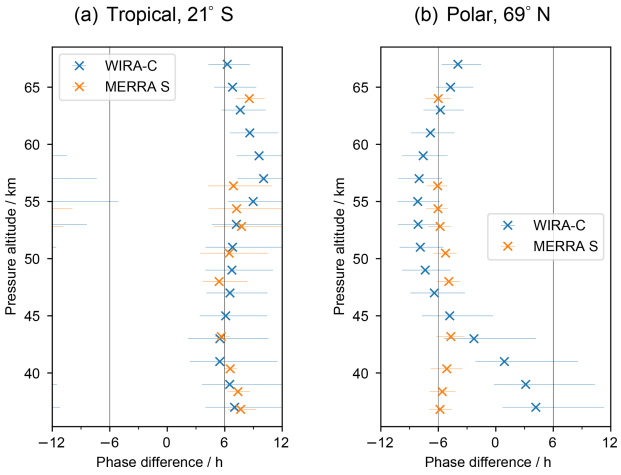

Figure 4. Phase difference between meridional and zonal diurnal wind tide ($\Delta\phi$=$\phi_{\text{merid.}}-\phi_{\text{zonal}}$) for the tropical and arctic campaigns in WIRA-C measurements and the MERRA-2 reanalysis.

the outcome for the (13, 2) composite only, and we provide five more composites in the Appendix in Figs. A1 and A2 for the tropical campaign. The WIRA-C diurnal tidal amplitudes reach a maximum at the beginning of the campaign of about 16 to 20 m s^{-1} for both components. During the second phase of the campaign we observe smaller tidal amplitudes of approximately 4 to 12 m s^{-1}. The vertical structure that is obvious in Fig. 5a can also be seen in the tri-monthly mean (Fig. 3a) with a minimum at 55 km. Because we observe a similar oscillating pattern of tidal amplitude with altitude in measurements and reanalysis (Fig. 3a), we propose the mixing of different tidal waves with different vertical

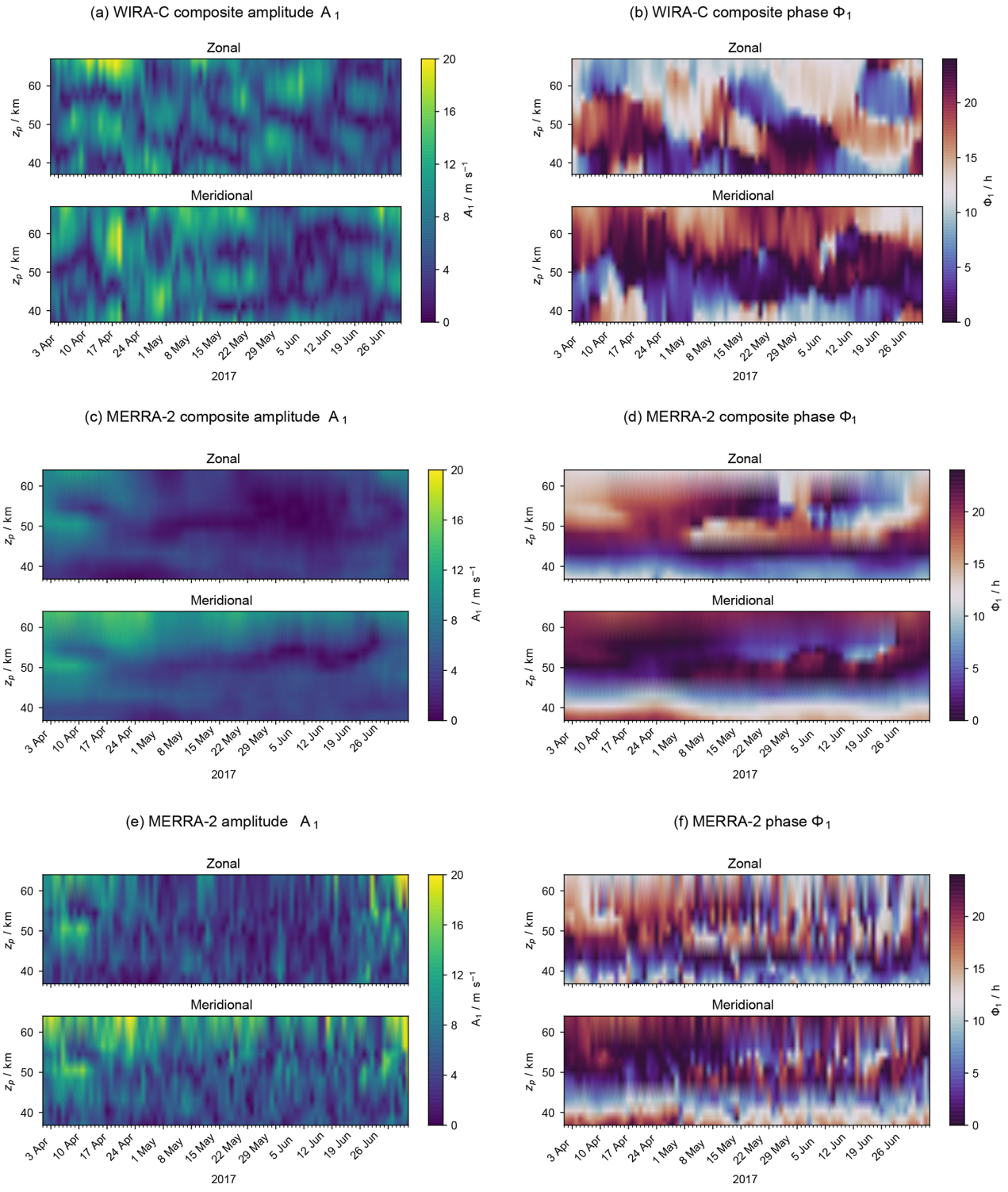

Figure 5. Amplitude and phase of the diurnal tide over 3 months from WIRA-C measurements **(a, b)**, smoothed MERRA-2 reanalysis **(c, d)**, and original MERRA-2 **(e, f)** during the tropical campaign at the Maïdo observatory.

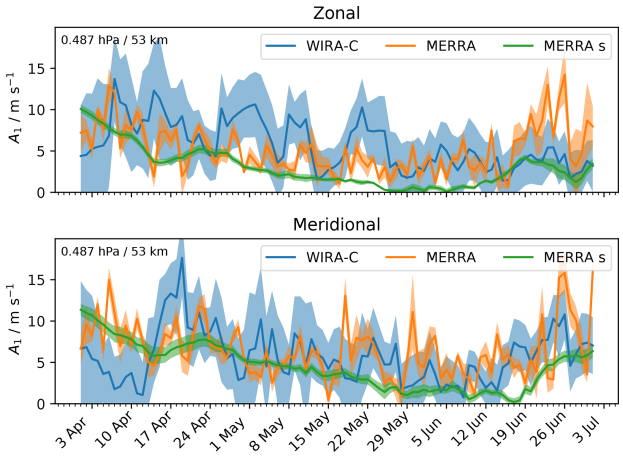

Figure 6. Time series of zonal and meridional diurnal tide amplitudes during the tropical campaign for measurements (WIRA-C), MERRA-2 reanalysis (MERRA) and reanalysis smoothed (MERRA s) at an altitude level of 53 km with corresponding errors of the model fit as shaded area.

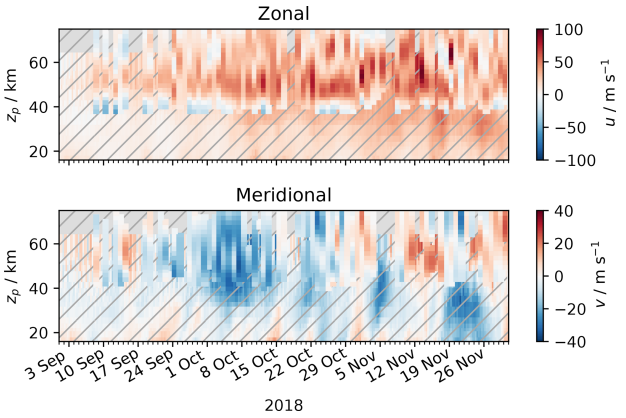

Figure 7. Background wind speed measured by WIRA-C complemented with MERRA-2 reanalysis data (hatching) for the arctic campaign. Note the different scales for the zonal and meridional components.

wavelengths or propagation directions as a possible source for this structure. The augmented magnitude of the structure in our measurements compared to reanalysis data might still be due to slight oscillations of the retrieval.

Further, our observations show a strong time dependence of the diurnal tidal amplitude and phase at the resolved temporal scales of 7 to 13 d. We observe the same morphology in the time series for all composites (Figs. A1 and A2), and we take this as a hint that the variability is not only due to noise. Nevertheless, there are some differences between the different composites, especially in the absolute values of the amplitudes that are most probably related to instrumental noise. The phase, on the other hand, is more robust, and the time series of the diurnal tidal phase has the same structure in all composites and exposes a pattern of the diurnal tidal phase modulated with a period of approximately a month.

Compared to the WIRA-C observations, the MERRA-2 reanalysis data show a constant amplitude and phase over time in the composite analysis (Fig. 5c and d). The original MERRA-2 data as shown in Fig. 5e and f are less constant over time, and phase and amplitude expose a high day-to-day variability. However, the mean behaviour seems to be in good agreement with the observations, and the general morphology of the diurnal tide in amplitude and phase seems to agree between measurements and reanalysis.

Figure 6 shows a comparison of the time series between WIRA-C and the MERRA-2 reanalysis at an altitude of 55 km. The shaded area represents the uncertainties of the estimated diurnal tidal amplitudes taken from the covariance of the adjusted parameters. In addition to the MERRA-2 reanalysis that has been smoothed with our integration kernel, we show the tidal analysis of the original MERRA-2 data. This comparison indicates how the diurnal tidal amplitude decreases and increases again during the campaign in the measurements as well as in the reanalysis. MERRA-2 and our measurements show larger diurnal tidal amplitudes at the beginning of the tropical campaign in April, which then decrease in May and June.

4.2 Results for the arctic campaign

From the ongoing arctic campaign in Andenes (ALOMAR), we selected September, October and November 2018 for our analysis. The measurement response during these months is between 0.8 and 1.2 between 42 and 62 km and between 0.7 and 1.3 between 39 and 69 km, and therefore it is acceptable for the whole altitude range we cover. We did not choose this period to start earlier because of the biannual wind reversal that took place just before September 2018 and, on the other end, we did not expand this period to December because of the major sudden stratospheric warming that took place in this winter (Schranz et al., 2019).

For this period, the meteorological situation is dominated by the fall transition in the stratosphere. The corresponding background wind field retrieval from WIRA-C is shown in Fig. 7. The campaign period starts at the end of summer with a weak eastward zonal jet between 45 and 55 km altitude, which evolves into a typical polar vortex until November covering nearly all observed altitudes from 40 to 70 km. Meridional winds are dominated by a southward flow at the beginning of the campaign period, which then reverses into a northward wind regime at the end of October. Both wind components indicate some variability due to waves on temporal scales of a few days; in particular, the meridional wind indicates an onset of the planetary wave activity towards the end of the observation period.

Figure 8 shows the diurnal cycle, averaged over the 3 months during the arctic campaign. The reanalysis data

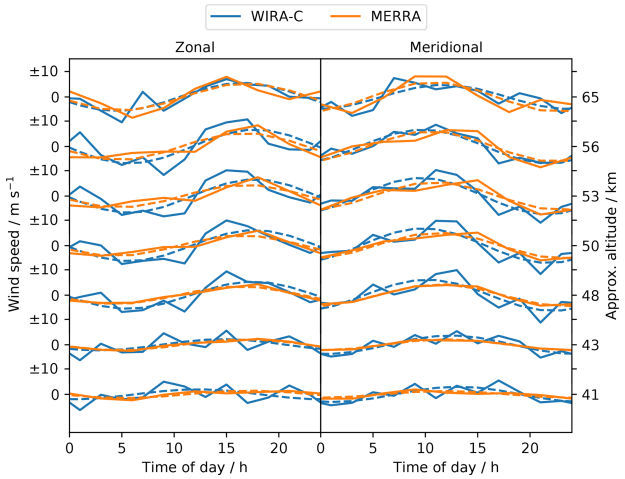

Figure 8. Mean daily cycle of zonal and meridional wind speeds at different altitudes for the 3 months during the arctic campaign from MERRA-2 and WIRA-C. Dashed lines indicate the best fit of the diurnal tide model.

are well fitted by our diurnal tide model at all altitudes, but the presence of a semi-diurnal component is indicated by the slight oscillation of the reanalysis data around the diurnal tide model fit. The WIRA-C measurements are well represented by the simple diurnal tide model, while containing some higher-frequency oscillations that could originate in higher mode oscillation as well as measurement noise.

Figure 9 shows amplitude and phase profiles of the mean daily cycle of this period. Measurements and reanalysis mostly agree and show the same structure of the diurnal tidal amplitude and phase. Still as seen in Fig. 9a, WIRA-C measures a higher diurnal amplitude than the reanalysis suggests. Here, the offset in amplitude seems to be systematic since, for the most part, the profiles do not agree within their limits of confidence even though they show the same structure.

The phase of the mean daily cycle is shown in Fig. 9b. Both data sets show a situation with infinite vertical wavelength above 45 km. The maximum of the diurnal tide is around noon and 18:00 local time for the zonal and meridional components, respectively.

The phase difference between zonal and meridional components in the tri-monthly mean is shown in Fig. 4a. Above 45 km, the zonal tide leads the meridional tide by 6 h (90° phase angle), as expected for the Northern Hemisphere. Below 45 km, the phase of the zonal component starts to deviate in the measurements and lags behind the meridional tide at approximately 40 km altitude.

Figure 10 shows extracted amplitudes and phases of the diurnal tide for the arctic campaign over time and altitude. The panels on the left (Fig. 10a, c and e) show the diurnal tidal amplitude A_1 for the WIRA-C measurements and the MERRA-2 composite and original reanalysis, respectively. In the measurements, the diurnal tide is stronger in September than it is in October and reaches nearly 20 m s^{-1} in the meridional component by the end of September. Again, this is most probably related to augmentation of tides by weaker background wind speed caused by the seasonal wind reversal that took place at the end of August to beginning of September 2018. But also during October and November, diurnal tidal amplitudes are quite strong, often up to or more than 15 m s^{-1}. This is different for the composite reanalysis data, where amplitudes are generally lower than 10 m s^{-1}. In the non-smoothed reanalysis data, tidal amplitudes of more than 15 m s^{-1} are also reached.

The extracted diurnal tidal phase ϕ_1 is shown in Fig. 10b and d for the measurement and reanalysis, respectively. In general, the reanalysis shows a very stable phase with the maximum of the diurnal tide at noon local time for the zonal component and 18:00 local time for the meridional component. Only in November does the phase becomes more variable and expose some structure which might be related to the onset of planetary wave activity. This applies to the smoothed and original MERRA-2 data equally and is in strong contrast to the measurements, where the diurnal tidal phase is highly variable with time and altitude on the presented timescales. Because this time dependence is present in all composites with the same morphology, we partly attribute it to the intermittency of the diurnal tide, while the exact value of the phase might still be subject to noise.

As for the tropical campaign, we discuss the (13, 2) composite and provide a total of six composites in the Appendix (Figs. A3 and A4). Again we see the same morphology and time dependence of amplitude and phase in all composites. While the amplitude is less consistent among the composites due to noise, the phase is more robust.

Figure 11 shows the time series for one specific altitude level (53 km) and additionally shows the amplitudes of the original reanalysis data that have not been aggregated over multiple days. Especially in November, the original reanalysis data show a variability that is comparable or even stronger when compared to the measurements. By applying the aggregation, this variability is averaged out from the reanalysis data but not entirely from the WIRA-C measurements. If this variability comes from the atmosphere as opposed to instrumental noise, this would indicate that the coherence time of short-timescale disturbances of the diurnal tide might actually be longer than the reanalysis predicts. Notably, the measured amplitude features a disturbance around 24 September, where the zonal amplitude is close to zero and the meridional amplitude exhibits a maximum. Similar dynamics are not represented in the reanalysis data, not even in the (non-smoothed) original reanalysis data.

4.3 Summary

We presented measurements of the diurnal tide in the wind field in the stratosphere and lower mesosphere. To our knowledge, these are the first direct observations of tides in the

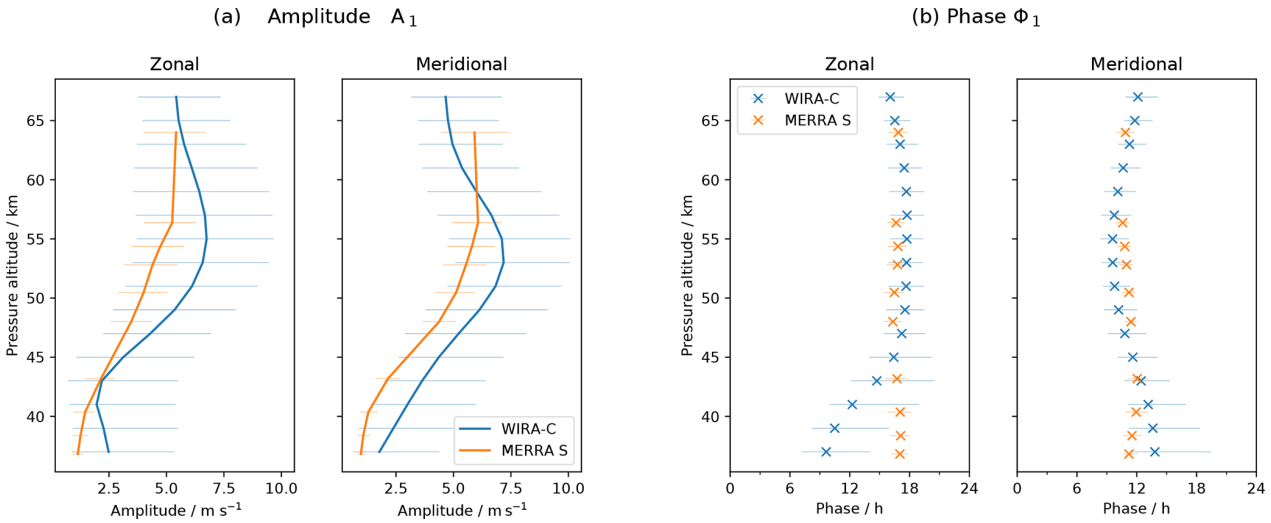

Figure 9. Amplitude and phase of mean daily cycle over 3 months from MERRA-2 reanalysis and WIRA-C measurements from the arctic campaign. Error bars indicate 95 % confidence limits. Phase is equivalent to solar time of maximum.

wind field in the middle atmosphere (30 to 70 km) with ground-based instruments. In contrast to the standard time series retrievals applied in previous studies, we apply a composite analysis and superpose spectra for the same time of day over several days. This composite analysis enables us to resolve tidal structures in the wind field.

To investigate the results of our method, we applied our analysis to two 3-month periods from different campaigns: one from the Southern Hemisphere and one from the Northern Hemisphere.

The averaged data over the 3-month periods showed basic and well-known properties of the diurnal tide with different details for the Northern Hemisphere and Southern Hemisphere. Notably we observed an increasing amplitude with altitude, reasonable vertical wavelengths, and a 6 h (90° phase angle) shift between zonal and meridional component with the leading component being different for the austral and boreal locations.

We compared our wind measurements to the MERRA-2 reanalysis, which has already been compared by Sakazaki et al. (2018) to other data sets in regards to tides in the temperature field. We find a good overall correspondence between reanalysis and measurements in the amplitude of the diurnal tide in the wind field and temporal evolution thereof. Further, the amplitude and phase profiles for the tri-monthly mean wind field correspond between the radiometer and the meteorological reanalysis, mostly within their uncertainties for the tropical campaign and with a small offset for the arctic campaign. While the phase of the diurnal tide is very stable in the reanalysis data, especially in the polar region and sometimes even stationary, we see a big temporal variation in the phase in our measurements, which persists among different composites.

Further, we presented a time series of the diurnal tidal amplitude and phase over two 3-month periods. We observed an augmented diurnal tide in the context of weak background wind speeds after seasonal wind reversals. Looking at shorter timescales, we observe strong temporal variability of the amplitudes and especially of the phase. Certainly, the time dependence of the diurnal tidal phase has to be investigated in further studies. Since we see the same time dependence in all our composites, we conclude that intermittent diurnal tides could be a possible explanation.

5 Conclusions

In summary, we find that reanalysis and measurements agree on the tidal component in the tri-monthly mean daily cycle. We conclude that the MERRA-2 reanalysis captures the amplitude and phase of the mean diurnal tide reasonably well when averaging over 3 months or longer. When looking at shorter timescales, obvious differences between model and measurements appear. We can explain some of the differences, like the augmented tide, in the context of weak background winds and also observe other notable differences like the variable phase in measurements that are not represented in the MERRA-2 product. Since the general morphology of the variable phase is the same among all composites, we conclude that it might be caused by actual atmospheric variability of the tide. While these intermittent structures are present to some extent in the reanalysis data as well, they are averaged out when we apply the 13 d smoothing that is equivalent to the composite of our measurement. A possible explanation would be that the coherence time of short-timescale disturbances of the diurnal tide is longer, and variability is in general stronger in reality than in the reanalysis model. On

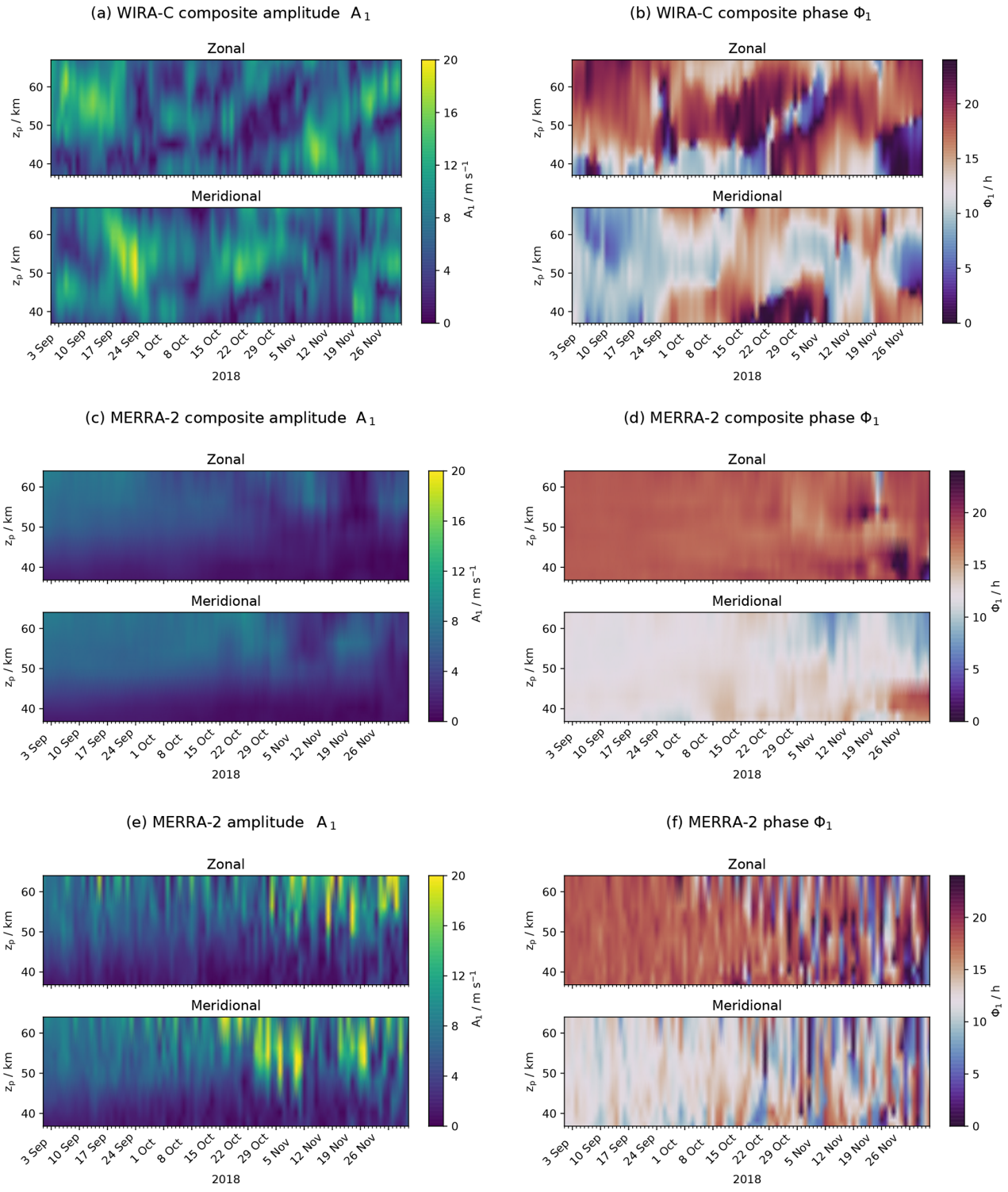

Figure 10. Amplitude and phase of the diurnal tide over 3 months from WIRA-C measurements **(a, b)**, smoothed MERRA-2 reanalysis **(c, d)** and original MERRA-2 **(e, f)** during the arctic campaign at the ALOMAR observatory.

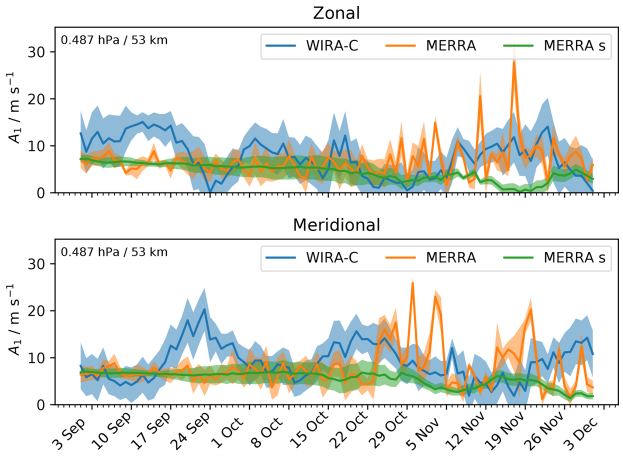

Figure 11. Time series of zonal and meridional diurnal tide amplitudes during the arctic campaign for measurements (WIRA-C), MERRA-2 reanalysis (MERRA) and reanalysis smoothed (MERRA s) at an altitude level of 53 km with corresponding errors of the model fit as shaded area.

the other hand, our study is based on a composite analysis, and we assume that the diurnal tide is reasonably stationary during our 7 to 13 d window. Baumgarten and Stober (2019), based on temperature lidar observations with high temporal resolution, provide some evidence that tides can be highly variable and aggregation windows should be no longer than a few days.

Further studies could develop more elaborate methods to extract tidal information from radiometer data and further constrain the uncertainty on the extracted parameters. Diurnal tide measurements from daylight-capable lidar or even from rocket campaigns would be a possible source of comparison data. Also other models, for example NAVGEM-HA, could provide further comparison data on different timescales.

In this study, we focused on the diurnal tidal component only. Future studies could as well address the semi-diurnal component using the same or different composites.

We required a stationary background and focused on selected periods which satisfy this condition. Further studies could investigate the necessity or this requirement and retrieve tides while taking a variable background into account.

Ground-based microwave radiometers are capable of measuring continuously over decades and can be deployed in tropical and polar latitudes with minimal maintenance and deployment effort. This makes these instruments very valuable to observe dynamics in the atmosphere, especially from 30 to 70 km altitude where observations are scarce. Since tidal waves on sub-seasonal and regional scales play an important role in the dynamics of the atmosphere, such observations are highly valuable.

Appendix A: Diurnal tide amplitude and phase for all composites

Figures A1, A2, A3 and A4 contain panels with the extracted amplitude and phase of the diurnal tide in the wind field for six different composites of the WIRA-C wind measurements. We refer to the different composites by (ΔD, ΔH), where ΔD indicates the number of days and ΔH the number of hours for the integration; the total integration time is thus given by $\Delta D \times \Delta H$ and ranges from 21 to 28 h for the presented composites. We select these six composites because they all have an integration time of around 24 h and provide different window lengths (7 to 13 d) and different resolutions (2 to 4 h).

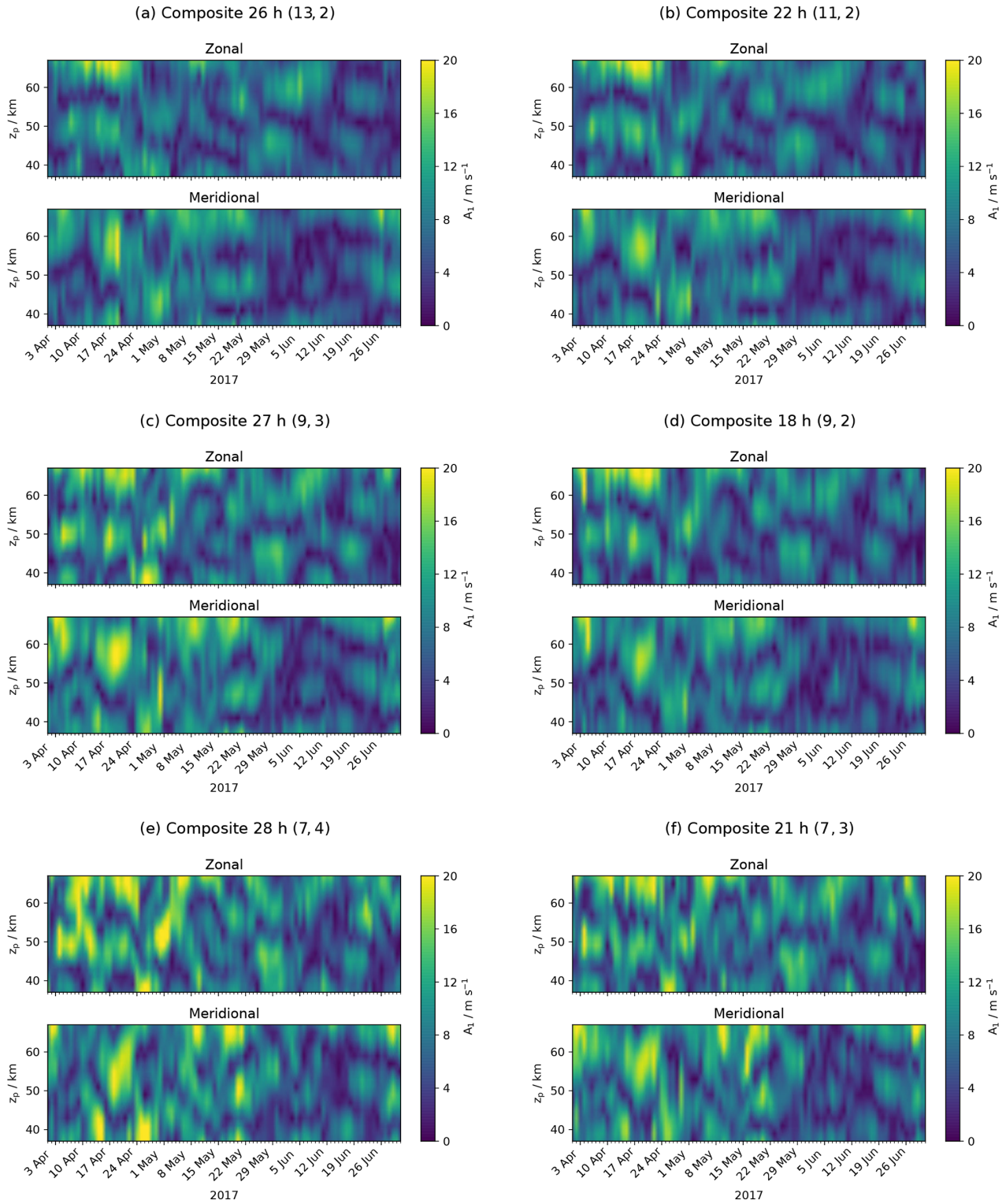

Figure A1. Tropical campaign: amplitude of the diurnal tide for six different composites with a similar total integration time of 21 to 28 h ordered by window length.

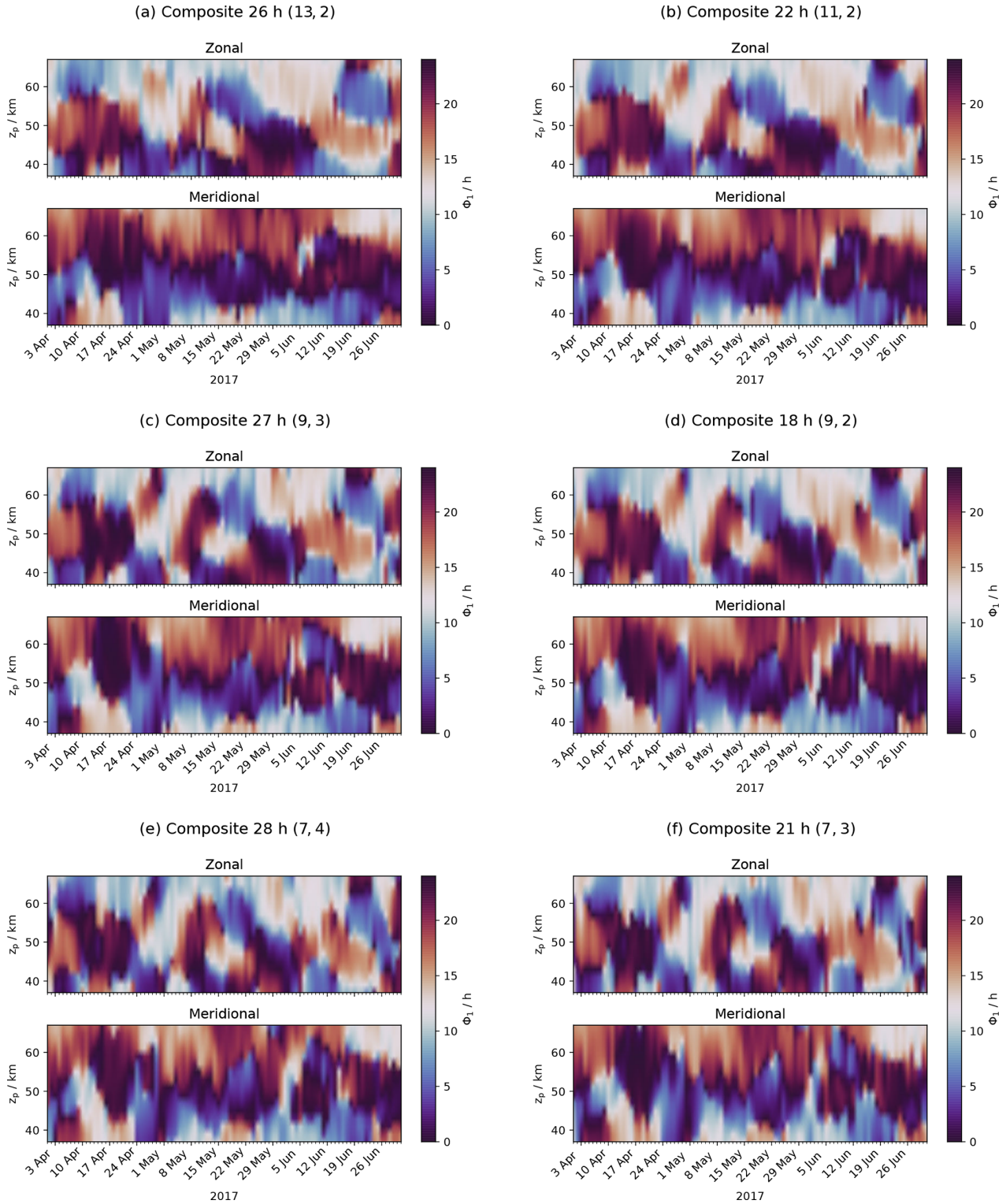

Figure A2. Tropical campaign: phase of the diurnal tide for six different composites with a similar total integration time of 21 to 28 h ordered by window length.

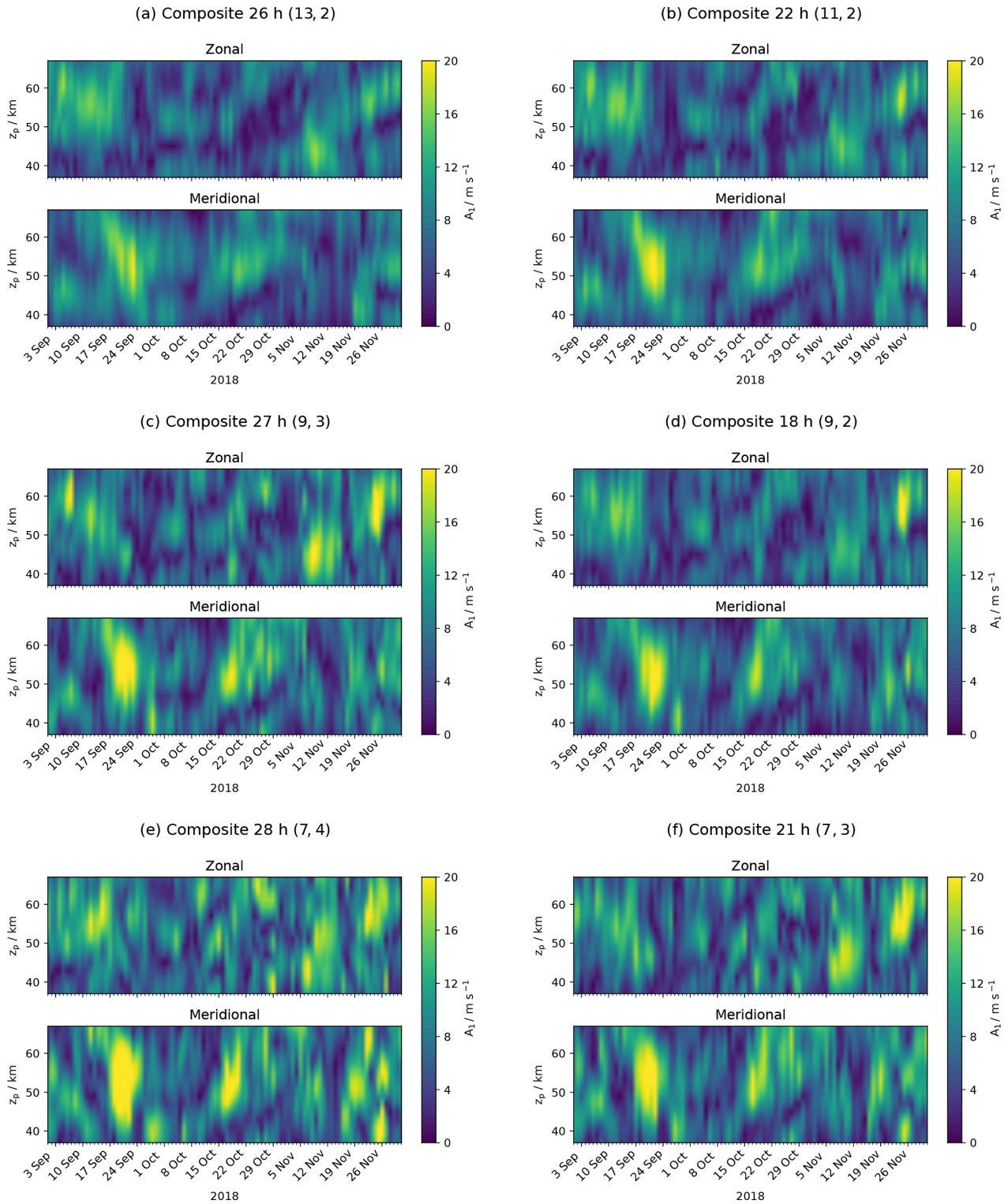

Figure A3. Arctic campaign: amplitude of the diurnal tide for six different composites with a similar total integration time of 21 to 28 h ordered by window length.

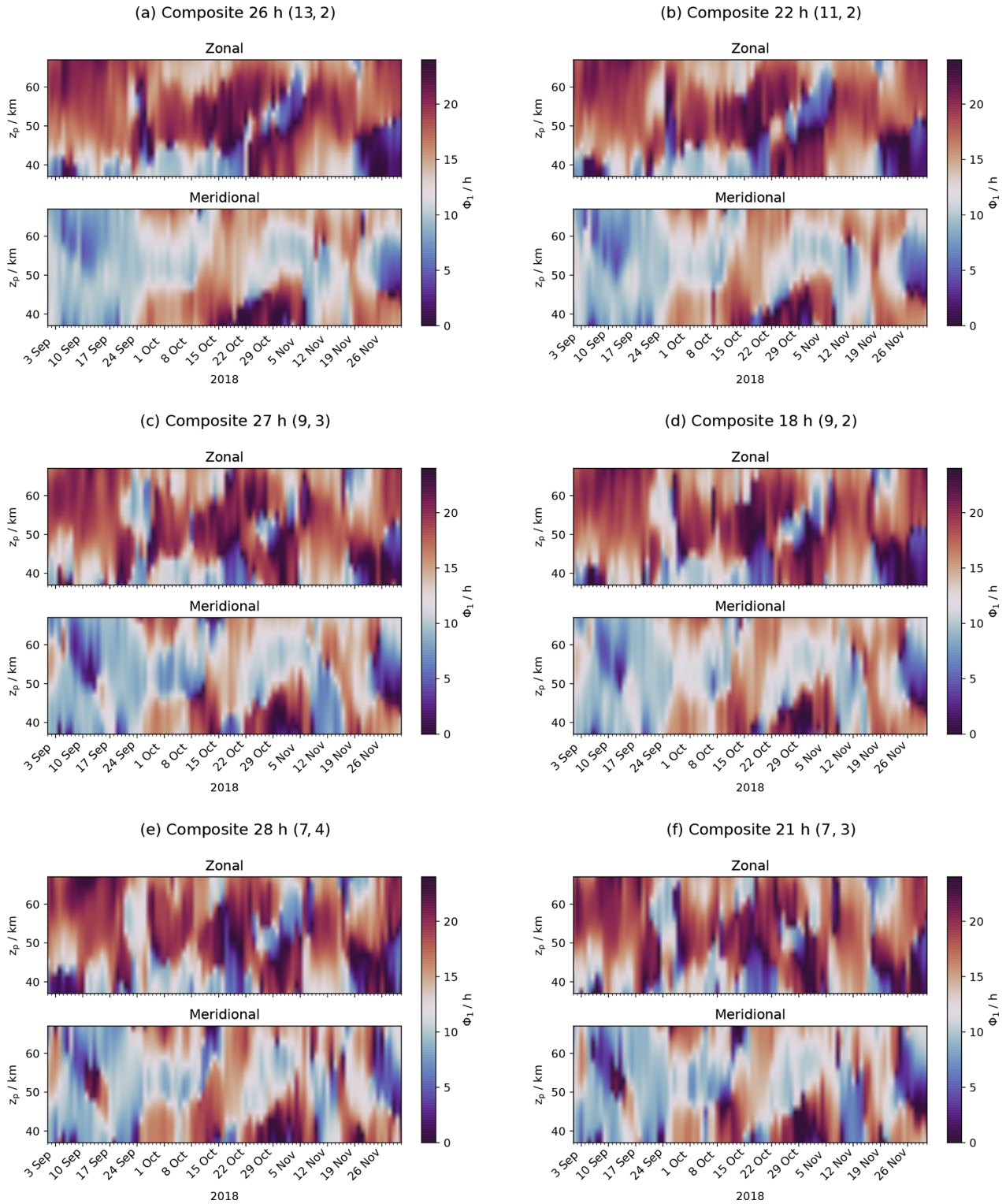

Figure A4. Arctic campaign: phase of the diurnal tide for six different composites with a similar total integration time of 21 to 28 h ordered by window length.

Data availability. The retrieved wind fields (WIRA-C level 2 data) for the two 3-month periods are available from the Zenodo public repository (https://doi.org/10.5281/zenodo.3468900, Hagen, 2019).

Author contributions. JH performed the data analysis and wrote the paper. KH and GS helped to interpret the results and contributed to the writing. SP contributes to the ARTS software package and worked on retrieval code. AM contributed to the development of the instrument and helped to discuss the method and the results. NK is PI of the project.

Competing interests. The authors declare that they have no conflict of interest.

Acknowledgements. The authors thank the staff of the ALOMAR observatory on Andøya, Norway, and the colleagues from the IAP Kühlungsborn, Germany, for their support and help during the campaign. The authors acknowledge the European Communities, the Région Réunion, CNRS and Université de La Réunion for their support and contributions in the construction phase of the research infrastructure OPAR (Observatoire de Physique de l'Atmosphère de La Réunion). OPAR is presently funded by CNRS (INSU), Météo-France and Université de La Réunion, and it is managed by OSU-R (Observatoire des Sciences de l'Univers de La Réunion, UMS 3365). The authors acknowledge the European Centre for Medium-Range Weather Forecasts (ECMWF) for the supplied data. Finally, the authors thank the two anonymous referees for their thorough review and very constructive comments.

Financial support. This research has been supported by the Schweizerischer Nationalfonds zur Förderung der Wissenschaftlichen Forschung (grant no. 200020-160048), the Staatssekretariat für Bildung, Forschung und Innovation (grant no. 15.0262/REF-113./52107), and Horizon 2020 (grant no. ARISE2 (653980)).

Review statement. This paper was edited by Farahnaz Khosrawi and reviewed by two anonymous referees.

References

Baray, J.-L., Courcoux, Y., Keckhut, P., Portafaix, T., Tulet, P., Cammas, J.-P., Hauchecorne, A., Godin Beekmann, S., De Mazière, M., Hermans, C., Desmet, F., Sellegri, K., Colomb, A., Ramonet, M., Sciare, J., Vuillemin, C., Hoareau, C., Dionisi, D., Duflot, V., Vérèmes, H., Porteneuve, J., Gabarrot, F., Gaudo, T., Metzger, J.-M., Payen, G., Leclair de Bellevue, J., Barthe, C., Posny, F., Ricaud, P., Abchiche, A., and Delmas, R.: Maïdo observatory: a new high-altitude station facility at Reunion Island (21° S, 55° E) for long-term atmospheric remote sensing and in situ measurements, Atmos. Meas. Tech., 6, 2865–2877, https://doi.org/10.5194/amt-6-2865-2013, 2013.

Baumgarten, G., Fiedler, J., Hildebrand, J., and Lübken, F.-J.: Inertia gravity wave in the stratosphere and mesosphere observed by Doppler wind and temperature lidar, Geophys. Res. Lett., 42, 10929–10936, https://doi.org/10.1002/2015GL066991, 2015.

Baumgarten, K. and Stober, G.: On the evaluation of the phase relation between temperature and wind tides based on ground-based measurements and reanalysis data in the middle atmosphere, Ann. Geophys., 37, 581–602, https://doi.org/10.5194/angeo-37-581-2019, 2019.

Buehler, S. A., Mendrok, J., Eriksson, P., Perrin, A., Larsson, R., and Lemke, O.: ARTS, the Atmospheric Radiative Transfer Simulator – version 2.2, the planetary toolbox edition, Geosci. Model Dev., 11, 1537–1556, https://doi.org/10.5194/gmd-11-1537-2018, 2018.

Forbes, J. M. and Wu, D.: Solar Tides as Revealed by Measurements of Mesosphere Temperature by the MLS Experiment on UARS, J. Atmos. Sci., 63, 1776–1797, https://doi.org/10.1175/JAS3724.1, 2006.

Global Modeling and Assimilation Office (GMAO): MERRA-2 inst3_3d_asm_Np: 3d, 3-Hourly, Instantaneous, Pressure-Level, Assimilation, Assimilated Meteorological Fields V5.12.4, Goddard Earth Sciences Data and Information Services Center (GES DISC), Greenbelt, MD, USA, https://doi.org/10.5067/QBZ6MG944HW0, 2015.

Hagan, M. E., Burrage, M. D., Forbes, J. M., Hackney, J., Randel, W. J., and Zhang, X.: GSWM-98: Results for Migrating Solar Tides, J. Geophys. Res., 104, 6813–6827, https://doi.org/10.1029/1998JA900125, 1999.

Hagen, J.: Wind fields from aggregated retrievals from the WIRA-C Doppler wind radiometer in tropical and arctic lattitudes (Version 1.0), Zenodo, https://doi.org/10.5281/zenodo.3468900, 2019.

Hagen, J., Murk, A., Rüfenacht, R., Khaykin, S., Hauchecorne, A., and Kämpfer, N.: WIRA-C: a compact 142-GHz-radiometer for continuous middle-atmospheric wind measurements, Atmos. Meas. Tech., 11, 5007–5024, https://doi.org/10.5194/amt-11-5007-2018, 2018.

Häusler, K., Lühr, H., Hagan, M. E., Maute, A., and Roble, R. G.: Comparison of CHAMP and TIME-GCM nonmigrating tidal signals in the thermospheric zonal wind, J. Geophys. Res.-Atmos., 115, D00I08, https://doi.org/10.1029/2009JD012394, 2010.

Jacobi, C.: 6 year mean prevailing winds and tides measured by VHF meteor radar over Collm (51.3° N, 13.0° E), structure and Dynamics of Mesosphere and Lower Thermosphere, J. Atmos. Sol.-Terr. Phy., 78, 8–18, https://doi.org/10.1016/j.jastp.2011.04.010, 2012.

Kopp, M., Gerding, M., Höffner, J., and Lübken, F.-J.: Tidal signatures in temperatures derived from daylight lidar soundings above Kühlungsborn (54° N, 12° E), layered Phenomena in the Mesopause Region, J. Atmos. Sol.-Terr. Phy., 127, 37–50, https://doi.org/10.1016/j.jastp.2014.09.002, 2015.

Lahiri, S.: Resampling Methods for Dependent Data, Springer Series in Statistics, Springer, 374 pp., 2003.

Lindzen, R. S.: Tides and Gravity Waves in the Upper Atmosphere, in: Mesospheric Models and Related Experiments, edited by: Fiocco, G., Springer Netherlands, Dordrecht, 25, 122–130, https://doi.org/10.1007/978-94-010-3114-1_8, 1971.

Lindzen, R. S. and Chapman, S.: Atmospheric Tides, Space Sci. Rev., 10, 3–188, https://doi.org/10.1007/BF00171584, 1969.

Liu, H.-L.: Variability and predictability of the space environment as related to lower atmosphere forcing, Space Weather, 14, 634–658, https://doi.org/10.1002/2016SW001450, 2016.

Liu, H.-L., Bardeen, C. G., Foster, B. T., Lauritzen, P., Liu, J., Lu, G., Marsh, D. R., Maute, A., McInerney, J. M., Pedatella, N. M., Qian, L., Richmond, A. D., Roble, R. G., Solomon, S. C., Vitt, F. M., and Wang, W.: Development and Validation of the Whole Atmosphere Community Climate Model With Thermosphere and Ionosphere Extension (WACCM-X 2.0), J. Adv. Model Earth Sy., 10, 381–402, https://doi.org/10.1002/2017MS001232, 2018.

McCormack, J., Hoppel, K., Kuhl, D., de Wit, R., Stober, G., Espy, P., Baker, N., Brown, P., Fritts, D., Jacobi, C., Janches, D., Mitchell, N., Ruston, B., Swadley, S., Viner, K., Whitcomb, T., and Hibbins, R.: Comparison of mesospheric winds from a high-altitude meteorological analysis system and meteor radar observations during the boreal winters of 2009–2010 and 2012–2013, J. Atmos. Sol.-Terr. Phy., 154, 132–166, https://doi.org/10.1016/j.jastp.2016.12.007, 2017.

McLandress, C., Shepherd, G. G., and Solheim, B. H.: Satellite Observations of Thermospheric Tides: Results from the Wind Imaging Interferometer on UARS, J. Geophys. Res.-Atmos., 101, 4093–4114, https://doi.org/10.1029/95JD03359, 1996.

Merzlyakov, E., Jacobi, C., Portnyagin, Y., and Solovjova, T.: Structural changes in trend parameters of the MLT winds based on wind measurements at Obninsk (55° N, 37° E) and Collm (52° N, 15° E), long-Term Changes and Trends in the Atmosphere-Ionosphere System, J. Atmos. Sol.-Terr. Phy., 71, 1547–1557, https://doi.org/10.1016/j.jastp.2009.05.013, 2009.

Oberheide, J., Forbes, J. M., Häusler, K., Wu, Q., and Bruinsma, S. L.: Tropospheric tides from 80 to 400 km: Propagation, interannual variability, and solar cycle effects, J. Geophys. Res.-Atmos., 114, D00I05, https://doi.org/10.1029/2009JD012388, 2009.

Oberheide, J., Forbes, J. M., Zhang, X., and Bruinsma, S. L.: Climatology of upward propagating diurnal and semidiurnal tides in the thermosphere, J. Geophys. Res., 116, A11306, https://doi.org/10.1029/2011JA016784, 2011.

Ortland, D. A.: Daily estimates of the migrating tide and zonal mean temperature in the mesosphere and lower thermosphere derived from SABER data, J. Geophys. Res.-Atmos., 122, 3754–3785, https://doi.org/10.1002/2016JD025573, 2017.

Pancheva, D. and Mukhtarov, P.: Atmospheric Tides and Planetary Waves: Recent Progress Based on SABER/TIMED Temperature Measurements (2002–2007), Springer Netherlands, Dordrecht, 19–56, https://doi.org/10.1007/978-94-007-0326-1_2, 2011.

Pancheva, D., Miyoshi, Y., Mukhtarov, P., Jin, H., Shinagawa, H., and Fujiwara, H.: Global response of the ionosphere to atmospheric tides forced from below: Comparison between COSMIC measurements and simulations by atmosphere-ionosphere coupled model GAIA, J. Geophys. Res., 117, A07319, https://doi.org/10.1029/2011JA017452, 2012.

Portnyagin, Y., Forbes, J., Fraser, G., Vlncent, R., Avery, S., Lysenko, I., and Makarov, N.: Dynamics of the Antarctic and Arctic mesosphere and lower thermosphere regions II, The semidiurnal tide, J. Atmos. Terr. Phys., 55, 843–855, https://doi.org/10.1016/0021-9169(93)90025-T, 1993.

Portnyagin, Y. I., Solovjova, T. V., Makarov, N. A., Merzlyakov, E. G., Manson, A. H., Meek, C. E., Hocking, W., Mitchell, N., Pancheva, D., Hoffmann, P., Singer, W., Murayama, Y., Igarashi, K., Forbes, J. M., Palo, S., Hall, C., and Nozawa, S.: Monthly mean climatology of the prevailing winds and tides in the Arctic mesosphere/lower thermosphere, Ann. Geophys., 22, 3395–3410, https://doi.org/10.5194/angeo-22-3395-2004, 2004.

Rodgers, C. D.: Inverse Methods for Atmospheric Sounding – Theory and Practice, 2, https://doi.org/10.1142/9789812813718, 256 pp., 2000.

Rogers, A. E., Erickson, P. J., Goncharenko, L. P., Alam, O. B., Noto, J., Kerr, R. B., and Kapali, S.: Seasonal and Local Solar Time Variation of the Meridional Wind at 95 km from Observations of the 11.072 GHz Ozone Line and the 557.7 Nm Oxygen Line, J. Atmos. Ocean. Tech., 33, 1355–1361, https://doi.org/10.1175/JTECH-D-15-0247.1, 2016.

Rüfenacht, R., Hocke, K., and Kämpfer, N.: First continuous ground-based observations of long period oscillations in the vertically resolved wind field of the stratosphere and mesosphere, Atmos. Chem. Phys., 16, 4915–4925, https://doi.org/10.5194/acp-16-4915-2016, 2016.

Rüfenacht, R., Baumgarten, G., Hildebrand, J., Schranz, F., Matthias, V., Stober, G., Lübken, F.-J., and Kämpfer, N.: Intercomparison of middle-atmospheric wind in observations and models, Atmos. Meas. Tech., 11, 1971–1987, https://doi.org/10.5194/amt-11-1971-2018, 2018.

Sakazaki, T., Fujiwara, M., Zhang, X., Hagan, M. E., and Forbes, J. M.: Diurnal Tides from the Troposphere to the Lower Mesosphere as Deduced from TIMED/SABER Satellite Data and Six Global Reanalysis Data Sets, J. Geophys. Res.-Atmos., 117, D13108, https://doi.org/10.1029/2011JD017117, 2012.

Sakazaki, T., Fujiwara, M., and Shiotani, M.: Representation of solar tides in the stratosphere and lower mesosphere in state-of-the-art reanalyses and in satellite observations, Atmos. Chem. Phys., 18, 1437–1456, https://doi.org/10.5194/acp-18-1437-2018, 2018.

Schanz, A., Hocke, K., and Kämpfer, N.: Daily ozone cycle in the stratosphere: global, regional and seasonal behaviour modelled with the Whole Atmosphere Community Climate Model, Atmos. Chem. Phys., 14, 7645–7663, https://doi.org/10.5194/acp-14-7645-2014, 2014.

Schranz, F., Hagen, J., Stober, G., Hocke, K., Murk, A., and Kämpfer, N.: Small-scale variability of stratospheric ozone during the SSW 2018/2019 observed at Ny-Ålesund, Svalbard, Atmos. Chem. Phys. Discuss., https://doi.org/10.5194/acp-2019-1093, in review, 2019.

Stober, G., Jacobi, C., Fröhlich, K., and Oberheide, J.: Meteor radar temperatures over Collm (51.3° N, 13° E), Adv. Space Res., 42, 1253–1258, https://doi.org/10.1016/j.asr.2007.10.018, 2008.

Stober, G., Matthias, V., Jacobi, C., Wilhelm, S., Höffner, J., and Chau, J. L.: Exceptionally strong summer-like zonal wind reversal in the upper mesosphere during winter 2015/16, Ann. Geophys., 35, 711–720, https://doi.org/10.5194/angeo-35-711-2017, 2017.

Wang, H., Boyd, J. P., and Akmaev, R. A.: On computation of Hough functions, Geosci. Model Dev., 9, 1477–1488, https://doi.org/10.5194/gmd-9-1477-2016, 2016.

Wilhelm, S., Stober, G., and Brown, P.: Climatologies and long-term changes in mesospheric wind and wave measurements based on radar observations at high and mid latitudes, Ann. Geophys., 37, 851–875, https://doi.org/10.5194/angeo-37-851-2019, 2019.

Woolnough, S. J., Slingo, J. M., and Hoskins, B. J.: The Diurnal Cycle of Convection and Atmospheric Tides in an Aquaplanet GCM, J. Atmos. Sci., 61, 2559–2573, https://doi.org/10.1175/JAS3290.1, 2004.

Yiğit, E., Knížová, P. K., Georgieva, K., and Ward, W.: A review of vertical coupling in the Atmosphere–Ionosphere system: Effects of waves, sudden stratospheric warmings, space weather, and of solar activity, J. Atmos. Sol.-Terr. Phy., 141, 1–12, https://doi.org/10.1016/j.jastp.2016.02.011, 2016.

7 Publication: Frequency-agile Fast Fourier Transform Spectrometer

Summary

Apart from the enhancement of data analyses techniques, also the technical part of radiometry has still room for improvement. This includes to take full advantage of technological progressions like software defined radio with its plethora of possibilities. The third publication explores such an application of software defined radio to passive microwave radiometry. The technique described is one of fast local oscillator switching for bandwidth enlargement by trading off integration time. Using current hardware, this can be done in a way that the trade-off can be adjusted for different parts of the spectrum, allowing to choose the optimal configuration of the spectrometer for wind and ozone applications. In this article, we evaluate the benefits of this configuration for ozone retrievals using the WIRA-C instrument.

This is relevant to the future development and adoption of microwave radiometry and is a contribution to the efforts towards a comprehensive atmospheric research infrastructure. Such a global network infrastructure would ideally include many multi-species (passive microwave) instruments to cover a large area and many species with observations.

Publication

The following article has been published in *Atmosphere*.

Citation: Jonas Hagen, Andres Luder, Axel Murk, and Niklaus Kämpfer. "Frequency-Agile FFT Spectrometer for Microwave Remote Sensing Applications". In: *Atmosphere* 11.5 (May 11, 2020), p. 490. ISSN: 2073-4433. DOI: 10.3390/atmos11050490

atmosphere

MDPI

Article

Frequency-Agile FFT Spectrometer for Microwave Remote Sensing Applications

Jonas Hagen *, Andres Luder, Axel Murk and Niklaus Kämpfer

Institute of Applied Physics, University of Bern, 3012 Bern, Switzerland; andres.luder@iap.unibe.ch (A.L.); axel.murk@iap.unibe.ch (A.M.); niklaus.kaempfer@iap.unibe.ch (N.K.)

* Correspondence: jonas.hagen@iap.unibe.ch

Received: 6 April 2020; Accepted: 6 May 2020; Published: 11 May 2020

Abstract: We report on a Fast Fourier Transform Spectrometer (FFTS) that provides larger bandwidth by fast local oscillator switching of the base-band converter. We demonstrate that this frequency scanning technique is suited for atmospheric remote sensing and conduct measurements of atmospheric ozone using the WIRA-C (WInd RAdiometer for Campaigns) Doppler wind radiometer. The comparison of our measurements to an adjusted atmospheric and instrumental model exposes no systematic biases due to the switching procedure in the measured spectra. It further shows that the combination of high spectral resolution with large bandwidth yields good measurement response to stratospheric and mesospheric ozone from approximately a 20 km to 70 km altitude with a resolution of 7 km in the lower stratosphere to 20 km in the mesosphere. We conclude that low-cost, low-power software-defined radio hardware designed for communications applications is very well suited for a variety of spectroscopic applications, including ozone monitoring. This allows the design of low-cost, multi-purpose instruments for atmospheric remote sensing and thus has a direct impact on future radiometer developments and their adoption in remote sensing campaigns and networks.

Keywords: radiometry; remote sensing; FFT spectrometry; ozone

1. Introduction

Spectrometers are used for the real-time observation of emission lines in remote sensing of the atmosphere and radio-astronomy. Fast Fourier Transform Spectrometers (FFTS) in particular are widely used in microwave remote sensing to observe the spectral distribution of thermal microwave emission of atmospheric trace gases. Compared to other spectrometer types, like optoacoustic spectrometers or filter-banks, FFTS offer a good compromise between bandwidth, spectral resolution, and stability [1,2]. An overview of different FFTS implementations and their performance characteristics was given by [3]. Lately, less expensive and more flexible radio peripherals became available as Software-Defined Radio (SDR), which not only allow the implementation of an FFTS, but also offer some flexibility in implementing further signal processing and acquisition schemes.

The WIRA-C (WInd RAdiometer for Campaigns) Doppler microwave wind radiometer [4] is a ground-based passive radiometer, which observes the ozone rotational emission line at 142.17504 GHz with a high spectral resolution of 12 kHz. It uses the Doppler shift of the emission line due to moving air to retrieve information about the horizontal wind speed in the stratosphere and lower mesosphere (approximately 30 to 70 km). The pressure broadening effect allows the retrieval of altitude-resolved wind profiles.

The spectrometer used in this instrument is a general purpose SDR that is available at a low cost and small form-factor and implements an FFTS. The trade-off is the relatively low bandwidth of 200 MHz, which is enough for wind observations in the stratosphere and lower mesosphere, but not for ozone observations in the lower stratosphere. Extending the bandwidth, while keeping the high

resolution at the line-center, would thus enable simultaneous ozone and wind measurements, among other novel applications.

Multi-purpose ground-based passive instruments that observe different species at the same time provide very valuable observations to understand the small scale variability and local behavior of dynamics and chemistry in the middle atmosphere. An instrument that observes multiple emission lines with a frequency switched double-side-band receiver has been shown to be valuable for simultaneous measurements of carbon monoxide and ozone [5]. In [6], the value of joint ozone and wind measurements was demonstrated at the arctic station in Ny-Ålesund, Svalbard, using the 110 GHz ozone emission line.

With this study, we present a method to extend the observation bandwidth of our spectrometer from 200 MHz to 1 GHz, which makes it possible to use our wind radiometer WIRA-C also for ozone measurements, and thus, we present a way to get additional scientific data out of our campaigns. We discuss the performance of our spectrometer configuration and its impact on retrievals of ozone. A cross-validation with other ozone instruments is not in the scope of this study. Instead, this study should motivate the inclusion of WIRA-C in future cross-validations.

2. Materials and Methods

2.1. Instrument and Spectrometer Configuration

The WIRA-C radiometer is a single-side-band heterodyne receiver, which uses a USRP (Universal Software Radio Peripheral) as a high resolution FFTS to measure the 142.17504 GHz rotational emission line of ozone with a high spectral resolution of 12 kHz over a bandwidth of 200 MHz. Figure 1 shows a schematic of the radiometer front-end and the back-end. The front-end consists of a 140 GHz Low Noise Amplifier (LNA), a single-side-band filter, and a sub-harmonic mixer that converts the Radio Frequency (RF) signal down to an Intermediate Frequency (IF) band centered at 3.65 GHz.

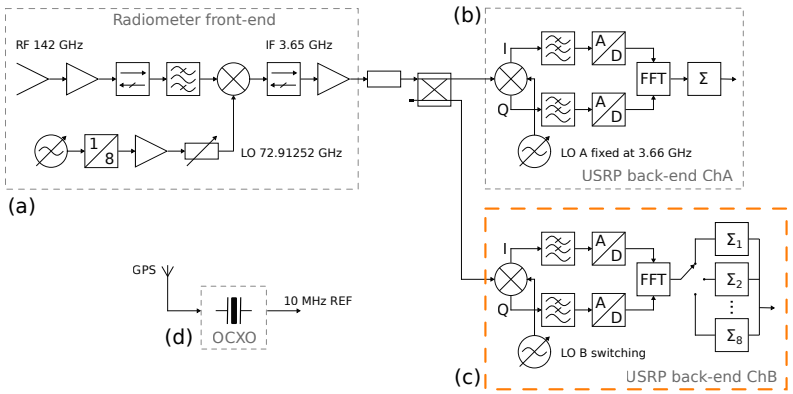

Figure 1. Schema of the WIRA-C radiometer front-end (**a**) and the back-end with spectrometer ChA (**b**) with fixed LO and changed ChB (**c**) with switching LO. All LO clocks are connected to the same GPS disciplined Oven Controlled Crystal Oscillator (OCXO) (**d**). IF, Intermediate Frequency.

The Universal Software Radio Peripheral (USRP X310 with two CBX-120 daughter-boards [7]) is used as the radiometer back-end; see Figure 1c,d. It has two independent channels (ChA and ChB), each of which embedds an In-phase and Quadrature (IQ) base-band converter and Analog-to-Digital Converters (ADCs) with a sampling rate of 200 MHz each. Due to the filter characteristics of the CBX-120 daughter-board input stage, only 160 MHz of the theoretically achievable 200 MHz are usable. We implement the FFT and accumulation on the internal Field-Programmable Gate Array (FPGA) using LabView-RT. After absolute-value-squared accumulation, the raw spectra are sent off to a general purpose computer for further processing. Both channels of the back-end are fed with the same IF signal, while ChA provides the high resolution spectrum for wind retrievals; we reconfigured ChB to

provide a wide spectrum with a total bandwidth of 1 GHz centered around the same region as ChA. An overview of the configuration is shown in Table 1.

Table 1. Overview of the channel configuration of the USRP used for this study. Both channels (ChA and ChB) are electrically equal, but ChB takes advantage of frequency scanning for larger Bandwidth (BW) at the cost of a lower total integration time.

	Technical BW	Usable BW	Resolution	Integration Time
ChA	200 MHz	160 MHz	12.2 kHz	10 s
ChB	8 × 200 MHz	1000 MHz	61.0 kHz	1.13 s

While both channels have the same ADC with a sampling rate of 200 MHz, we use fast Local Oscillator (LO) switching to scan a broader band with ChB. This method switches the LO frequency of the base band converter in ChB fast enough to cover multiple adjacent spectral regions. We chose a total of 8 different LO frequencies and take the central 125 MHz of each spectrum. The combination of the spectra is done so that we have a small overlap of a few channels between the different parts. Then, we average over 5 channels to reduce noise, which resulted in 2048 channels per LO frequency. The details (binning, overlap, and bandwidth) are chosen so that the combined spectrum has 16,384 ($=2^{14}$, same as ChA) channels and a 1 GHz bandwidth, which gives a channel resolution of 61 kHz.

In theory, the integration time for ChB is exactly 8 times less than for ChA. However, in practice, the re-locking of the base-band converter LO takes some time, during which we do not acquire any ADC values. The ratio between actual integration time for ChA and ChB is 8.88 for 10 seconds of integration, meaning that we loose 1 s or 10% of the integration time. In absolute numbers, this means that an LO reconfiguration takes approximately 140 ms. This applies only to the data presented in this study, and we were since able to reduce this to less than 1 ms by optimizing the LO reconfiguration procedure.

2.2. Data Processing

We calibrate our spectrometer with a tipping curve scheme. This calibration method uses the observations under different elevation angles to calculate the zenith opacity and thus the brightness temperature of the sky in the zenith direction. One calibration cycle takes 2 min, which is well within the time span for which the receiver can be assumed to be stable, as presented in [4]. Together with the internal hot-load, this allows a hot-cold calibration. Notably, each FFT channel of the spectrum is considered separately. We use the zenith measurement and our slanted observation at a 40° elevation angle in the north and southward directions. The general scheme of this calibration method is described in [8], and its implementation for WIRA-C is given in [4].

Then, we perform a tropospheric correction of the calibrated spectra by estimating the tropospheric contribution using the left wing of the measured ozone emission line [4,9]. Using this estimation, we remove the tropospheric contribution from our spectrum. To account fully for the tropospheric contribution, the slope of the continuum of the water-vapor line at 182 GHz would also have to be considered. We do not correct for this in the tropospheric correction step, but leave it for the retrieval to deal with the linear offset in terms of a baseline.

To characterize the quality of our concatenated spectrum, we compare the measurements to the Atmospheric Radiative Transfer Model (ARTS) [10]. Firstly, this lets us subtract the contribution from the ozone line from our measurements, and we can compute the statistics of the residuals for the different parts of the concatenated spectrum. Secondly, we can give a first estimate of the performance of our setup with regard to ozone retrievals.

The retrieval includes the adjustment of the ozone profile and a baseline (constant and linear) to fit our measurement. We use the Optimal Estimation Method (OEM) from ARTS for the inversion. The OEM uses an a priori estimation with corresponding co-variances to regularize the inversion problem [11]. The ozone retrieval is performed for 81 pressure levels, logarithmically distributed between 10^2 and 10^{-3} hPa. The ozone a priori data are the same as used in [4], namely the ozone

a priori data form the F2000 WACCM scenario from [12]. We impose a co-variance matrix with a diagonal of 1 ppm ozone VMR. The temperature data is taken from the ECMWF operational analysis, and we extend it with the F2000 WACCM data above 70 km altitude. The co-variance matrix of the spectrum is assumed to be diagonal (uncorrelated channels), and the variance is estimated by the Allan variance of the spectrum. We validate this estimation a posteriori against the variance of the residuals.

Once we have fitted the atmospheric model to our data, we compute the residuals and statistics for each block of the spectrum. We repeat the same evaluation method for different combinations of the spectra: (1) for the original spectrum from ChA, (2) for the concatenated spectrum from ChB, and (3) for a combination of data from ChA and ChB. For the combination of both channels, we take the spectrum from ChA and extend it with those parts from the broad-band ChB that are not covered by ChA itself.

In this study, we use data from the campaign in Bern that took place from March to May 2018. We selected this campaign because the data and methods used in this study might be of particular interest for the future validation of the GROMOS radiometer that is also located in Bern [13–15]. Specifically, we look at data for the night- and day-time of 7 May 2018 to 9 May 2018 and integrate over 12 h. For this measurement, the WIRA-C instrument was configured to look at a 40° elevation angle (same as GROMOS) instead of 22°, which is used for routine wind measurements. The WIRA-C instrument looks in four different cardinal directions (plus zenith) for wind measurements, but for this study, we only consider the northward measurement.

3. Results

Figure 2 shows a narrow spectrum (from ChA) and a wide spectrum (from ChB) colorized to give an impression of the concatenation process. The concatenation is done with a slight overlap, where one part blends into the next one. This is done for no specific reason, and we consider it to be an implementation detail with no bearing on the results. The spectra were acquired at nighttime 9 May 2018. The top panel of Figure 2 shows the ChA and ChB with a zoom on the line-center. Both channels show a matching brightness temperature. Note that from this figure, it is not clearly visible that ChA has less noise due to longer total integration time. We will later determine the noise from the residuals of a retrieval.

To quantify how well the spectra from the different channels match and also how well the spectra from the different parts of ChB match, we run a retrieval (and thus, fit an atmospheric model) on our data. As described above, we used three different spectra for our retrievals (ChA, ChB, and combined). The results from all these retrievals are shown in Figure 3, also for nighttime on 9 May 2018.

The increased bandwidth extends the sensitivity for ozone towards lower altitudes, whereas the high spectral resolution adds sensitivity in the mesosphere, as expected. For the combined retrieval, the measurement response is larger than 0.8 between approximately 21 km up to 70 km.

We also see an effect on the vertical resolution of the ozone profile, which is characterized by the Full Width at Half Maximum (FWHM) of the averaging kernels. For example, at an altitude of approximately 40 km, the averaging kernels from the retrievals from ChB have a FWHM of 14 km, which improves to 11 km when using the higher resolution of ChA. This difference is most notable at higher altitudes. Only below 30 km, the FWHM of the averaging kernels can profit from the wider bandwidth of ChB, which is able to capture more information from the pressure broadened emission line. This effect is caused by the better signal-to-noise ratio of the ChA measurement compared to that of ChB because of the longer integration time. The combined retrieval profits from the lower noise, as well as from the broader bandwidth at the lowest altitude levels. Another important measure of quality is the observation error. Here, the impact of the different spectral resolutions and noise are quite small, and the observational error is about 0.13 ppm for the whole altitude region covered.

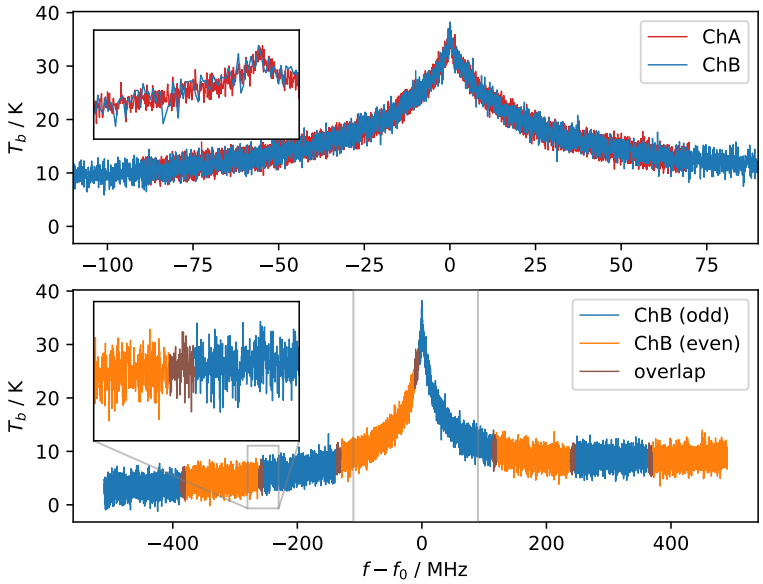

Figure 2. Spectra from the WIRA-C ChA (narrow) and WIRA-C ChB (wide) at an elevation angle of 40°. The bottom panel shows the different parts of the spectrum that were measured independently with alternating colors (odd/even). Frequencies are relative to the emission line center of ozone at $f_0 = 142.17504$ GHz.

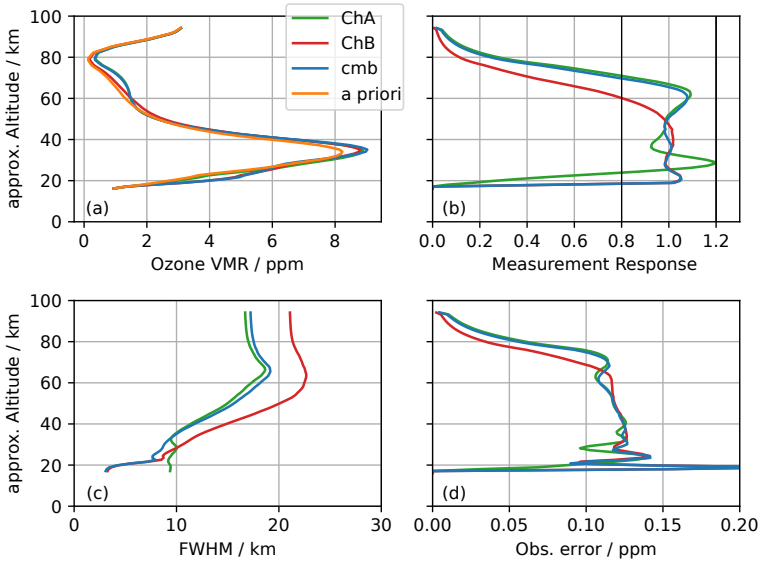

Figure 3. Ozone retrieval for three different spectra: ChA only, ChB only, and combined (cmb). Shown are the (**a**) ozone VMR, (**b**) the measurement response, (**c**) the full width at half maximum of the averaging kernels, and (**d**) the estimated observational error.

In general, the wider bandwidth only brings an improvement at or below approximately 30 km altitude. However, we would like to note that off-resonance measurements (that is, measurements at the line-wing) are important also for tropospheric correction and can be valuable for baseline correction.

Figure 4a shows the fitted spectrum together with the measurement and the baseline for the combined retrieval. There is a small slope visible in the baseline of approximately 3 K per GHz, which comes from the slope of the 182 GHz emission line of tropospheric water vapor that we did not correct for during tropospheric correction. Figure 4b shows the residuals (observed-minus-computed) of the

combined retrieval. There is no obvious baseline visible, and the transition from the broad spectrum to the high resolution one appears to be smooth.

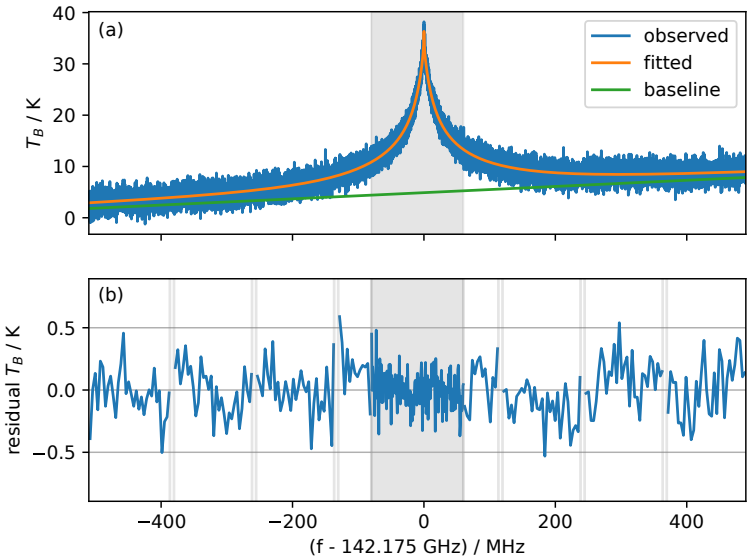

Figure 4. Measured and fitted spectrum for the combined (ChA and ChB) retrieval together with the baseline estimation (**a**). Residuals (**b**) are binned (64 FFTS channels), for each part separately. The spectral region from ChA is indicated by the gray area, and vertical gray lines indicate the boundaries of individual sub-spectra.

The residuals do not expose significant steps between the sub-spectra and are reasonably normally distributed as shown in Figure 5. Statistical evaluation shows no systematic dependency of residuals correlated with their origin (ChA or sub-spectra of ChB; no figure shown). The residuals of ChA have a standard deviation of 1.05 K, which is 1.31 times lower than the standard deviation of ChB residuals, which is 1.38 K. According to the radiometer formula, the relative noise between the two channels would be:

$$r_\sigma = \frac{\sigma_A}{\sigma_B} = \sqrt{\frac{\tau_A B_A}{\tau_B B_B}} = \sqrt{\frac{8.88 \times 1}{1 \times 5}} = 1.33 \quad (1)$$

which is very close to the observed value of 1.31.

Figure 6 shows the residuals of retrievals from ChB spectra for three days separated by daytime and nighttime (in total, six measurements). The distribution of the residuals is wider for days with a higher tropospheric opacity, because high humidity decreases the signal-to-noise ratio for the stratospheric signal. Some residuals expose a small step between the sub-spectra, for example on 8 May 2018 (day- and night-time) of about 0.2 K between Sub-spectra 7 and 8. Since the residuals can be assumed to be distributed with a standard deviation of $\sigma \approx 1.3$ K, we expect the difference between two channels to be smaller than $2\sigma \approx 2.6$ K in 66% of the cases. For the binned values shown in Figure 5, the expectation is that the difference between the two channels is smaller than 0.325 K in approximately 66% of the cases. For a future study on ozone retrievals with WIRA-C using the described spectrometer configuration, we thus recommend considering the possible steps between the sub-spectra of ChB in the quality control of the ozone retrieval. For example, one could consider measurements where the edges of the binned sub-spectra are more than 0.3 K apart for more than four of the seven boundaries to be invalid. The exact numbers would depend on the binning and distribution of residuals. In any case, the assumption of normally distributed residuals has to be checked first.

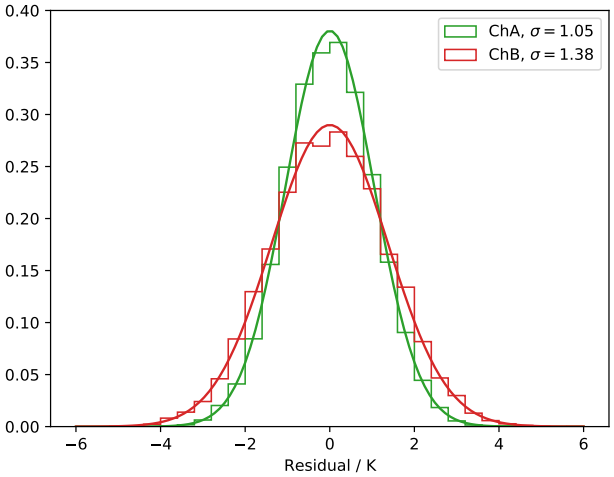

Figure 5. Histogram of the residuals for the different spectra (ChA only, ChB only, and combined) with the normal distribution corresponding to the data mean and standard deviation. Vertical gray lines indicate boundaries of individual sub-spectra. Measurements are annotated with tropospheric opacity τ.

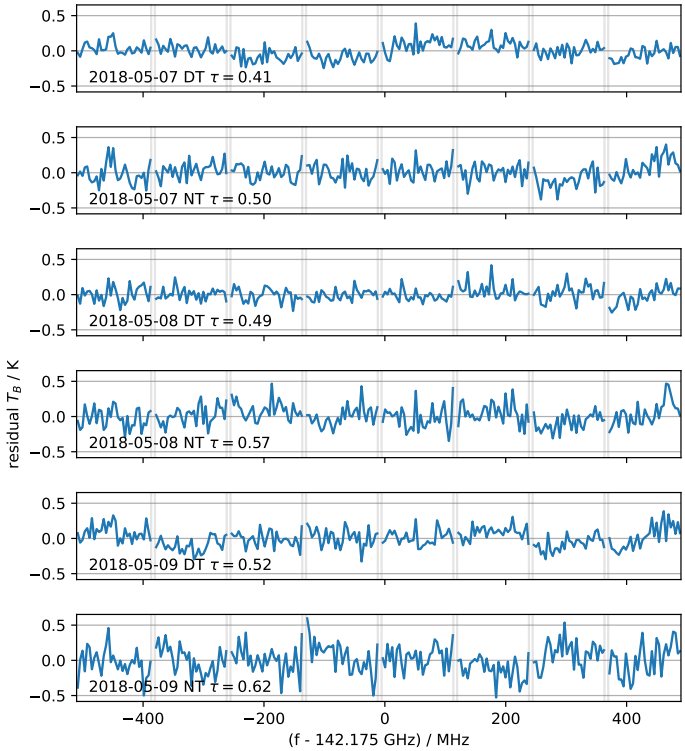

Figure 6. Residuals from six measurements taken during three days, daytime (DT) and nighttime (NT) obtained from the retrieval of ChB only. Residuals are binned (64 FFTS channels) for each part separately.

4. Outlook and Conclusions

We presented a method to measure broad-band spectra using off-the-shelf communications radio peripherals and demonstrated its use for radiometric observations of the atmosphere. While the method of fast LO switching itself is used in other applications, it is new to atmospheric remote sensing.

The LO switching reduced the integration time, and thus, the combination of a concatenated spectrum with a high resolution spectrum at the line-center was especially useful. At the line-wings, a larger bandwidth is preferred over high spectral resolution for ozone retrievals. This setup demonstrates how multi-purpose instruments can be built using off-the-shelf radio communications peripherals using SDR techniques.

We suggest a specific method to control the quality of the concatenated spectrum by rejecting measurements, where the binned values at the edges between the sub-spectra are off by more than 2σ at four or more of the seven edges (or equivalent).

An estimation of the retrieval quality showed that ozone retrievals could benefit from the broad spectrum, especially if the high resolution spectrum were combined with the broad-band spectrum at the line-center. In this specific case, we observed an improved vertical resolution of 11 km for the combined spectra over 14 km for the broad-band spectra, while keeping the measurement response larger than 0.8 down to 20 km (compared to 25 to 30 km for the high resolution spectrum from ChA only). While effective numbers are only valid for the presented case, the improvement is the result of the combination of the high resolution spectrum (used at the line-center) with the broad-band spectrum.

While the same hardware has already been used for operational wind measurements, this new method improves the capability to retrieve ozone profiles from the WIRA-C instrument. Since wind radiometers observe all four cardinal directions (north, south, east, west), they are also well suited to observe the spatial ozone distribution and gradients on a small scale. Together with wind observations, this facilitates gaining further insight into atmospheric dynamics and chemistry on small scales.

Author Contributions: Conceptualization, A.L. and A.M.; implementation/software A.L. and J.H.; investigation J.H. and A.M.; writing, original draft preparation, J.H.; writing, review and editing, J.H., A.M., and N.K.; supervision, N.K. and A.M. All authors read and agreed to the published version of the manuscript.

Funding: This research was supported by the Schweizerischer Nationalfonds zur Förderung der Wissenschaftlichen Forschung (Grant No. 200020-160048), the Staatssekretariat für Bildung, Forschung und Innovation (Grant No. 15.0262/REF-113./52107), and Horizon 2020 (Grant No. ARISE2 (653980)).

Acknowledgments: We acknowledge the effort of all technicians who contributed to this work or instruments used for this work, namely Nik Jaussi, Daniel Weber, and Adrian Jenk.

Conflicts of Interest: The authors declare no conflict of interest. The funders and the vendors of equipment and software had no role in the design of the study; in the collection, analyses, or interpretation of data; in the writing of the manuscript; nor in the decision to publish the results.

Abbreviations

The following abbreviations are used in this manuscript (in alphabetical order):

ADC	Analog-to-Digital Converter
ARTS	Atmospheric Radiative Transfer Simulator
BW	Bandwidth
ECMWF	European Centre for Medium-Range Weather Forecasts
FFT	Fast Fourier Transformation
FFTS	Fast Fourier Transform Spectrometer
FPGA	Field Programmable Gate Array
FWHM	Full Width at Half Maximum
GROMOS	Ground-based Remote Ozone Monitoring and Observation System
IQ	In-phase and Quadrature (converter)
LNA	Low Noise Amplifier
LO	Local Oscillator
OEM	Optimal Estimation Method
SDR	Software-Defined Radio
USRP	Universal Software Radio Peripheral
VMR	Volume Mixing Ratio
WACCM	Whole Atmosphere Community Climate Model
WIRA-C	WInd RAdiometer for Campaigns

References

1. Müller, S.C.; Murk, A.; Monstein, C.; Kämpfer, N. Intercomparison of Digital Fast Fourier Transform and Acoustooptical Spectrometers for Microwave Radiometry of the Atmosphere. *IEEE Trans. Geosci. Remote Sens.* **2009**, *47*, 2233–2239. [CrossRef]
2. Benz, A.O.; Grigis, P.C.; Hungerbühler, V.; Meyer, H.; Monstein, C.; Stuber, B.; Zardet, D. A broadband FFT spectrometer for radio and millimeter astronomy. *Astron. Astrophys.* **2005**, *442*, 767–773.:20053568. [CrossRef]
3. Murk, A.; Kotiranta, M. Characterization of Digital Real-Time Spectrometers for Radio Astronomy and Atmospheric Remote Sensing. In Proceedings of the International Symposium on Space THz Technology, Gothenburg, Sweden, 15 April 2019.
4. Hagen, J.; Murk, A.; Rüfenacht, R.; Khaykin, S.; Hauchecorne, A.; Kämpfer, N. WIRA-C: A Compact 142-GHz-Radiometer for Continuous Middle-Atmospheric Wind Measurements. *Atmos. Meas. Tech. Dis.* **2018**, 1–30. [CrossRef]
5. Forkman, P.; Christensen, O.M.; Eriksson, P.; Billade, B.; Vassilev, V.; Shulga, V.M. A compact receiver system for simultaneous measurements of mesospheric CO and O3. *Geosci. Instrum. Methods Data Syst.* **2016**, *5*, 27–44. [CrossRef]
6. Schranz, F.; Hagen, J.; Stober, G.; Hocke, K.; Murk, A.; Kämpfer, N. Small-scale variability of stratospheric ozone during the SSW 2018/2019 observed at Ny-Ålesund, Svalbard. *Atmos. Chem. Phys. Discuss.* **2019**, *2019*, 1–25. [CrossRef]
7. Ettus Research. USRP X310 High Performance Software Defined Radio (SDR)—Ettus Research. 2018. Available online: https://www.ettus.com/ (accessed on 7 January 2020).
8. Han, Y.; Westwater, E.R. Analysis and Improvement of Tipping Calibration for Ground-Based Microwave Radiometers. *IEEE Trans. Geosci. Remote Sens.* **2000**, *38*, 1260–1276. [CrossRef]
9. Fernandez, S.; Murk, A.; Kämpfer, N. GROMOS-C, a novel ground-based microwave radiometer for ozone measurement campaigns. *Atmos. Meas. Tech.* **2015**, *8*, 2649–2662. [CrossRef]
10. Buehler, S.A.; Mendrok, J.; Eriksson, P.; Perrin, A.; Larsson, R.; Lemke, O. ARTS, the Atmospheric Radiative Transfer Simulator—Version 2.2, the planetary toolbox edition. *Geosci. Model Dev.* **2018**, *11*, 1537–1556. [CrossRef]
11. Rodgers, C.D. *Inverse Methods for Atmospheric Sounding—Theory and Practice*; World Scientific: Singapore, 2000; Volume 2. [CrossRef]
12. Schanz, A.; Hocke, K.; Kämpfer, N. Daily Ozone Cycle in the Stratosphere: Global, Regional and Seasonal Behaviour Modelled with the Whole Atmosphere Community Climate Model. *Atmos. Chem. Phys.* **2014**, *14*, 7645–7663. [CrossRef]
13. Kämpfer, N. Microwave remote sensing of the atmosphere in Switzerland. *Opt. Eng.* **1995**, *34*, 2413–2424. [CrossRef]
14. Peter, R. *The Ground-Based Millimeter-Wave Ozone Spectrometer—GROMOS*; Research Report no. 97-13; Institute of Applied Physics, University of Bern: Bern, Switzerland, 1997.
15. Moreira, L.; Hocke, K.; Eckert, E.; Von Clarmann, T.; Kämpfer, N. Trend analysis of the 20-year time series of stratospheric ozone profiles observed by the GROMOS microwave radiometer at Bern. *Atmos. Chem. Phys.* **2015**, *15*, 10999–11009. [CrossRef]

8 Conclusions and Outlook

This thesis presents three scientific studies of which each represents a significant progress in middle-atmospheric wind radiometry. Firstly, it has been shown that Doppler microwave wind radiometry as established by WIRA can be reproduced. This has been one of the goals for WIRA-C within the ARISE2 project. It has been shown that the WIRA-C wind radiometer is capable to perform continuous observations of middle-atmospheric horizontal wind speeds with a vertical resolution of 12 km, a temporal resolution of 12 to 24 hours and an uncertainty of around 10 ms^{-1}. The models and observations do generally agree and represent the same local manifestations of global scale features such as planetary waves, their braking, sudden stratospheric warmings and bi-annual wind reversals.

Secondly, it has been shown that the wind radiometer technology in its current state, that is using a un-cooled, pre-amplified single-side-band heterodyne receiver is capable to also resolve the diurnal tide in the wind field. By using composite retrievals which average over at least 7 days, it is possible to reach a temporal resolution of 2 hours. This enables the observation of diurnal tides. Thanks to the inherent advantages of passive microwave radiometry such as long-term stability, independence of daylight and clouds and easy deployment this makes the observation of middle-atmospheric tides possible over an extended period of time. Averaged observations over three months do compare well to the reanalysis data and show the same features of the diurnal tide.

A recent topic in middle-atmospheric research is the tidal variability in the middle-atmosphere. There exists evidence that the variability of the tidal phase in the middle-atmosphere is larger than predicted by models (see references in Hagen et al., 2020a, particularly Baumgarten and Stober, 2019). With the possibility to use composite retrievals on different timescales, it might be possible for passive microwave wind radiometry to contribute to this field of active research. First results from WIRA-C measurements show indeed a higher variability than expected from the models, even tough more independent measurements are needed to confirm that this variability is indeed of purely atmospheric origin. Further research on the topic of tidal variability in the middle atmosphere is certainly required.

Since tides in the wind and temperature field are tightly coupled (with the details of this coupling being debated) it is of high interest to combine temperature and wind measurements in the middle-atmosphere to further explore these relations. Passive microwave radiometry is capable to deliver wind measurements and also temperature measurements for such studies. A campaign with passive microwave radiometers which measure the diurnal cycle of temperature and wind in the stratosphere are feasible and promise a high scientific value.

Wind acts by transport on all the other atmospheric species and waves in the wind field are a driver for local small-scale variability of these species, for example ozone. Thus the observation of the small scale variability of ozone together with the observation of wind gives further insight to middle-atmospheric dynamics, as has been shown by Schranz et al., 2019b. WIRA-C is in principle capable to perform such observations by leveraging the capabilities of software defined radio (SDR) to extend the bandwidth for ozone observations. Future studies could take advantage of this capability to further characterize the coupling of ozone chemistry and oscillations in the wind filed, particularly in highly dynamic environments such as in the context of sudden stratospheric warmings.

In summary, the following could be topics of future research with the WIRA-C wind radiometer:

- Continue observation of middle atmospheric wind at different latitudes
- Compare WIRA-C wind profiles from Andøya to ALOMAR lidar measurements
- Further compare the wind measurements to different models and reanalysis
- Combine temperature and wind radiometry to measure the phase relation of tidal fields
- Compare measurements of the diurnal tide to models in the context of sudden stratospheric warmings (expecting enhancement of diurnal tide)
- Retrieve Ozone profiles from WIRA-C and WIRA data, cross-compare with e.g. GROMOS

Bibliography

Alexander, M. J. et al. "Recent Developments in Gravity-Wave Effects in Climate Models and the Global Distribution of Gravity-Wave Momentum Flux from Observations and Models". In: *Quarterly Journal of the Royal Meteorological Society* (July 20, 2010), n/a–n/a. ISSN: 00359009, 1477870X. DOI: 10.1002/qj.637.

Baldwin, Mark P et al. "Stratospheric Memory and Skill of Extended-Range Weather Forecasts." In: *Science (New York, N.Y.)* 301 (August 2003). _eprint: 12893941 _eprinttype: pmid, pp. 636–640. ISSN: 0036-8075. DOI: 10.1126/science.1087143.

Baron, P. et al. "Observation of Horizontal Winds in the Middle-Atmosphere between 30 S and 55 N during the Northern Winter 2009-2010". In: *Atmospheric Chemistry and Physics* 13.12 (2013), pp. 6049–6064. ISSN: 16807316. DOI: 10.5194/acp-13-6049-2013.

Baron, P. et al. "Performance Assessment of Superconducting Submillimeter-Wave Limb-Emission Sounder-2 (SMILES-2)". In: *IGARSS 2019 - 2019 IEEE International Geoscience and Remote Sensing Symposium*. IGARSS 2019 - 2019 IEEE International Geoscience and Remote Sensing Symposium. Yokohama, Japan: IEEE, July 2019, pp. 7556–7559. ISBN: 978-1-5386-9154-0. DOI: 10.1109/IGARSS.2019.8898496.

Baumgarten, G. "Doppler Rayleigh/Mie/Raman Lidar for Wind and Temperature Measurements in the Middle Atmosphere up to 80 Km". In: *Atmospheric Measurement Techniques* 3.6 (2010), pp. 1509–1518. DOI: 10.5194/amt-3-1509-2010.

Baumgarten, Kathrin and Gunter Stober. "On the Evaluation of the Phase Relation between Temperature and Wind Tides Based on Ground-Based Measurements and Reanalysis Data in the Middle Atmosphere". In: *Annales Geophysicae* 37.4 (July 18, 2019), pp. 581–602. ISSN: 1432-0576. DOI: 10.5194/angeo-37-581-2019.

Bernet, Leonie et al. "Ground-Based Ozone Profiles over Central Europe: Incorporating Anomalous Observations into the Analysis of Stratospheric Ozone Trends". In: *Atmospheric Chemistry and Physics* 19.7 (Apr. 3, 2019), pp. 4289–4309. ISSN: 1680-7316. DOI: https://doi.org/10.5194/acp-19-4289-2019.

Blanc, E. et al. "Toward an Improved Representation of Middle Atmospheric Dynamics Thanks to the ARISE Project". In: *Surveys in Geophysics* 39.2 (Mar. 2018), pp. 171–225. ISSN: 0169-3298, 1573-0956. DOI: 10.1007/s10712-017-9444-0.

Blanc, Elisabeth et al. "Middle Atmosphere Variability and Model Uncertainties as Investigated in the Framework of the ARISE Project". In: *Infrasound Monitoring for Atmospheric Studies*. Ed. by Alexis Le Pichon, Elisabeth Blanc, and Alain Hauchecorne. Cham: Springer International Publishing, 2019, pp. 845–887. ISBN: 978-3-319-75138-2 978-3-319-75140-5. DOI: 10.1007/978-3-319-75140-5_28.

Buehler, S. A. et al. "ARTS, the Atmospheric Radiative Transfer Simulator – Version 2.2, the Planetary Toolbox Edition". In: *Geoscientific Model Development* 11.4 (2018), pp. 1537–1556. DOI: 10.5194/gmd-11-1537-2018.

Burrows, S. M., C. L. Martin, and E. A. Roberts. "High-Latitude Remote Sensing of Mesospheric Wind Speeds and Carbon Monoxide". In: *Journal of Geophysical Research: Atmospheres* 112.D17 (2007). ISSN: 2156-2202. DOI: 10.1029/2006JD007993.

Chalmers, University of Technology. *New Swedish Satellite to Map Unstudied Winds High up in Earth's Atmosphere*. 2018. URL: https://www.chalmers.se/en/departments/see/news/Pages/New-Swedish-satellite-to-map-unstudied-winds.aspx (visited on 05/18/2020).

Charlton, Andrew James et al. "Sensitivity of Tropospheric Forecasts to Stratospheric Initial Conditions". In: (2004), pp. 1771–1792. ISSN: 00359009. DOI: 10.1256/qj.03.167.

Clancy, Todd and Duane Muhleman. "Ground-Based Microwave Spectroscopy of the Earth's Stratosphere and Mesosphere". In: Janssen, Michael A. *Atmospheric Remote Sensing by Microwave Radiometry*. Wiley Series in Remote Sensing. New York: Wiley, 1993. ISBN: 978-0-471-62891-0.

Coumou, D. et al. "Quasi-Resonant Circulation Regimes and Hemispheric Synchronization of Extreme Weather in Boreal Summer". In: *Proceedings of the National Academy of Sciences* 111.34 (2014), pp. 12331–12336. ISSN: 0027-8424, 1091-6490. DOI: 10.1073/pnas.1412797111.

Dunkerton, T, CP F Hsu, and ME McIntyre. "Some Eulerian and Lagrangian Diagnostics for a Model Stratospheric Warming". In: *Journal of the Atmospheric Sciences* 38.4 (1981), pp. 819–844. ISSN: 1520-0469.

Flury, T. et al. "First Measurements of Lower Mesospheric Wind by Airborne Microwave Radiometry". In: *Geophysical Research Letters* 35.19 (Oct. 2, 2008), p. L19802. ISSN: 0094-8276. DOI: 10.1029/2008GL034663.

Forbes, J. M. et al. "Tidal Variability in the Ionospheric Dynamo Region". In: *Journal of Geophysical Research: Space Physics* 113.A2 (2008). ISSN: 2156-2202. DOI: 10.1029/2007JA012737.

Forbes, Jeffrey M. and Joseph E. Salah. "Mesosphere- Thermosphere Tidal Coupling during the September 21-25, 1987, LTCS 1 Campaign". In: *Journal of Geophysical Research: Space Physics* 96.A2 (Feb. 1, 1991), pp. 1135–1145. ISSN: 01480227. DOI: 10.1029/90JA01768.

Gelaro, Ronald et al. "The Modern-Era Retrospective Analysis for Research and Applications, Version 2 (MERRA-2)". In: *Journal of Climate* 30.14 (July 2017), pp. 5419–5454. ISSN: 0894-8755, 1520-0442. DOI: 10.1175/JCLI-D-16-0758.1.

Hagan, M. E. et al. "GSWM-98: Results for Migrating Solar Tides". In: *Journal of Geophysical Research: Space Physics* 104.A4 (Apr. 1999), pp. 6813–6827. ISSN: 01480227. DOI: 10.1029/1998JA900125.

Hagen, Jonas et al. "First Measurements of Tides in the Stratosphere and Lower Mesosphere by Ground-Based Doppler Microwave Wind Radiometry". In: *Atmospheric Chemistry and Physics* 20.4 (Feb. 28, 2020), pp. 2367–2386. ISSN: 1680-7324. DOI: 10.5194/acp-20-2367-2020.

Hagen, Jonas et al. "Frequency-Agile FFT Spectrometer for Microwave Remote Sensing Applications". In: *Atmosphere* 11.5 (May 11, 2020), p. 490. ISSN: 2073-4433. DOI: 10.3390/atmos11050490.

Hagen, Jonas et al. "WIRA-C: A Compact 142-GHz-Radiometer for Continuous Middle-Atmospheric Wind Measurements". In: *Atmospheric Measurement Techniques* 11.9 (Sept. 4, 2018), pp. 5007–5024. ISSN: 1867-8548. DOI: 10.5194/amt-11-5007-2018.

Han, Yong and E. R. Westwater. "Analysis and Improvement of Tipping Calibration for Ground-Based Microwave Radiometers". In: *IEEE Transactions on Geoscience and Re-*

mote Sensing 38.3 (May 2000), pp. 1260–1276. ISSN: 0196-2892. DOI: 10.1109/36.843018.

Hocke, Klemens et al. "Atmospheric Inertia-Gravity Waves Retrieved from Level-2 Data of the Satellite Microwave Limb Sounder Aura/MLS". In: *Annales Geophysicae* 34.9 (Sept. 19, 2016), pp. 781–788. ISSN: 1432-0576. DOI: 10.5194/angeo-34-781-2016.

Hocke, Klemens et al. "Diurnal Cycle of Short-Term Fluctuations of Integrated Water Vapour above Switzerland". In: *Atmospheric Chemistry and Physics* 19.19 (Sept. 30, 2019), pp. 12083–12090. ISSN: 1680-7324. DOI: 10.5194/acp-19-12083-2019.

Ingold, T., R. Peter, and N. Kämpfer. "Weighted Mean Tropospheric Temperature and Transmittance Determination at Millimeter-Wave Frequencies for Ground-Based Applications". In: *Radio Science* 33.4 (July 1998), pp. 905–918. ISSN: 1944-799X. DOI: 10.1029/98RS01000.

Khaykin, S M et al. "Ground-Based Rayleigh-Mie Doppler Lidar for Wind Measurements in the Middle Atmosphere". In: *EPJ Web of Conferences* 119 (June 2016). Ed. by B. Gross, F. Moshary, and M. Arend, p. 13005. DOI: 10.1051/epjconf/201611913005.

Kim, Young-Joon, Stephen D. Eckermann, and Hye-Yeong Chun. "An Overview of the Past, Present and Future of Gravity-wave Drag Parametrization for Numerical Climate and Weather Prediction Models". In: *Atmosphere-Ocean* 41.1 (Mar. 2003), pp. 65–98. ISSN: 0705-5900, 1480-9214. DOI: 10.3137/ao.410105.

Leuther, A. et al. "450 GHz Amplifier MMIC in 50 Nm Metamorphic HEMT Technology". In: *2012 International Conference on Indium Phosphide and Related Materials*. Aug. 2012, pp. 229–232. DOI: 10.1109/ICIPRM.2012.6403365.

Lewis, Dyani. "Rare Warming over Antarctica Reveals Power of Stratospheric Models". In: *Nature* 574.7777 (Oct. 2019), pp. 160–161. ISSN: 0028-0836, 1476-4687. DOI: 10.1038/d41586-019-02985-8.

Lindzen, Richard S. "Tides and Gravity Waves in the Upper Atmosphere". In: *Mesospheric Models and Related Experiments*. Ed. by G. Fiocco. Vol. 25. Dordrecht: Springer Netherlands, 1971, pp. 122–130. ISBN: 978-94-010-3116-5 978-94-010-3114-1. DOI: 10.1007/978-94-010-3114-1_8.

Lindzen, Richard S. and Sydney Chapman. "Atmospheric Tides". In: *Space Science Reviews* 10.1 (Oct. 1969), pp. 3–188. ISSN: 1572-9672. DOI: 10.1007/BF00171584.

Lobsiger, E. "Ground-Based Microwave Radiometry to Determine Stratospheric and Mesospheric Ozone Profiles". In: *Journal of Atmospheric and Terrestrial Physics* 49.5 (May 1, 1987), pp. 493–501. ISSN: 0021-9169. DOI: 10.1016/0021-9169(87)90043-2.

Manzini, E. et al. "Northern Winter Climate Change: Assessment of Uncertainty in CMIP5 Projections Related to Stratosphere-Troposphere Coupling: STRATOSPHERE-TROPOSPHERE CLIMATE CHANGE". In: *Journal of Geophysical Research: Atmospheres* 119.13 (July 16, 2014), pp. 7979–7998. ISSN: 2169897X. DOI: 10.1002/2013JD021403.

Matsuno, Taroh. "A Dynamical Model of the Stratospheric Sudden Warming". In: 28.8 (1971), pp. 1479–1494.

Matthias, Vivien and Manfred Ern. "On the Origin of the Mesospheric Quasi-Stationary Planetary Waves in the Unusual Arctic Winter 2015/2016". In: *Atmospheric Chemistry and Physics* 18.7 (Apr. 9, 2018), pp. 4803–4815. ISSN: 1680-7324. DOI: 10.5194/acp-18-4803-2018.

McIntyre, M. E. and T. N. Palmer. "Breaking Planetary Waves in the Stratosphere". In: *Nature* 305.5935 (Oct. 1983), pp. 593–600. ISSN: 0028-0836, 1476-4687. DOI: 10.1038/305593a0.

Müllemann, Arno and Franz-Josef Lübken. “Horizontal Winds in the Mesosphere at High Latitudes”. In: *Advances in Space Research* 35.11 (Jan. 2005), pp. 1890–1894. ISSN: 02731177. DOI: 10.1016/j.asr.2004.11.014.

Nedoluha, Gerald E. et al. “Ground-Based Measurements of Water Vapor in the Middle Atmosphere”. In: *Journal of Geophysical Research: Atmospheres* 100.D2 (1995). _eprint: https://agupubs.onlinelibrary.wiley.com/doi/pdf/10.1029/94JD02952, pp. 2927–2939. ISSN: 2156-2202. DOI: 10.1029/94JD02952.

Newman, P. A. et al. “The Anomalous Change in the QBO in 2015-2016: The Anomalous Change in the 2015-2016 QBO”. In: *Geophysical Research Letters* 43.16 (Aug. 28, 2016), pp. 8791–8797. ISSN: 00948276. DOI: 10.1002/2016GL070373.

Orr, Andrew et al. “Improved Middle Atmosphere Climate and Forecasts in the ECMWF Model through a Nonorographic Gravity Wave Drag Parameterization”. In: *Journal of Climate* 23.22 (Nov. 2010), pp. 5905–5926. ISSN: 0894-8755, 1520-0442. DOI: 10.1175/2010JCLI3490.1.

Palo, S. E. et al. “An Eastward Propagating Two-Day Wave: Evidence for Nonlinear Planetary Wave and Tidal Coupling in the Mesosphere and Lower Thermosphere”. In: *Geophysical Research Letters* 34.7 (Apr. 10, 2007), p. L07807. ISSN: 0094-8276. DOI: 10.1029/2006GL027728.

Pichon, A. Le et al. “Comparison of Co-Located Independent Ground-Based Middle Atmospheric Wind and Temperature Measurements with Numerical Weather Prediction Models”. In: *Journal of Geophysical Research: Atmospheres* 120.16 (2015). _eprint: https://agupubs.onlinelibrary.wiley.com/doi/pdf/10.1002/2015JD023273, pp. 8318–8331. ISSN: 2169-8996. DOI: 10.1002/2015JD023273.

Plumb, R. Alan. “Stratospheric Transport”. In: *Journal of the Meteorological Society of Japan. Ser. II* 80 (4B 2002), pp. 793–809. ISSN: 0026-1165, 2186-9057. DOI: 10.2151/jmsj.80.793.

Reitebuch, Oliver. “The Spaceborne Wind Lidar Mission ADM-Aeolus”. In: *Atmospheric Physics: Background – Methods – Trends*. Ed. by Ulrich Schumann. Research Topics in Aerospace. Berlin, Heidelberg: Springer, 2012, pp. 815–827. ISBN: 978-3-642-30183-4. DOI: 10.1007/978-3-642-30183-4_49.

Rodgers, Clive D. *Inverse Methods for Atmospheric Sounding - Theory and Practice*. Vol. 2. January. 2000. 256 pp. ISBN: 978-981-281-371-8. DOI: 10.1142/9789812813718.

Rogers, Alan E.E. et al. “Seasonal and Local Solar Time Variation of the Meridional Wind at 95km from Observations of the 11.072-GHz Ozone Line and the 557.7-Nm Oxygen Line”. In: *Journal of Atmospheric and Oceanic Technology* 33.7 (2016), pp. 1355–1361. ISSN: 15200426. DOI: 10.1175/JTECH-D-15-0247.1.

Rüfenacht, R. et al. “Intercomparison of Middle-Atmospheric Wind in Observations and Models”. In: *Atmospheric Measurement Techniques* 11.4 (2018), pp. 1971–1987. DOI: 10.5194/amt-11-1971-2018.

Rüfenacht, Rolf. “Ground-Based Doppler Microwave Radiometry for Middle-Atmospheric Wind Profiles”. Bern, Switzerland: Philosophisch-Naturwissenschaftliche Fakultät, Universität Bern, July 2015.

Rüfenacht, Rolf, Klemens Hocke, and Niklaus Kämpfer. “First Continuous Ground-Based Observations of Long Period Oscillations in the Vertically Resolved Wind Field of the Stratosphere and Mesosphere”. In: *Atmospheric Chemistry and Physics* 16.8 (Apr. 2016), pp. 4915–4925. ISSN: 1680-7324. DOI: 10.5194/acp-16-4915-2016.

Rüfenacht, Rolf, N. Kämpfer, and A. Murk. “First Middle-Atmospheric Zonal Wind Profile Measurements with a New Ground-Based Microwave Doppler-Spectro-Radiometer”. In:

Atmospheric Measurement Techniques 5 (2012), pp. 2647–2659. ISSN: 18671381. DOI: 10.5194/amt-5-2647-2012.

Rüfenacht, Rolf et al. "Middle-Atmospheric Zonal and Meridional Wind Profiles from Polar, Tropical and Midlatitudes with the Ground-Based Microwave Doppler Wind Radiometer WIRA". In: *Atmospheric Measurement Techniques* 7.2012 (2014), pp. 4491–4505. ISSN: 1867-8548. DOI: 10.5194/amt-7-4491-2014.

Schranz, Franziska et al. "Investigation of Arctic Middle-Atmospheric Dynamics Using 3 Years of H2O and O3 Measurements from Microwave Radiometers at Ny-Ålesund". In: *Atmospheric Chemistry and Physics* 19.15 (Aug. 8, 2019), pp. 9927–9947. ISSN: 1680-7324. DOI: 10.5194/acp-19-9927-2019.

Schranz, Franziska et al. *Small-Scale Variability of Stratospheric Ozone during the SSW 2018/2019 Observed at Ny-ÅLesund, Svalbard.* preprint. Gases/Remote Sensing/Stratosphere/Physics (physical properties and processes), Dec. 11, 2019. DOI: 10.5194/acp-2019-1093.

– "Small-Scale Variability of Stratospheric Ozone during the SSW 2018/2019 Observed at Ny-Ålesund, Svalbard". In: (Dec. 11, 2019). DOI: 10.5194/acp-2019-1093.

Shah, Kathryn Pierce, Duane O. Muhleman, and Glenn L. Berge. "Measurement of Winds in Venus' Upper Mesosphere Based on Doppler Shifts of the 2.6-Mm 12CO Line". In: *Icarus* 93.1 (Sept. 1, 1991), pp. 96–121. ISSN: 0019-1035. DOI: 10.1016/0019-1035(91)90167-R.

Shaw, Tiffany A. and Theodore G. Shepherd. "Raising the Roof". In: *Nature Geoscience* 1.1 (Jan. 2008), pp. 12–13. ISSN: 1752-0894, 1752-0908. DOI: 10.1038/ngeo.2007.53.

Shepherd, Theodore G. "The Middle Atmosphere". In: *Journal of Atmospheric and Solar-Terrestrial Physics* 62.17-18 (Nov. 2000), pp. 1587–1601. ISSN: 13646826. DOI: 10.1016/S1364-6826(00)00114-0.

Sigmond, M. et al. "Enhanced Seasonal Forecast Skill Following Stratospheric Sudden Warmings". In: *Nature Geoscience* 6.2 (Feb. 2013), pp. 98–102. ISSN: 1752-0894, 1752-0908. DOI: 10.1038/ngeo1698.

Souprayen, Claude et al. "Rayleigh–Mie Doppler Wind Lidar for Atmospheric Measurements. I. Instrumental Setup, Validation, and First Climatological Results". In: *Appl. Opt.* 38.12 (Apr. 1999), pp. 2410–2421. DOI: 10.1364/AO.38.002410.

Stober, G. et al. "Exceptionally Strong Summer-like Zonal Wind Reversal in the Upper Mesosphere during Winter 2015/16". In: *Annales Geophysicae* 35.3 (2017), pp. 711–720. DOI: 10.5194/angeo-35-711-2017.

Stober, G. et al. "Meteor Radar Temperatures over Collm (51.3°N, 13°E)". In: *Advances in Space Research* 42.7 (2008), pp. 1253–1258. ISSN: 0273-1177. DOI: 10.1016/j.asr.2007.10.018.

Stober, Gunter et al. "Retrieving Horizontally Resolved Wind Fields Using Multi-Static Meteor Radar Observations". In: *Atmospheric Measurement Techniques* 11.8 (Aug. 27, 2018), pp. 4891–4907. ISSN: 1867-8548. DOI: 10.5194/amt-11-4891-2018.

Strelnikov, Boris et al. "Spatial and Temporal Variability in MLT Turbulence Inferred from in Situ and Ground-Based Observations during the WADIS-1 Sounding Rocket Campaign". In: *Annales Geophysicae* 35.3 (Apr. 10, 2017), pp. 547–565. ISSN: 1432-0576. DOI: 10.5194/angeo-35-547-2017.

Suess, Martin. "Frequency Calibration of the SWI Instrument On-Board of JUICE Using SpaceWire Time-Codes". In: *2014 International SpaceWire Conference (SpaceWire).* 2014 International SpaceWire Conference (SpaceWire). Sept. 2014, pp. 1–4. DOI: 10.1109/SpaceWire.2014.6936231.

Varotsos, Costas. “The Southern Hemisphere Ozone Hole Split in 2002”. In: *Environmental Science and Pollution Research* 9.6 (Nov. 2002), pp. 375–376. ISSN: 0944-1344, 1614-7499. DOI: 10.1007/BF02987584.

Volland, Hans. *Atmospheric Tidal and Planetary Waves*. Springer Science & Business Media, Dec. 6, 2012. 358 pp. ISBN: 978-94-009-2861-9. Google Books: jDXwCAAAQBAJ.

Wilhelm, S., G. Stober, and P. Brown. “Climatologies and Long-Term Changes of Mesospheric Wind and Wave Measurements Based on Radar Observations at High and Mid-Latitudes”. In: *Annales Geophysicae Discussions* 2019 (2019), pp. 1–37. DOI: 10.5194/angeo-2019-51.

Wu, Dong L. et al. “Mesospheric Doppler Wind Measurements from Aura Microwave Limb Sounder (MLS)”. In: *Advances in Space Research* 42.7 (2008), pp. 1246–1252. ISSN: 02731177. DOI: 10.1016/j.asr.2007.06.014.

Yan, Zhaoai et al. “Development of a Mobile Doppler Lidar System for Wind and Temperature Measurements at 30–70km”. In: *Journal of Quantitative Spectroscopy and Radiative Transfer* 188 (Supplement C 2017), pp. 52–59. ISSN: 0022-4073. DOI: https://doi.org/10.1016/j.jqsrt.2016.04.024.

List of publications

Publications

Jonas Hagen, Andres Luder, Axel Murk, and Niklaus Kämpfer. "Frequency-Agile FFT Spectrometer for Microwave Remote Sensing Applications". In: *Atmosphere* 11.5 (May 11, 2020), p. 490. ISSN: 2073-4433. DOI: 10.3390/atmos11050490

Jonas Hagen, Klemens Hocke, Gunter Stober, Simon Pfreundschuh, Axel Murk, and Niklaus Kämpfer. "First Measurements of Tides in the Stratosphere and Lower Mesosphere by Ground-Based Doppler Microwave Wind Radiometry". In: *Atmospheric Chemistry and Physics* 20.4 (Feb. 28, 2020), pp. 2367–2386. ISSN: 1680-7324. DOI: 10.5194/acp-20-2367-2020

Franziska Schranz, Jonas Hagen, Gunter Stober, Klemens Hocke, Axel Murk, and Niklaus Kämpfer. "Small-Scale Variability of Stratospheric Ozone during the SSW 2018/2019 Observed at Ny-Ålesund, Svalbard". In: (Dec. 11, 2019). DOI: 10.5194/acp-2019-1093

Elisabeth Blanc, Katy Pol, Alexis Le Pichon, Alain Hauchecorne, Philippe Keckhut, Gerd Baumgarten, Jens Hildebrand, Josef Höffner, Gunter Stober, Robert Hibbins, Patrick Espy, Markus Rapp, Bernd Kaifler, Lars Ceranna, Patrick Hupe, Jonas Hagen, Rolf Rüfenacht, Niklaus Kämpfer, and Pieter Smets. "Middle Atmosphere Variability and Model Uncertainties as Investigated in the Framework of the ARISE Project". In: *Infrasound Monitoring for Atmospheric Studies*. Ed. by Alexis Le Pichon, Elisabeth Blanc, and Alain Hauchecorne. Cham: Springer International Publishing, 2019, pp. 845–887. ISBN: 978-3-319-75138-2 978-3-319-75140-5. DOI: 10.1007/978-3-319-75140-5_28

Klemens Hocke, Leonie Bernet, Jonas Hagen, Axel Murk, Matthias Renker, and Christian Mätzler. "Diurnal Cycle of Short-Term Fluctuations of Integrated Water Vapour above Switzerland". In: *Atmospheric Chemistry and Physics* 19.19 (Sept. 30, 2019), pp. 12083–12090. ISSN: 1680-7324. DOI: 10.5194/acp-19-12083-2019

Jonas Hagen, Axel Murk, Rolf Rüfenacht, Sergey Khaykin, Alain Hauchecorne, and Niklaus Kämpfer. "WIRA-C: A Compact 142-GHz-Radiometer for Continuous Middle-Atmospheric Wind Measurements". In: *Atmospheric Measurement Techniques* 11.9 (Sept. 4, 2018), pp. 5007–5024. ISSN: 1867-8548. DOI: 10.5194/amt-11-5007-2018

Klemens Hocke, Martin Lainer, Lorena Moreira, Jonas Hagen, Susana Fernandez Vidal, and Franziska Schranz. "Atmospheric Inertia-Gravity Waves Retrieved from Level-2 Data of the Satellite Microwave Limb Sounder Aura/MLS". in: *Annales Geophysicae* 34.9 (Sept. 19, 2016), pp. 781–788. ISSN: 1432-0576. DOI: 10.5194/angeo-34-781-2016

Selected Talks

Jonas Hagen, Franziska Schranz, Klemens Hocke, and Niklaus Kämpfer: "Stratospheric and mesospheric diurnal wind cycle from microwave Doppler wind measurements", EGU 2019, Vienna, Austria, 10 April 2018, EGU2019-17242

Jonas Hagen, Rolf Rüfenacht, Niklaus Kämpfer, Sergey Khaykin, Alain Hauchecorne, and Gerd Baumgarten: "Results from stratospheric and mesospheric wind measurement campaigns from tropical, polar and mid-latitudes by microwave radiometry", EGU 2018, Vienna, Austria, 13 April 2018, EGU2018-4930

Jonas Hagen, Niklaus Kämpfer, Sergey Khaykin, and Alain Hauchecorne: "Stratospheric and mesospheric wind measurements from the new WIRA-C wind radiometer and comparison to the Doppler lidar on La Réunion island", EGU 2017, Vienna, Austria, 25 April 2017, EGU2017-3612.

Jonas Hagen, Axel Murk, Niklaus Kämpfer: "A compact 142-GHz-radiometer for continuous middle-atmospheric wind measurements", Microrad, Espoo, Finnland, 13 April 2016

Online

The list of publications is available online:

https://orcid.org/0000-0002-3484-4266

Acknowledgements

I am thankful for the collaboration with and help from all the technical staff, namely Andres Luder, Nik Jaussi, Daniel Weber, Adrian Jenk and Beat Hiltbrunner. I really enjoyed working with you and am grateful for all the technical knowledge I could gain from you throughout my years at the IAP.

I appreciate the help and support of our office team members Beatrice Thut, Simone Corry, Yvette Eggenschwiler and Franziska Stämpfli. Your help in organizing the transport of the scientific instruments and all the other countless efforts are indispensable.

All the other PhD students and postdocs deserve my appreciation for their contributions, either scientific, technical or mentally, especially Franziska Schanz, Leonie Bernet, Karl Jacob, Martin Lainer, Ansgar Schanz, Eric Sauvageat and of course all the others.

The help and support of Rolf Rüfenacht, Susana Fernandez-Vidal and Francisco Navas-Guzmán is especially appreciated.

Manes Hornung deserves special thanks for all the conversations we had together. His powers of comprehension and his empathy helped me in many ways.

I thank Niklaus Kämpfer for his guidance and supervision during my masters and PhD studies and for acquiring the funding required for these projects. Especially I am thankful for his continued support after his retirement.

I thank Axel Murk for his constant support and his profound expertise in all technical subjects. Further, I am thankful to Axel for his effort in taking the group lead after Nik's retirement.

I am thankful to Klemens Hocke for his invaluable help and for always having time to discuss results.

The enthusiasm of Gunter Stober made a huge difference in the process of writing the tides paper. I appreciate his help and contributions since he joined our group, not only to this thesis but to the MW group in general.

The help of all the ARTS community was invaluable. Especially I tank Simon Pfreundschuh, Ole Martin Christensen and Patrick Eriksson for their support and the organisation of the ARTS Community Workshop 2017.

The open-source community around python, xarray, numpy, matplotlib (and countless others) is greatly appreciated.

Erklärung

gemäss Art. 18 PromR Phil.-nat. 2019

Name/Vorname:	Jonas Hagen
Matrikelnummer:	10-113-843
Studiengang:	Physik Bachelor ☐ Master ☐ Dissertation ☒
Titel der Arbeit:	Observations of middle-atmospheric wind by ground-based microwave Doppler wind radiometry
Leiter der Arbeit:	Prof. Dr. Niklaus Kämpfer

Ich erkläre hiermit, dass ich diese Arbeit selbständig verfasst und keine anderen als die angegebenen Quellen benutzt habe. Alle Stellen, die wörtlich oder sinngemäss aus Quellen entnommen wurden, habe ich als solche gekennzeichnet. Mir ist bekannt, dass andernfalls der Senat gemäss Artikel 36 Absatz 1 Buchstabe r des Gesetzes über die Universität vom 5. September 1996 und Artikel 69 des Universitätsstatuts vom 7. Juni 2011 zum Entzug des Doktortitels berechtigt ist. Für die Zwecke der Begutachtung und der Überprüfung der Einhaltung der Selbständigkeitserklärung bzw. der Reglemente betreffend Plagiate erteile ich der Universität Bern das Recht, die dazu erforderlichen Personendaten zu bearbeiten und Nutzungshandlungen vorzunehmen, insbesondere die Doktorarbeit zu vervielfältigen und dauerhaft in einer Datenbank zu speichern sowie diese zur Überprüfung von Arbeiten Dritter zu verwenden oder hierzu zur Verfügung zu stellen.

Bern, den 29. Mai 2020

Jonas Hagen

Curriculum vitae

Jonas Hagen

Date of birth:	15. November 1990
Place of origin:	Hüttwilen TG
Email:	jonas.hagen@iap.unibe.ch

Education

since Nov. 2015	PhD thesis on *Middle-atmospheric wind measurements by the ground-based passive radiometer WIRA-C* Supervised by Prof. Dr. Niklaus Kämpfer Institute of Applied Physics, University of Bern, Switzerland
2014 - 2015	Master of science in Applied Physics University of Bern, Switzerland Thesis on the *Design and characterisation of a compact 142-GHz-radiometer for middle-atmospheric wind measurements*, supervised by Prof. Dr. Niklaus Kämpfer
2010 - 2014	Bachelor of science in Physics with Minor Mathematics University of Bern, Switzerland Thesis on the *Evaluation of digital micro-mirrors as fluidics-system*, supervised by Prof. Dr. Jaro Rička

Work experience

2014 - 2020	IT Systems Administrator Institute of Applied Physics, University of Bern, Switzerland
2010 - 2014	Software Developer Xovis AG, Zollikofen, Switzerland
Feb. - Jun. 2014	Civil Service at METAS Federal Institute of Metrology, Wabern, Switzerland

Errata

- p. 9: "[...] which built upon the grounds of the **first** ARISE project."
- p. 15: "[...] with a maximum in volume mixing **ratio** between 20 and 60 km."
- p. 17, Fig. 2.4: "Overview of the mechanics in **WIRA-C**."
- p. 22: "[...] the improvement **from** v1 to v2 is [...]"
- p. 31: "For example, one can see the atmospheric wind reversal around equinox in March 2017 from the westwards regime changing to the eastwards regime and back (November **2017**)."
- p. 31, Tab. 4.1: "Period: 2016-08-28 to 2018-**01**-27"
- p. 39 "Figure 4.11 and figure **4.12** show the whole WIRA-C time series measured at ALOMAR [...]"
- p. 111: Correct citation: Franziska Schranz, Jonas Hagen, Gunter Stober, Klemens Hocke, Axel Murk, and Niklaus Kämpfer. "Small-Scale Variability of Stratospheric Ozone during the SSW 2018/2019 Observed at Ny-Ålesund, Svalbard". In: *Atmospheric Chemistry and Physics Discussion* (Dec. 11, 2019). DOI: 10.5194/acp-2019-1093
- Along and instead of (Baumgarten and Stober, 2019), the work from Baumgarten et al., 2018 should have been cited: Kathrin Baumgarten, Michael Gerding, Gerd Baumgarten, and Franz-Josef Lübken. "Temporal Variability of Tidal and Gravity Waves during a Record Long 10-Day Continuous Lidar Sounding". In: *Atmospheric Chemistry and Physics* 18.1 (Jan. 12, 2018), pp. 371–384. ISSN: 1680-7324. DOI: 10.5194/acp-18-371-2018.

Bern, June 15. 2020
Jonas Hagen